NOVEL MULTIMODAL SENSING SYSTEMS FOR WEARABLE KNEE HEALTH ASSESSMENT

A Dissertation
Presented to
The Academic Faculty

By

Caitlin N. Teague

In Partial Fulfillment
of the Requirements for the Degree
Doctor of Philosophy in the
School of Electrical and Computer Engineering

Georgia Institute of Technology

May 2020

NOVEL MULTIMODAL SENSING SYSTEMS FOR WEARABLE KNEE HEALTH ASSESSMENT

Approved by:

Dr. Omer T. Inan, Advisor
School of Electrical and Computer Engineering
Georgia Institute of Technology

Dr. Hua Wang
School of Electrical and Computer Engineering
Georgia Institute of Technology

Dr. Mozziyar Etemadi
Feinberg School of Medicine
Northwestern University

Dr. Muhannad S. Bakir
School of Electrical and Computer Engineering
Georgia Institute of Technology

Dr. Mindy L. Millard-Stafford
School of Biological Sciences
Georgia Institute of Technology

Date Approved: March 13, 2020

To my family, with love.

ACKNOWLEDGEMENTS

In pursuit of my Ph.D., so many have provided positive influences on my life in either a professional or personal capacity, and I would like to express my thanks to some of them in this section.

It would be remiss of me to start my many thanks with anyone but my advisor and mentor, Dr. Omer T. Inan. From our first meeting in a coffee shop, as would be the site for many of our conversations over the years, he has sparked an enthusiasm for research in me. I met with him that spring day about to graduate with my Bachelor's degree unclear of what path to pursue but convinced I did not want to leave school to do "boring" and unfulfilling work. That meeting changed my life, as he introduced me to a field that is exciting, interesting, and one that I am passionate about. Over the course of the next six years, Dr. Inan (or Omer) has provided constant encouragement, motivation, and technical guidance—always done with great humor and kindness. He has built and fostered an incredible lab environment, and I feel fortunate to have been a part of it, working for (or "with" as Dr. Inan will insist) him. I look forward to future coffee shop talks with him.

I would also like to thank Dr. Muhannad S. Bakir, Dr. Hua Wang, Dr. Mindy L. Millard-Stafford, and Dr. Mozziyar Etemadi for taking the time to serve as members of my dissertation committee and for providing insightful comments to improve my work and the content of this dissertation.

I am extremely fortunate to have worked alongside intelligent, hard-working, and kind lab members: Sinan Hersek, Hakan Töreyin, Oludotun Ode, Andrew Carek, Nicholas Bolus, Brandi Nevius, Jordan Conant, Hyeon Ki Jeong, Samer Mabrouk, Venu Ganti, and the *many* others not explicitly listed here but their influence very much felt. First, I would like to thank Sinan Hersek with whom I worked closely during the initial phases of the joint sounds work. His relentless work ethic, sharp technical skills for both hardware and software, and friendly, positive attitude were invaluable. I am glad to have worked with

him at the start of my research career and to have had him by my side, especially during long data collection or troubleshooting sessions. I thank Hakan Töreyin whose seniority helped guide me as a young researcher. I would like to thank Jordan Conant and Brandi Nevius for spearheading mechanical designs for the many knee brace prototypes. A special thanks to Brandi for her work on developing an *actually deployable* brace device, which was done with unmatched organization and attention to detail for system design. She also provided a much-needed (female) friendship at times. I am also thankful to Dotun Ode for his help with theoretical and computer science topics. Beyond this, sharing of a laugh and a sleeve of Oreos with a friend was always welcomed. He deserves all the rewards heaven will grant him. I extend special thanks to Nick Bolus, my friend, my desk partner, and my cheerleader for when I look particularly exasperated. His knowledge of mechanical systems and biomechanical fundamentals were particularly useful, and his availability to always read a *rough* draft was also much appreciated. His navigation of the English (and Latin) language has "embiggened" my own scientific vernacular. In Bill Belichick and Nick Saban we trust. Lastly, I would like to thank Andrew Carek. Though we never actually worked together on the same project, the time we worked together in lab, on class projects, and at various internships would suggest otherwise. He was always willing to help debug difficult problems, lend an extra—and more skilled—set of hands, and tackle anything else research would throw at us. I appreciated the freedom to talk freely about ideas without fear or intimidation that my ideas would be considered "silly" or "dumb" even when some admittedly were ("Cafecito"). I am happy to call him a friend.

I would like to thank the members of the Etemadi Research Group of Northwestern University. Firstly, to Dr. Etemadi for providing me the invaluable opportunity to intern for a summer in the clinical environment. I extend thanks to J. Alex Heller for his exhaustive knowledge of embedded systems. I greatly appreciated our walks to Starbucks to clear my head and our many texts and phone calls to debug problems. I thank Flori Garcia-Vicente for ensuring my summer was productive.

I thank my friends and "family-to-me", especially Ashley Lemire, Matthew Rudinsky, and Barbara Lemire. I am blessed to have such good lifelong friends and look forward to another 20 years of friendship. I thank my soon-to-be (officially) family, the Wittbrodts, who have welcomed me with open arms and love me as one of their own.

Next, I wholeheartedly thank my family. I will start the long list of family with my parents, Karen and Michael Teague, whom I am blessed to call mom and dad. They have provided unwavering love and support, and throughout life, they helped me chase after—or provided the gentle nudge when needed to go after—every opportunity I desired. I thank them for always answering my phone calls (the less-happy ones to mom and more-happy ones to dad) and for understanding when I do not immediately text back at times. I thank them for filling a home with so much love and laughter—and so many siblings. I extend thanks to my siblings, Ryan (and sister-in-law Katie), Daniel, Andrew, and Nicole (and Maddie). I feel I can do anything with them by my side, and as a group, we are unstoppable. I feel such pride to be an older sister to such amazing individuals. They have been amazingly supportive and protective. I thank my grandparents, Jeannine and Leo Teague and Elaine and Roland Rondeau, for the love only grandparents can give. Memere and Papa, thank you for the many wake-up calls following late nights in the lab, the much-needed mental breaks in Florida, and endless encouragement. To the rest of my family, though you are not mentioned by name here, your love and support is felt and deeply appreciated.

Finally, I thank my fiancé, Matthew Wittbrodt, for his continued love and support. Beyond all the other wonderful experiences the Ph.D. has afforded me, it provided me the happy fortune of meeting Matt. Over the years, he has read countless drafts, listened to numerous practice talks, and brewed endless cups of tea. He is always willing to help me with a problem, namely statistics, and when it was outside his immediate brilliance, he always lent an empathetic ear. Our runs, soccer games, and walks around Atlanta are treasured. He brings such joy and overwhelming happiness to my life. I could not wish for a better life partner, and I am so excited for our next phase in life.

TABLE OF CONTENTS

LIST OF TABLES

LIST OF FIGURES

LIST OF SYMBOLS AND ABBREVIATIONS

AC	Alternating Current
ACC	Accelerometer
ACL	Anterior Cruciate Ligament
ADC	Analog-to-digital Converter
AFE	Analog Front-end
AHRPO	Army Human Research Protection Office
AIC	Akaike Information Criterion
BPF	Band-pass Filter
DAQ	Data Acquisition Unit
DC	Direct Current
DVJ	Drop Vertical Jump
EBI	Electrical Bioimpedance
EBI-Switch	Electrical Bioimpedance Switch
f_c	Cut-off Frequency
GCF	Graph Community Factor
GYR	Gyroscope
HRPO	Human Research Protection Office
IA	Instrumentation Amplifier
I^2C	Inter-integrated Circuit
I^2S	Inter-integrated Circuit Sound
IC	Integrated Circuit
ICC	Intraclass Correlation Coefficient
IMU	Inertial Measurement Unit
IRB	Institutional Review Board
JS-Switch	Joint Sounds Switch

kNN	k-Nearest Neighbor
LED	Light-emitting Diode
MCU	Microcontroller
MEMS	Microelectromechanical Systems
mHealth	Mobile Health
Mic	Microphone
microSD Card	Miniaturized Secure Digital Card
Op-Amp	Operational Amplifier
PCB	Printed Circuit Board
PDF	Probability Distribution Function
PLA	Polylactic Acid
RAM	Random-access Memory
RMS	Root Mean Square
ROM	Range-of-motion
SNIR	Signal-to-noise-and-interference Ratio
SNR	Signal-to-noise Ration
SPI	Serial Peripheral Interface
STFT	Short-time Fourier Transform
TDM	Time Division Multiplexing
USB	Universal Serial Bus
WUS	Wake-up System
μC	Microcontroller

SUMMARY

Wearable technologies for healthcare represent a popular research area, as they can provide quantitative metrics during rehabilitation, enable long-term, at-home monitoring of chronic conditions, and facilitate preventative—versus reactive—medical interventions. Moreover, their low cost makes them accessible to broad subject populations and enables more frequent measures of biomarkers. Such technologies are particularly useful for areas of medicine where the diagnostic or evaluation tools are expensive, not readily available, or time consuming. Orthopedics, in particular joint health assessment, is an area where wearable devices may provide clinicians and patients with more readily available quantitative data. The objective of this research is to investigate wearable, multimodal sensing technologies to facilitate joint health and rehabilitation monitoring, ultimately providing a "joint health score" based on evaluation of joint acoustics, electrical bioimpedance, inertial measures, and temperature data. This joint health score may be employed in various applications—including during rehabilitation after an acute injury and management of joint diseases, such as arthritis—providing an actionable metric for physicians based on the underlying physiological changes of the joint itself. This work specifically investigates the hardware for such a system. First, we examined microphones suited for wearable applications (e.g., miniature, inexpensive) that still provide robust measurements in terms of signal quality and consistency for repeated measurements. Second, we implemented a microcontroller-based system to sample high-throughput audio data as well as lower-rate electrical bioimpedance, inertial, and temperature data, which was incorporated into a fully untethered "brace." Importantly, this work provides the fundamental hardware system for wearable knee joint health assessment.

CHAPTER 1
INTRODUCTION

1.1 Motivation

The knee is one of the most complex joints in the body [1] and is thereby subject to extreme stress due to the multidirectional forces exerted on the joint during motion [1, 2]; additionally, its intricate structural arrangement, reliance on soft tissue networks for structural stability, and large loading requirements leave the joint particularly susceptible to injury [3–5]. As a result, the knee represents not only one of the most frequently injured body parts but also accounts for many severe injuries in terms of time of restricted and / or total loss of participation among athletes [6–8], military personnel [9], and other populations engaged in high performance activities [10]. Moreover, knee injuries are not exclusive to active populations; sedentary populations may be at higher risk for such injuries due to poor cardiovascular health, atrophied surrounding muscles which fail to properly stabilize the joint, and lack of training and warm-up [2, 10]. This frequency across populations combined with the extensive treatment requirements—often entailing surgery and / or substantial rehabilitation [3]—result in approximately 10.4 million patient visits annually in the United States [11]. Beyond injuries, joint diseases, such as arthritis, are prevalent among Americans with nearly 25% of the population diagnosed with some form of the disease [12]. To this extent, injuries and degenerative diseases are considerable in their effect on not only the health care system but also on patients' daily lives given the knee's significance in performing ambulatory motions and other everyday activities [4].

To alleviate such strains on the health care system and facilitate monitoring of patients during daily activities, researchers have explored the use of wearable devices to unobtrusively acquire health information [13]. With regard to musculoskeletal and biomechanical-

related disorders and injuries, these systems may provide a new way to collect objective and quantitative data. For example, Rampp *et al.* assessed gait impairment parameters in elderly populations using data from inertial sensors worn on shoes, thus providing a successful wearable alternative to clinic-based diagnostics (e.g., specialist observation, camera-based laboratories, sensor-embedded walkways, etc.) [14]. Atallah *et al.* also investigated gait, leveraging changes in gait patterns in post-operative, knee-replacement patients to evaluate recovery progress by utilizing an ear-worn sensor [15]. Toffola *et al.* developed a wearable sleeve to record robust knee joint kinematics and subject compliance during long-term, at-home activities and therapies [16].

Similar approaches may be employed for knee injuries and diseases, and accordingly, we propose a wearable system for knee joint health monitoring, leveraging multiple sensing modalities: joint acoustics, electrical bioimpedance, inertial measures, and temperature data. Ultimately, we envision data from these sensors would be acquired and input to feature extraction and machine learning algorithms, outputting a "joint health score" and providing quantifiable data that physicians and patients can act upon.

1.2 Major Contributions of this Work

While knee acoustic emissions have been previously used for evaluation of joint health [17], to the best of our knowledge, no work has focused on translating these sensing techniques to a wearable (untethered) device. This thesis presents methods for facilitating *feasible* in-clinic or at-home measurements for joint health assessment with a focus on capturing joint sounds. As such, the major contributions of this work include:

1. Demonstrated, for the first time, that miniature microphones and accelerometers amenable to wearable implementations can accurately capture joint sound measurements from the knee.

2. Quantified the robustness and repeatability of knee sound measurement methods in

student-athletes rehabilitating acute knee injuries as well as healthy controls.

3. Designed, implemented, and validated low power, high fidelity wearable electronics to record multiple modalities of joint health data including sounds, electrical bioimpedance spectroscopy, kinematics, and skin temperature.

1.3 Thesis Organization

The rest of this thesis is organized as follows: Chapter 2 provides a summary of the sensing modalities proposed for joint health assessment as well as the motivation for employing multiple sensing methods for knee health assessment. Chapter 3 investigates microphones for sensing knee joint sounds for wearable applications, while Chapter 4 presents a wearable "brace" for acquiring joint sounds, electrical bioimpedance, inertial measures, and temperature data. Lastly, Chapter 5 provides final conclusions and proposed directions for future work. Synopses of Chapters 3 and 4 are provided in the immediate sections (Sections 1.3.1 and 1.3.2).

1.3.1 Chapter 3 Summary

Chapter 3 examines contact-based and airborne measurement of knee joint acoustic emissions. We used three types of microphones—electret, MEMS, and piezoelectric film microphones—to obtain joint sounds in healthy collegiate athletes during unloaded flexion / extension, and we evaluated the microphones' capabilities of acquiring robust measurements by examining two main parameters: (1) signal quality and (2) within-day consistency of measurements. First, we determined that air microphones acquire higher quality signals than contact microphones for wearable measurements (SNIR of 11.7 dB and 12.4 dB for electret and MEMS respectively vs. 8.4 dB for piezoelectric). Furthermore, we found that air microphones measured similar acoustic signatures on the skin and 5 cm off the skin ($\sim$4.5$\times$ smaller amplitude). Second, we determined that the main acoustic event during repetitive motions occurs at consistent joint angles using intraclass correlation

coefficients (ICC(1, 1) = 0.94 and ICC(1, k) = 0.99). Additionally, we found that this angular location was similar between right and left legs ($p > 0.05$) although some individuals exhibited asymmetry between legs. We conclude that piezoelectric microphones currently are not recommended for joint sound acquisition, as the interface noise must be reduced by packaging techniques for practical implementation within a device. Importantly, we show that airborne signals can be measured consistently and that healthy left and right knees often produce a similar pattern in acoustic emissions.

These initial findings were part of a larger study constructed to examine how joint health biomarkers, namely knee acoustics and electrical bioimpedance data, changed following rehabilitation following an acute injury. For comparison and data processing algorithms, data from healthy subjects (i.e., subjects with no recent knee injury, < 2 years) as well as those with knee injuries (collected pre- and post-rehabilitation) were collected. Results from the overall study are presented.

We briefly examined different characteristics of joint sounds for the healthy subject population. First, we examined the location of clicks for extension and flexion phases of exercises, finding that clicks are more likely to occur towards fully-extended positions during extension and at two peaks approximately at one- or two-thirds maximum angle for flexion. These results generally corresponded with results of a separate cadaver-based study. Further, we evaluated the *b*-value metric, a measure of the distribution of large to small amplitude acoustic signatures, in males and females. Significant differences ($p < 0.0001$) were found between males' (1.44 ± 0.31) and females' (1.14 ± 0.23) dominant legs, while no difference was observed between the non-dominant legs of males and females (male = 1.43 ± 0.25, female = 1.31 ± 0.37, $p = 0.10$). Females also exhibited smaller *b*-values in their dominant leg (by 0.17 ± 0.35, $p = 0.007$), while males did not (-0.014 ± 0.24, $p = 0.75$). A similar analysis was performed for sport-matched subjects, specifically men's and women's basketball players. Comparisons of men's and women's basketball players' dominant (men = 1.34 ± 0.19, women = 1.15 ± 0.24, $p = 0.08$) and non-dominant (men = 1.26

$\pm$ 0.22, women = 1.39 $\pm$ 0.37, p = 0.23) legs were not significant. Women's basketball players did have a significantly lower *b*-value in their dominant leg (by 0.25 $\pm$ 0.40, p = 0.01), but men's were not significantly different (0.07 $\pm$ 0.16, p = 0.50). These findings provide and initial examination of joint acoustics in healthy collegiate athletes.

Importantly, we used joint acoustics to track the improvement in joint health in subjects with a knee injury following months of rehabilitation in a longitudinal study. We employed an unsupervised graph mining algorithm to visualize heterogeneity of the high-dimensional acoustical emission data, and to then derive a quantitative metric capturing this heterogeneity—the graph community factor (GCF). A total of 42 subjects participated in the studies. Measurements were taken once each from 33 healthy subjects with no known previous knee injury, and twice each from 9 subjects with unilateral knee injury: first, within seven days of the injury, and second, 4 – 6 months after surgery when the subjects were determined ready to start functional activities. Acoustical signals were processed to extract time and frequency domain features from multiple time windows of the recordings from both knees, and k-Nearest Neighbor graphs were then constructed based on these features. Results: The GCF calculated from these graphs was found to be 18.5 $\pm$ 3.5 for healthy subjects, 24.8 $\pm$ 4.4 (p = 0.01) for recently injured and 16.5 $\pm$ 4.7 (p = 0.01) at 4 – 6 months recovery from surgery. The objective GCF scores changes were consistent with a medical professional's subjective evaluations and subjective functional scores of knee recovery.

1.3.2 Chapter 4 Summary

Chapter 4 details the design and validation of a wearable, multimodal sensor brace for knee joint health assessment. An embedded-, two-microcontroller-based approach is used to sample high-throughput, multi-microphone joint acoustics (46.785 kHz) as well as lower-rate electrical bioimpedance (EBI) (1/46.17 s), inertial (100 – 250 Hz), and skin temperature (1 Hz) data, and these data are saved onto microSD cards. Additionally, a flexible, 3D-printed brace houses the custom circuit boards and sensors to enable wearable sensing.

The system achieves 9 hours of continuous joint sound recording, while the EBI, inertial, and temperature sensors can sample for 35 hours using 500 mAh batteries. Further, for the entirety of these continuous recordings, there were no dropped samples for any of the sensors. Lastly, proof-of-concept measurements were used to show the system's efficacy for recording joint sounds and swelling data. This is, to the best of our knowledge, the first, completely untethered wearable system for multimodal, knee health monitoring.

Moreover, we describe the design and validation of a real-time, automated wake-up system for triggering measurements of knee health, specifically the sampling of joint sound data and electrical bioimpedance as analogues for structural health and swelling, respectively. The wake-up system utilizes custom switches retrofitted to a commercially-available, hinged knee brace to provide information about angular motion and leg position. A low-power microcontroller is used to run an activity classification algorithm, which searches for instances of flexion / extension and sit-to-stand exercises or the position used for optimal EBI measurements. If these tasks are recognized, signals are sent to a smart brace to initiate specific recordings (i.e., the sampling from only the relevant sensors needed). In addition to characterizing the electronic design, we also report the classification results from four able-bodied subjects participating in randomized activities to determine if the system successfully triggered recordings of joint health.

CHAPTER 2

A MULTIMODAL APPROACH: SENSING MODALITIES

2.1 Sensing Modalities

As part of the multimodal joint health assessment system, four signals are considered: (1) joint acoustical emissions, (2) electrical bioimpedance, (3) inertial measurements, and (4) temperature. These sensing modalities are described in this chapter, and a summary of the sensing types available for each modality is summarized in Table 2.1. Because temperature is primarily used to provide contextual information for the other acquired signals in this work, its stand-alone physiological significance will not be elaborated in detail here.

2.1.1 Acoustical Emissions from the Knee

Acoustics can provide an unobtrusive method—and thus a possible wearable platform—for capturing information regarding *underlying* physical structures and alignments, articulating surfaces, and soft tissue characteristics. Friction between the structures and articulating components of the knee joint gives rise to various kinds of vibrations [19]. These vibrations (i.e., acoustical energy) travel to the skin surface where they encounter a large impedance mismatch between the fluid-filled tissue and air. Because of this, most of the acoustical energy manifests itself as vibrations signals on the skin with the majority of the energy reflected back into the tissue [20]. However, there is a small amount of energy that propagates to the air, resulting in audible joint sounds. While some very early work in this area studied airborne signals using "air" microphones, the majority of research has largely utilized vibration sensors as "contact" microphones (e.g., accelerometers, piezoelectric devices, stethoscopes) to measure joint sound vibrations [17].

Researchers have concentrated on the efficacy of joint acoustic emissions, or vibroartho-

Table 2.1: Joint Health Assessment Sensing Modalities[a]

Modality	Sensor Type	Advantages	Disadvantages
Sounds	Electret Mic	• Low rubbing noise • High signal-to-noise ratio (SNR)	• Price • Background noise • Mounting / positioning
	Microelectro-mechanical System (MEMS) Mic	• Low rubbing noise • Inexpensive • Medium-high SNR	• Frequency response • Background noise • Mounting / positioning
	Contact Mic	• Coupling to body • High SNR • Background rejection	• Rubbing noise • Packaging
Electrical Bio-impedance (EBI)	Gel (Ag/AgCl)	• Coupling to body • Low impedance • Inexpensive	• Discomfort (gel) • Non-reusable
	Dry (e.g., copper)	• Medium-low impedance • Inexpensive	• Discomfort (metal) • Reliability (long-term)
Activity Context	Inertial Measurement Unit (IMU)	• Angle accuracy • Limb position	• Computational complexity • Calibration
	Encoder	• Accuracy • Direct measurement • No calibration	• No position information • Structure required

[a] Reproduced from [18].

graphic signals (VAG), as clinically-relevant biomarkers for joint health, and notably, the majority of the research has worked towards developing diagnostic techniques to differentiate "healthy" vs. "unhealthy" knee joints, primarily as it concerns cartilage-based conditions such as osteoarthritis and chondromalacia. For example, Mollan *et al.* measured acoustic emissions from the knee using a condenser microphone and captured low frequency signals (< 100 Hz) [20] while Shark *et al.* used wide-band piezoelectric sensors to record emissions in the ultrasonic band (> 20 kHz) [20, 21]. They observed differences between healthy knees and those afflicted with osteoarthritis and found that osteoarthritic knees produce more frequent, higher peak, and longer duration acoustic emissions compared to healthy knees [21]. Lee *et al.* also evaluated osteoarthritic subjects using an

accelerometer and successfully classified three different conditions of the patellofemoral joint [22]. To achieve such outcomes, significant work has been devoted to developing various signal processing techniques for conditioning and classifying VAG signals. Algorithms have leveraged linear prediction [23] and autoregressive modelling [22], statistical parameter investigation [24], Fourier [25] and time-frequency [26] analysis, wavelet decomposition [27, 28], and neural networks and other classifier methods such as dynamic weighted classifier fusion [24, 28].

Joint sounds are recorded either using contact microphones (e.g., accelerometers, stethoscopes) or "air" (e.g., electret, condenser) microphones, detecting the skin vibrations or audible sounds, respectively [17]. To the best of our knowledge, measurement of joint sounds has been exclusively conducted within clinical and laboratory settings, using benchtop data acquisition units [17]. Furthermore, audio recorders for health applications have been largely limited to commercially available recorders, such as professional audio equipment or smart phones [29]. While other fields, such as underwater environmental monitoring, have developed custom audio recorders using commercially available components, these recorders have either been large, consume too much current for practical wearable applications, and / or save only a compressed version or specific features of the data [30, 31]. For exploratory medical device research, uncompressed data must be recorded to allow for exhaustive investigation of the signals for clinically-relevant features. While future designs may employ compression algorithms to limit data storage load, new algorithms will likely need to be derived, which will retain knee joint health features, unless a lossless technique is used. Moreover, real-time, on-board processing may be leveraged pending determination of robust extraction of features, a small feature space, and the lightweight algorithm complexity.

2.1.2 Edema and Electrical Bioimpedance

Edema, or swelling, is a common symptom following an injury or when suffering from the effects of a disorder. Edema is typically evaluated in the clinic by visual inspection, circumferential measurements, or imaging [32,33], which do not provide a quick and practical way to quantitatively assess edema, especially for continuous monitoring. Continuous and longitudinal monitoring may be employed to make informed decisions regarding return-to-play following an injury or for medication and treatment plans for those with arthritis.

Electrical bioimpedance (EBI) is a mechanism that can be used to measure edema [34]. This measurement injects a known current into the body and measures the potential difference across this area. Using the ratio of voltage and current, the impedance—both the resistance and reactance—of the tissue is calculated [35]. Because elements of the tissue (namely fat, bone, and muscle) as well as fluid, air, and blood have different conductivities, EBI can infer composition changes within the volume of tissue. These changes contribute to the static and dynamic components of the signal; structural changes or swelling vary over the course of hours to days, while local blood flow occurs on the millisecond scale. With edema, the increase in fluid within the tissue corresponds to a decrease in resistance [36]. Further, damaged cell membranes, which may present with an injury, manifests as a decrease in capacitance and thus reactance [36]. In this way, EBI is a useful technique for assessing joint health.

Design considerations for wearable applications, particularly those that are unsupervised, include user comfort and capturing contextual information for the measurements. Traditionally, "wet" or gel electrodes (e.g., Ag/AgCl electrodes) are used when measuring EBI. However, for practical, wearable measurements, dry electrodes are preferred [37], and there are many materials which can be used as "dry" electrodes, including conductive textiles, carbon-doped electrodes, and various metals, though these materials suffer from a higher electrode-skin interface impedance compared to gel electrodes [38, 39]. Moreover, given posture and motion artifacts can impact the signal (described in the next section),

leg orientation and motion should be measured. Skin temperature should be acquired to provide additional context, as heating and cooling of the skin increases and decreases interstitial fluid volume, respectively, due to changes in the dilation and constriction of blood vessels, which effect filtration and absorption processes [40]. Skin or knee temperature may change due to environmental changes or activity level.

2.1.3 Inertial Measurement Units

A large portion of the research related to wearable knee joint health assessment leverages inertial measurement units (IMUs), performing gait analysis, activity detection, and kinematic evaluation. IMUs consist of two to three sensors: accelerometers, gyroscopes, and magnetometers, which measure acceleration, rate of rotation, and magnetic field, respectively. While the output from a single one of these sensors can detect specific information (e.g., activity detection from an accelerometer [41]) or be used to mine features for machine learning algorithms [36], sensor fusion algorithms combine the output from most or all of the sensors to calculate absolute orientation of the IMU itself, capturing a more complete model of motion in space [42–44]. Using two IMUs placed on the thigh and shank of the leg, joint angle is computed using the IMUs' absolute orientation or some scheme [42, 45].

On their own, IMUs generally do not provide enough information to discriminate small physiological changes because they do not directly capture the underlying structure and pathology. However, tracking motion of the knee has proven to be an important during rehabilitation and for managing arthritis given its relatively easy accessibility. Range of motion and mobility is an important marker used by physicians when evaluating joint health, as it may correlate with or indicate adverse functional outcomes: extreme swelling, joint stiffness, limited extension capabilities, and possible pain [46, 47]. Moreover, along with other criteria, confidence and capability to perform plyometric exercises that rely on proprioception are commonly used as metrics for return-to-play decisions [47]. As such, these measurements may provide vital features to be used in joint health score machine learning

algorithms.

Furthermore, IMUs can be used be used to improve the signal quality of other sensing modalities by gating measurements that may be corrupted by motion artifacts and / or orientation. For example, EBI measurements for knee swelling are influenced by motion and limb orientation and may obscure changes in the signal due to physiological changes; using IMUs to identify correct subject posture and stillness can ensure valid comparisons between left and right legs and provide repeatable measurements for use longitudinal analysis of swelling [36]. For joint acoustical emissions, loud sounds due to initial heel strike may be eliminated in walking data [48, 49].

Lastly, IMUs may provide contextual information for the other sensing modalities. For joint sound measurements, joint angle or velocity would provide context for where in the range-of-motion acoustic emissions occur, for example [50–52]. Given that joint sounds are not thoroughly understood at this time, such physiological information may aid researchers discover joint acoustic origins, properties, and signatures as well as convey these findings to clinicians.

2.2 The Advantage of Multimodal Sensing for Knee Health

Lack of low-cost, easily accessible, quantitative longitudinal assessment tools for tracking knee injuries and diseases represents a significant gap in technology available to both clinicians and patients. In this section, we examine the rehabilitation protocol following an anterior cruciate ligament (ACL) reconstructive surgery given the injury's high incidence rate and lengthy rehabilitation process [53–55]. In the following sections, we propose how the various sensing modalities of joint health may be leveraged at different stages of rehabilitation.

2.2.1 Immediately Following Surgery

Immediately following surgery, patients are typically equipped with a Cryo/Cuff and are instructed to apply the cold-compression treatment in an effort to reduce swelling and improve outcomes [56, 57]. Therapies at this stage can be critical, as continuous combined cold / compression yielded reduced swelling, decreased pain and painkiller usage, and improved functional knee scores than just ice bag treatments, for example [58]. Furthermore, using this therapy, patients achieved full extension earlier and more predictable rehabilitation progression [59]. During this period, EBI may be used to track swelling and identify changes in swelling that cannot be detected by visual inspection or tape measures. Moreover, rather than discrete measurements taken at a physical therapy office, continuous monitoring of EBI may be considered, as Cyro/Cuff therapy is around-the-clock following surgery.

Range-of-motion (ROM) is another large focus immediately post-operatively given restoration of full ROM is a primary objective during rehabilitation. Accelerated rehabilitation protocols call for ROM tasks (e.g., heel slides, leg lifts, hyperextension exercises, etc.) the day after surgery with some patients using continuous passive movement machines to supplement these exercises [57, 60, 61]. Such accelerated programs achieve full ROM faster than traditional programs [62]. During these ROM exercises, IMUs may calculate joint angle without the need for repeated measures, perhaps, as is recommended for clinicians to minimize error when using goniometers [63, 64]. Furthermore, IMUs would facilitate quantitative ROM measurements when the patient completes at-home exercises. When used in conjunction with EBI, possible changes in swelling may be measured and correlated with exercise intensity or time of completion.

Finally, joint sound measurements would be primarily used as a baseline measurement, as the underlying structural integrity of the joint is known by the clinician and patient to be severely compromised. This baseline measurement would help facilitate longitudinal comparisons of the structure of the joint, speculatively providing the worst-case (“unhealthiest”)

sounds for the given patient's knee.

2.2.2 Rehabilitation Period

During the core rehabilitation phase, we anticipate all sensing modalities may be used, especially when moving towards more complex tasks. There are many functional milestones during rehabilitation following ACL reconstruction, including the transitions from braced to unbraced walking, from walking to running, and from running to cutting motions—to name a few. Current rehabilitation protocols are no longer dictated by prescribed timelines and are instead driven by patient progression; as such, clinicians are tasked to pace therapies based on evaluated patient—and healing ACL's—readiness [55]. For example, ROM and swelling should be continuously monitored; at the extreme, if ROM decreases and / or swelling occurs, activities should be reduced and reevaluated to prevent long-term complications [57, 65]. Given the patient is already relearning movements, it would be prudent to incorporate concepts from ACL prevention training programs, such as those aimed at improved proprioception and jumping techniques as well as an emphasis on plyometric and strength training, which have been shown to reduce injury risk [66, 67]. During such tasks, IMUs, joint acoustics, and EBI may be used to quantitatively evaluate and / or reveal improper kinematic technique, undesirable loading of the joint, and acute inflammatory responses, respectively.

2.2.3 Return-to-Play Evaluation

When deciding on returning to play, joint acoustics and IMUs will be the most important sensing modalities, as the rehabilitated knee should not exhibit swelling at this point. Functional tests, isokinetic strength tests, and clinical outcome scores (e.g., surveys) are common metrics for determining patient readiness [68]. Notably, none of these measures directly provide information regarding the *underlying* structural integrity of the joint but are largely aimed at ensuring a decreased risk of re-injury. The analysis of joint acoustics

may provide such insight to the joint itself, especially when compared against baseline or even possible population-generalizable recordings. In addition to within-knee longitudinal analyses, measurement of the contralateral knee may provide "normal" (or "expected" / "healthy") standard for the rehabilitated knee [36]. Moreover, side-to-side differences may be evaluated, as asymmetry is considered an ACL injury risk factor [69]. Potential asymmetries can be examined in both acoustic- and inertial-based domains.

CHAPTER 3

NOVEL METHODS FOR SENSING ACOUSTICAL EMISSIONS FROM THE KNEE

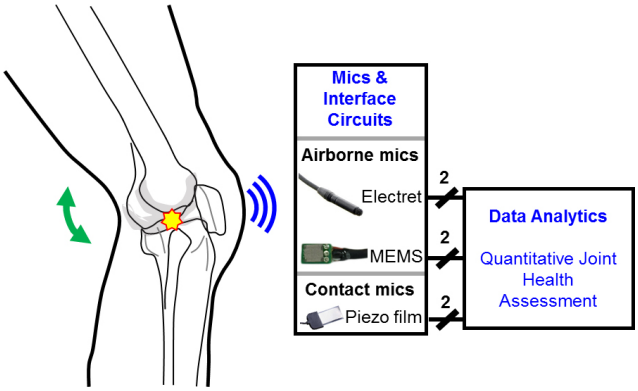

Figure 3.1: Block diagram of knee joint acoustic emissions sensing and interpretation for quantifying joint health during rehabilitation.

3.1 Introduction

Our ultimate goal is to enable around-the-clock monitoring of joint acoustics during normal activities of daily living, and prescribed rehabilitation activities that elicit specific signatures indicative of improving or worsening joint health. Towards this goal, we investigated miniature sensors that can be readily integrated into a wearable device enabling, for the first time, wearable joint acoustics sensing (Figure 3.1). Our preliminary work examined possible sensors, and findings from proof-of-concept experiments suggested that the main acoustic event during repetitive motion occurs at the same angular location [52]. However, these conclusions were reached by visual observation of the signals and failed to rigidly characterize these consistencies. Thus, one main goal of this work was to quantify the consistency of main knee joint emissions with respect to joint angle position. In particular, we focused on the analysis of airborne joint sounds, which have not been extensively studied

previously.

3.2 Assessing Miniature Microphones for Wearable Applications

This section details the initial investigation of miniature microphones for wearable applications. The sensing capabilities of various microphones are considered, specifically examining signal quality (e.g., signal-to-noise-and-interference ratio, frequencies of interest, sensitivity with respect to distance) and consistency of measurements for repeated exercises in human subjects. This work serves as the fundamental basis for wearable knee joint health assessment, as validation that microphones suited for deployable devices is contingent on robust and repeatable measurement of knee acoustic emissions.

3.2.1 System Design and Methods

3.2.1.1 Microphone Selection

When selecting the types of microphones to include in our system, we considered (1) their ability to sense acoustic emissions and (2) their practicality for integration within a wearable system. Analysis of how joint sounds propagate through the tissue and transmit to the air suggest contact microphones are the most appropriate sensor for acquiring joint sounds, and a review of prior art [17] shows that most researchers employ contact microphones successfully in *clinical / lab* applications. Contact microphones should theoretically acquire the highest quality acoustic signal since it senses the original, non-attenuated signal and is not sensitive to background noise. However, during motion and unsupervised *at-home* activity, loss of the sensor-to-skin interface is likely and of significant concern, for any compromise to the interface will be detrimental to the signal. In the extreme case that the sensor loses contact with the skin, the system will be unable to record joint sounds completely. To improve robustness, air microphones provide complementary sensing capabilities. The signal obtained by the air microphones will be inherently different from the contact microphones; the air microphones will only detect the airborne sounds: attenuated,

higher frequency signals. Additionally, while not limited by the sensor-to-skin interface like contact microphones, air microphones are much more susceptible to background noise. For these reasons, we employed both sensing modalities—contact and air microphones—to more robustly capture the acoustic emissions from the joint in future implementation in a wearable device.

For the contact microphone, we selected a piezoelectric film (SDT, Measurement Specialties, Hampton, VA) because its form factor seemingly lends itself to a wrap and other devices conventionally worn on the knee. Furthermore, piezoelectric films have wider bandwidths compared to miniature, low cost accelerometers, allowing for sensing of high frequency audio signals.

Two types of air microphones were chosen to supplement the piezoelectric film in acquiring acoustic emissions from the knee joint. The first was a commercially available electret microphone (Sanken Microphone Co., Ltd., Japan). The second was a microelectromechanical systems (MEMS) microphone, specifically the MP33AB01 (STMicroelectronics, Geneva, Switzerland), which was mounted on a custom printed circuit board (PCB). Electret and MEMS microphones sense sounds in a similar manner; however, the commercial electret microphone is much more expensive ($\sim\times 100$) compared to the MEMS microphone. The MEMS's low-cost and sensing capabilities provide a realistic solution for implementation in a wearable device; however, both the electret and MEMS microphones were used during our experiments with the electret microphone acting as the industry standard in terms of the quality of the sound acquired. For this work, we focused on the recordings from the air microphones because, at this time, they provide higher quality recordings as discussed in the results (Section 3.2.2.1). Images of the microphones used in this work (and in Chapter 4) are shown in Figure 3.2.

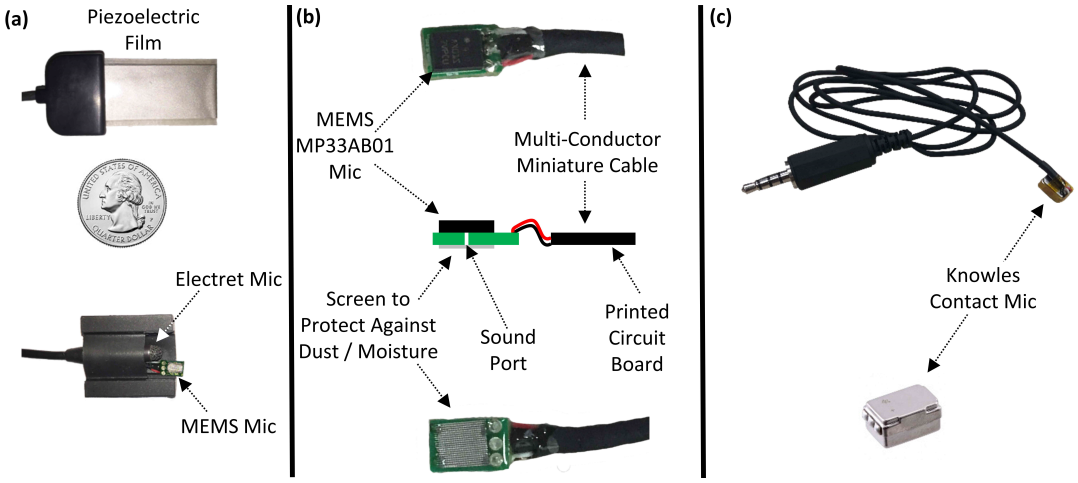

Figure 3.2: Various microphones used for recording joint sounds for our initial pilot studies. (a) Relative sizes of the piezoelectric film, electret, and MEM-based microphones. (b) Custom MEMS packaging, which includes a custom PCB mount, cabling, and stainless steel mesh for protection of the sound port. (c) Knowles contact microphone connected to an audio jack, which is used as part of the system described in Section 4.2. In part, adapted from [70].

3.2.1.2 Methods for Microphone Comparison

The similarity of the MEMS and electret microphones in detecting knee joint acoustic emissions was quantified by computing the information radius between the normalized histograms of these signals, which were acquired by both sensors at the same time placed in the same location on the lateral side of the patella. To construct the aforementioned histograms, the signals acquired from the microphones were first normalized such that their amplitudes were limited to the range [0, 1]. The histogram was formed from this normalized signal using 1000 bins.

Next, the quality of each sensor was evaluated by computing the signal-to-noise-and-interference ratio (SNIR). The SNIR for each microphone was calculated by finding the ratio of the peak power of a "click" (i.e., acoustic emission) emitted by the knee joint to the peak power of interface noise in the vicinity of the click. For this calculation, acoustic emissions from the microphones positioned at the medial side of the patella for the air microphones and distal side of the patella for the contact microphone were used.

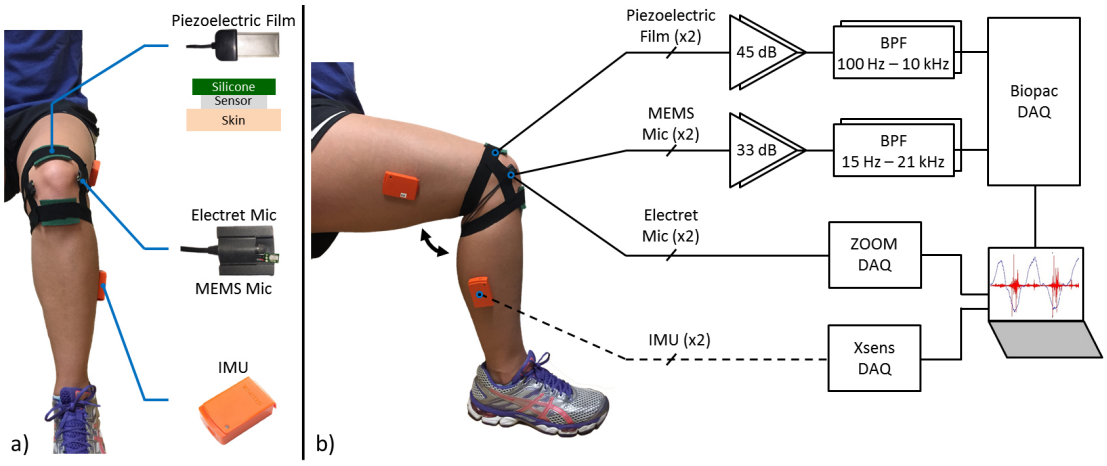

Figure 3.3: Sensor placement and measurement block diagram. (a) Eight sensors were used during human subject testing: two IMUs placed laterally on the thigh and shank; piezoelectric film sensors placed proximal and distal of the patella; and air microphones (MEMS and electret) attached on the lateral and medial sides of the patella. (b) Block diagram of the data collection hardware.

Lastly, a proof-of-concept experiment was conducted to compare signals measured on and off of the skin. A subject performed three cycles of seated, unloaded knee flexion / extension with two electret microphones positioned at the lateral side of the patella, one on the skin and one located 5 cm off the skin. The resulting signals were then compared.

3.2.1.3 Interfacing Circuits

The analog front-end for the MEMS microphones consisted of a non-inverting amplifier stage with 33 dB gain, which was selected such that the signals do not saturate but are amplified to utilize the full dynamic range of the subsequent analog to digital converter, and a high-pass 15 Hz cutoff frequency. This stage was followed by a second-order low-pass filter with a cutoff frequency of 21 kHz. A bandwidth of 15 Hz – 21 kHz was chosen, as knee joint sounds can range between these frequencies [17].

The analog front-end for the piezoelectric film microphones consisted of an amplification stage of gain 45 dB and 100 Hz high-pass cut off. This stage was followed by a fourth-order low pass filter with a 10 kHz cut-off frequency. A 100 Hz high-pass cut off

was chosen to attenuate the interface and motion artifact noise.

3.2.1.4 Human Subject Study and Measurement Protocol

Thirteen male subjects without history of knee injuries participated in the study and gave written informed consent approved by the Georgia Institute of Technology Institutional Review Board (IRB) and the Army Human Research Protection Office (AHRPO). The subject population was reasonably homogenous in terms of physical activity level (collegiate athletes) and ranged in age (19 – 21 years), weight (84.1 – 135.3 kg), and height (174 – 195 cm). With this approach, our plan was to assess the variability in the measurements separately from variability due to age or knee joint health. Following preliminary measures of body composition and height, weight, an electret and MEMS microphone were both positioned at the lateral and medial sides of the subject's patella targeting the patellofemoral joint while two piezoelectric film sensors were placed on the skin just proximal and distal to the patella. Each sensor was attached using Kinesio Tex tape. In addition to the tape, a thin piece of silicone (5 mm thick) was placed over the piezoelectric film to reduce the interface noise of the tape rubbing against the film. Lastly, two wireless inertial measurement units (IMUs) (MTW-38A70G20, Xsens, Enschede, The Netherlands), which contained three-axis accelerometer, gyroscope, and magnetometer as well as built-in sensor fusion outputs, were positioned on the lateral sides of the thigh and shank. These sensor placements are displayed in Figure 3.3(a). Data collection was completed with Dr. Sinan Hersek of the Inan Research Laboratory and Michael L. Jones of the Exercise Physiology Laboratory at the Georgia Institute of Technology.

While wearing these sensors, each subject completed two exercises: (1) seated, unloaded knee flexion / extension and (2) sit-to-stand. For each exercise, the subject repeated the motion five times while the microphone and IMU outputs were recorded in a quiet room (Figure 3.3(b)). The signals from the piezoelectric and MEMS microphones were passed through custom circuits and then collected at 50 kHz (16 bits/sample) using Biopac data

acquisition hardware (Biopac Systems Inc, Goleta, CA) while the signals from the electret microphones were sampled at 44.1 kHz (16 bits/sample) using a Zoom H6 recorder (Zoom Corp., Tokyo, Japan). The IMU signals were acquired at 50 Hz (16 bits/sample) using their device-specific software suite (MT Manager, Xsens, Enschede, The Netherlands) synched with the Biopac system. Apart from the electret microphone signals, which were stored on an SD card (SanDisk, Milpitas, CA) via the Zoom recorder, all signals were recorded on a laptop. The data were then processed using MATLAB (The Mathworks, Natick, MA).

3.2.1.5 Joint Sound Processing

The signal processing consisted of (1) calculation of knee joint angle and contextualization of the joint sounds with joint angle, (2) identification of significant high frequency acoustic emissions or clicks, and (3) statistical analysis to quantify the consistency of occurrence of the main clicks with respect to joint angle.

First, the knee joint angle was calculated using the methods described in [42], which leverage the sensor fusion outputs of 3-axis accelerometer, gyroscope, and magnometer provided by Xsens, namely the rotation matrix (i.e., Direction Cosine Matrix), and the kinematic constraints of a hinge joint to provide angle data. This method allowed for arbitrary sensor placement and orientation on each segment of the joint (i.e., thigh and shank), eliminating the need for precise calibration techniques and measures [42]. However, this method is potentially susceptible to error, due to deviations from a true hinge joint as a result of skin and motion artifacts [42]. Nevertheless, since we analyzed the cycles of repetitive motions against one another, this error was common to each cycle and thus did not present in our results. Finally, the signal was normalized between 0° and 90° such that subjects could be compared against one another with respect to location within each subject's range of motion.

Next, significant acoustic emissions were identified. This work was completed with Dr. Sinan Hersek of the Inan Research Laboratory. The most distinct audio signals that were

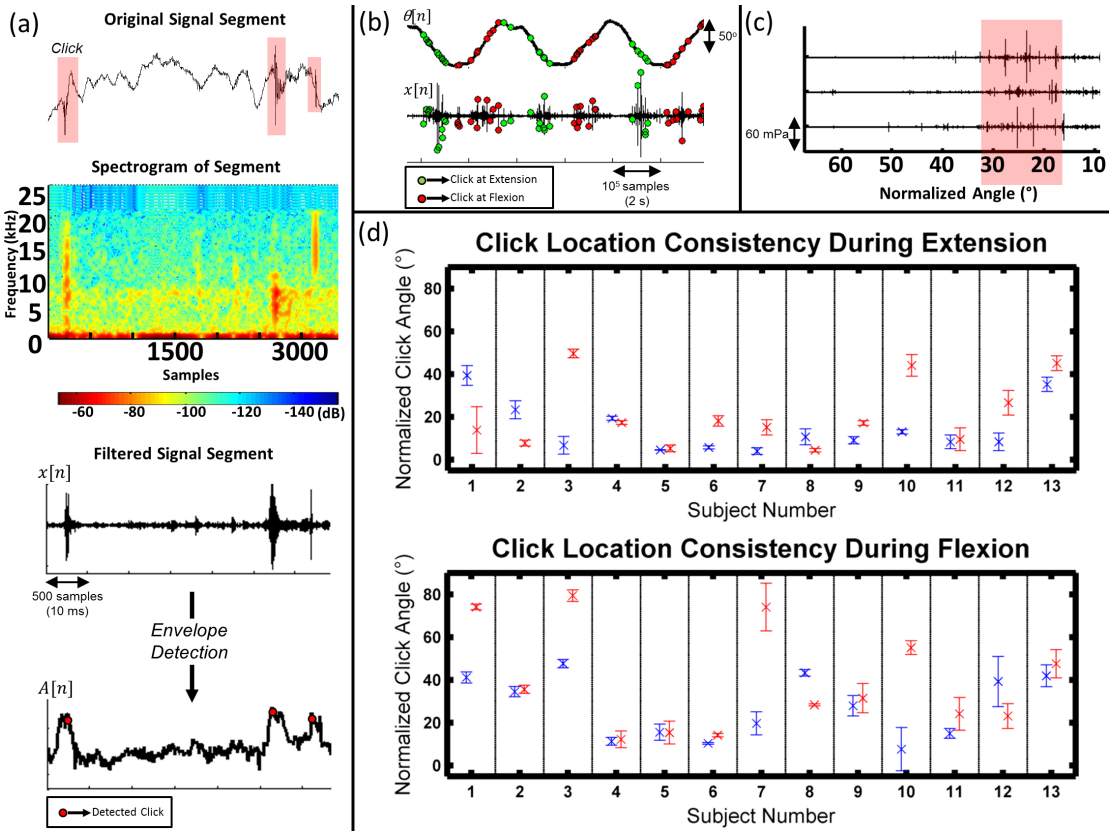

Figure 3.4: Joint sound processing of recordings taken with an electret microphone positioned at the lateral side of the patella (a-c) and results (d). (a) An example 3000 sample (60 ms) joint sound recording window showing three distinct high-amplitude, short-duration acoustic emissions. The original signal contains ambient noise, which presents as broadband signals up to 7 kHz, and interface noise, which appears as baseline movement. These components are clearly visualized in the spectrogram of the original signal. To remove the majority of the noise, the signal is bandpass filtered at 7 kHz - 16 kHz, resulting in the filtered signal $x[n]$. The envelope of this signal is found, yielding $A[n]$. Using a thresholding technique based on the moving average, the significant peaks of $A[n]$ are found, roughly corresponding to the clicks of the original signal. These are later refined to match the true locations of the clicks found in the original signal (i.e., such that the locations correspond to where the clicks achieve their maximum amplitudes, positive or negative, in the original signal). (b) Final result of the click detection algorithm, which displays the identified clicks for three cycles of flexion / extension. (c) Three extension cycles with artificial offsets. These qualitatively show that the main acoustic event of each cycle occurs at similar angular locations. (d) The final results of click location consistency for five repetitions of flexion / extension for 13 subjects on left (blue) and right (red) legs. Across subjects, the standard deviation for click location is small, supporting observations of consistent angular location cycle-to-cycle. Additionally, the mean locations of these clicks are consistent between left and right legs for most of the subjects.

detected by the air microphones were the high amplitude, short duration clicks (Figure 3.4(a)). By observing the signal's frequency content (i.e., short-time Fourier transform, STFT), these clicks were broadband with frequencies as high as 20 kHz. This unfiltered signal contained two main sources of noise; ambient noise ranged in frequency up to 7 kHz while interface noise appeared as baseline movement with components up to 1.5 kHz. The first step of this identification stage was to preprocess the signal such that the clicks became more prominent and any interface and / or ambient noise were mostly cancelled. To this extent, the air microphone signals were filtered with a bandpass filter spanning 7 kHz – 16 kHz. As seen from Figure 3.4(a), the filtered signal ($x[n]$) lacks the original baseline movement, and the clicks are more distinct from other artifacts in the signal.

After this preprocessing step was complete, a modified envelope detection algorithm was implemented. A 1024-bin spectrogram of the signal ($X[n, m]$) was calculated with a window size of 100 samples (i.e., 2 ms) and 90% overlap. The amplitude of the signal was calculated by summing the logarithmic amplitude of the spectrogram across the frequency bins as follows:

$$A[n] = \sum_{j} 20 \log \mid X[n, j] \mid \tag{3.1}$$

A moving average and standard deviation ($\mu[n]$ and $\sigma[n]$) of $A[n]$ using a window size of 1000 samples was calculated. $A[n]$ was then thresholded such that

$$T[n] = \begin{cases} A[n], & A[n] > \mu[n] + \alpha \cdot \sigma[n] \\ 0, & \text{otherwise} \end{cases} \tag{3.2}$$

where $T[n]$ is the thresholded amplitude signal and α is a constant control coefficient, which was selected as 3.3 by inspection.

Next, the peaks of $T[n]$ were detected by standard peak detection techniques. The peaks that resulted from the same click (i.e., resonances of the initial click, which are specified as peaks within 150 samples of each other) were eliminated, resulting in the raw click

locations vector $p_{\mathrm{r}} = [p_{\mathrm{r}1}, p_{\mathrm{r}2}, ..., p_{\mathrm{r}L}]$. The raw click locations p_{r} were refined such that each click location corresponded to the point on the original filtered signal where the click achieved its maximum amplitude, positive or negative. The refined click locations matrix $p = [p_1, p_2, ..., p_{\mathrm{L}}]$ gave the final detected click locations. An example of these detected clicks is shown in Figure 3.4(b).

Once the clicks were identified, we analyzed the consistency of these acoustic emissions. Figure 3.4(c) provides a visualization of consistent acoustic emission during repetitive motion. For each cycle of a particular exercise (i.e., flexion or extension), the three clicks with the largest amplitudes and their corresponding angular locations were determined. Each combination of the clicks across cycles (i.e., selection of one of the three clicks from each cycle) was found. The combination with the smallest standard deviation for angular location yielded the most consistently occurring major acoustic event. The mean and standard deviation of these locations were calculated.

Given these mean locations, three methods were used to analyze the data. For the first two methods, test-retest reliability was estimated using the intraclass correlation coefficient (ICC). We organized the data into "motions" and "repetitions." There were 52 "motions," one for each human subject and exercise combination (e.g., subject 1's extension data represented one "motion"). The "repetitions" consisted of the five click locations (one per cycle) from the selected combination. This dataset will be referred to as the test-retest dataset. Given this dataset, two ICC values were calculated using one-way random single (i.e., ICC(1, 1)) and average measure (i.e., ICC(1, k)) models to show the reliability of a single cycles' measure and mean of the fives cycles' measures. Additionally, the 95% confidence intervals (CI) for these two ICC values were determined. The last method for analyzing the data was a paired t-test, which was used to assess whether there were significant differences between the mean click locations for left and right legs.

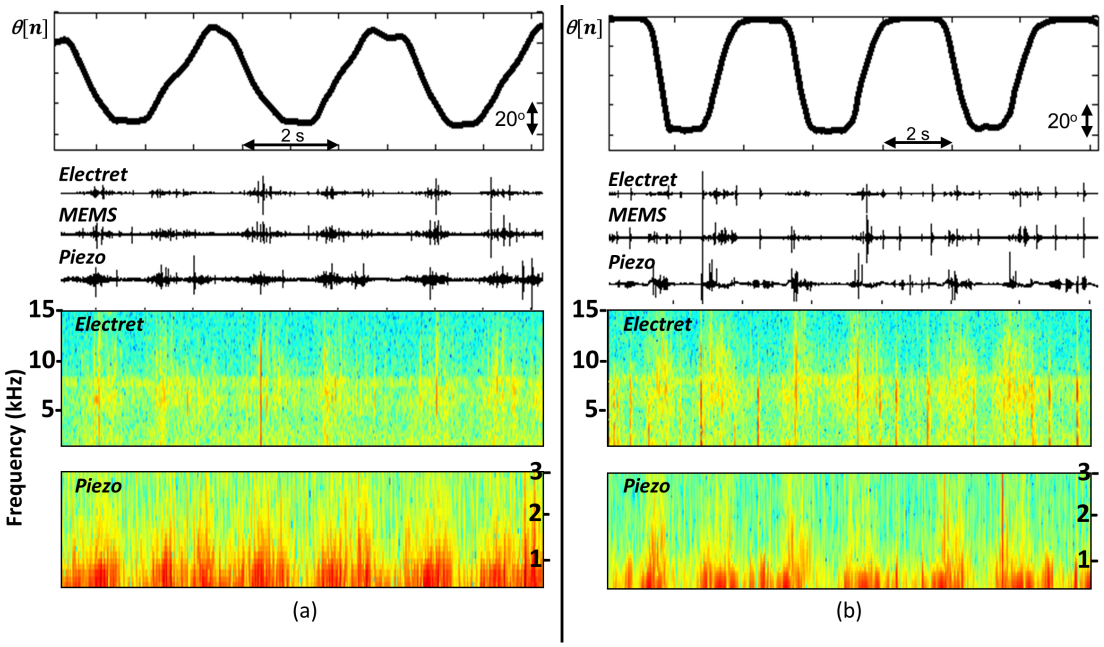

Figure 3.5: Joint sounds simultaneously sensed by electret, MEMS, and piezoelectric film microphones during three repetitions of (a) flexion / extension and (b) sit-to-stand exercises. For both parts (a) and (b), the top plot displays the joint angle (θ[n]). The middle and bottom graphs show the time and frequency domain signals from the various microphones. (The acoustic signatures of the electret and MEMS microphones exhibit similar characteristics.)

3.2.2 Results and Discussion

3.2.2.1 Microphone Comparison

In evaluating our microphone selection, we considered many different parameters. First, we compared the similarity of the signals measured by the electret and MEMS microphones. We also determined the quality of these microphones by evaluating the quality of their sensing capabilities in terms of SNIR. Moreover, when investigating the interface issues for the air microphones, we examined the effect that proximity of the sensor to knee had on the signal acquired. Finally, we researched the quality of the contact microphone.

As shown in Figure 3.5(a) and (b), the electret and MEMS microphones, measuring frequencies as high as 20 kHz, performed similarly in detecting joint sounds, which were acquired from a subject performing flexion / extension and sit-to-stand exercises respec-

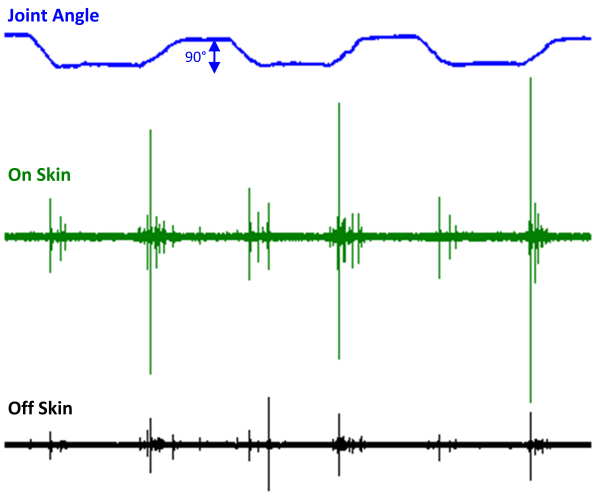

Figure 3.6: Joint sounds measured on the skin and 5 cm off the skin during flexion / extension exercises. Though the off-skin microphone captured a signal with decreased amplitude, the on- and off-skin measurements showed significant similarities in their acoustic signatures. The main acoustic event of each signal occurred at similar locations.

tively. This was confirmed by computing the information radius between the normalized histograms of signals captured by these two microphones, which yielded a value of 0.0025. This value shows a high similarity between these two types of microphones since the information radius ranges from 0 for identical distributions to 2 for maximally different distributions [71]. This shows that the more cost-effective MEMS microphones are a viable substitute for the more expensive electret microphones. This is an important result when designing deployable systems.

As predicted, the signal recorded by the air microphones included noise and interface components in addition to the desired joint sounds; both ambient background interference and interface noise caused by the rubbing of athletic tape, which was used to hold the sensors in place, were sensed by the microphones. The SNIR was 11.7 dB for the electret microphone and 12.4 dB for the MEMS microphone. To minimize issues with noise during initial experiments, measurements were taken in a quiet room; however, this will need to be addressed for implementation of a deployable, wearable system, especially given the fact that many ambulant sounds, such as speech, will reside in-band with the joint sounds.

One important observation made during proof-of-concept experiments showed that the air microphones did not need to be directly located at the skin surface to detect airborne joint sounds. As shown in Figure 3.6, the sounds obtained from an electret microphone placed on the skin and one located 5 cm off the skin captured similar acoustic signals in both morphology and timing ($\sim$4.5$\times$ smaller amplitude). This is an important observation because it suggests that the air microphones will be able to record joint sounds in a wearable device where direct contact with the skin may not be constant. However, it will be important to consider this distance when analyzing the captured signals, particularly when the analysis depends on the amplitude of the signal. In this sense, maintaining a fixed distance between the microphone and skin, especially for use in longitudinal analysis, will be required. Furthermore, placing the microphone off of the skin introduces increased potential for noise; the microphone may have a greater opportunity to strike or rub against the skin. Additionally, changing the distance between the microphone and skin will change the microphone's sensitivity in sensing these sounds. These issues must be addressed in the design of a wearable system.

The piezoelectric film measured signals up to approximately 3 kHz as seen from the spectrograms of the signals acquired shown in Figure 3.5. While the piezoelectric film had the advantage of not detecting background noise, it acquired significantly more interface noise—8.4 dB SNIR—due to the sensor rubbing on the skin and the athletic tape rubbing on both the skin and the sensor. This interface noise had frequency components up to 1.5 kHz, and was thus in-band.

During early pilot data collections, the piezoelectric film was attached to the skin using only Kinesio Tex tape. However, this method proved to be very susceptible to interface noise; as the knee extends and flexes, the tape, though stretchable, deformed the film which obscured the low frequency and low amplitude signatures. Furthermore, though acceptable for collecting pilot data, tape proves to be undesirable for long-term monitoring. To mitigate this issue, a piece of silicone was placed above the piezoelectric film. Because

silicone has similar compliant mechanical properties to skin and subcutaneous tissue, the joint sounds received did not experience dampening, and the silicone surface provided a suitable surface to stick the tape. Though this method did not completely eliminate interface noise—the sensor still experienced some movement along the skin—it did help to reduce the recorded noise.

Accordingly, while using piezoelectric film or other contact microphones is desired to capture the vibration signal, which represents the majority of the acoustical energy generated, implementation presents practical issues. The piezoelectric film was significantly affected by interface noise; a smaller portion of the signal bandwidth was corrupted by interface noise for the air microphones compared to contact microphones. Furthermore, contact microphones did not pick up higher frequency vibrations as distinctly as air microphones. For these reasons, piezoelectric film as a contact microphone is not recommended at this time.

3.2.2.2 Joint Sound Consistency

Figure 3.4(d) summarizes the results for mean angular click location for the left and right legs of 13 seated subjects performing five repetitions of knee flexion / extension. Two important findings resulted from this data: (1) significant acoustic events are repeatable during single trial measures and (2) left and right legs produce similar sounds.

First, two ICC values were found for the test-retest dataset. An ICC(1,1) value of 0.94 with a 95% CI of 0.92 – 0.97 and an ICC(1, k) value of 0.99 with a 95% CI of 0.98 – 0.99 were calculated. Since the ICC values were greater than 0.7, these values showed that the main acoustic emission per cycle of activity were consistent within a single trial of monitoring for both single and average measure reliability [72]. Given that audible joint sounds have not been extensively explored, this was an important finding, demonstrating that airborne signals emit a stable pattern with repeated movement in a healthy hinge joint.

Second, the difference between legs for each exercise suggested that a healthy subject's

knees produce similar joint sounds; the difference between left and right legs were not significant at the $p < 0.05$ level. While as a group, there were no significant differences between the left and right legs, some subjects could be grouped as having relatively no difference between right limb and left limb click locations whereas others had notable differences between right and left suggesting the potential for defining clinically relevant "signature traits." Such variations in click location could represent useful knee joint health biomarkers.

Though these results are promising, there are some limitations to our current system and analysis. First, with regard to the IMUs, sensor positioning, drift, and motion artifacts can all contribute to flexion angle calculations that differ from the true joint angle. Techniques will need to be employed to minimize these errors, especially when considering their application in a system which measures longitudinal data. For example, ensuring more rigid sensor positioning [42] and leveraging the joint's kinematic constraints directly into the calculation of joint angle to minimize the effect of drift [73, 74] could potentially minimize error. Second, the effect of lubrication (e.g., diminished boundary lubrication after an injury [75]) and differing structural components (e.g., damaged ligaments [76], etc.) on acoustic emissions has not been sufficiently studied. These variables may introduce "error" when calculating click location consistency for repeated cycles and measuring differences between legs. In this sense, these isolated, one-time measurements may not prove to be as useful as compared to longitudinal analysis for the same subject over time. Future work is required to determine the efficacy of these observations as clinically relevant data.

3.2.3 Conclusions for Initial Microphone Investigation and Future Work

This section describes the measurement and analysis of acoustic emissions from the knee joint during loaded and unloaded activities. We demonstrated, quantitatively, that major acoustic events occur at consistent joint angles during repetitive motions for healthy subjects. Furthermore, we observed that these locations are similar between left and right legs

for most subjects. Whether asymmetry between right and left knee acoustic emissions is related to risk factors for injury or other training-related variables remains to be clarified. Importantly, these findings showed that joint sound measurements from air microphones are repeatable, with sensing technology that can be implemented in an inexpensive, wearable form factor. While extensive analysis of the piezoelectric film was not conducted in this work due to corruption of the signal with interface noise, we believe its use in a wearable device holds promise based on our preliminary findings showing that packaging techniques have a large influence on the signal recorded.

Future work will include mitigating background and interface noise for both the air and contact microphones. In particular, the focus should be on the packaging of these sensors into a wearable wrap or sleeve enabling high quality signal measurements during at-home, long-term monitoring. Additionally, existing algorithms should be refined and new processing techniques developed to detect clinically-relevant acoustic signatures. Given that therapists and clinicians look at sounds, swelling, structural stability, and range of motion, researchers should investigate methods for quantifying these joint health biomarkers unobtrusively and accurately; namely, they should determine which acoustic signatures encapsulate these biomarkers. Furthermore, exploration of these biomarkers as they relate to specific diseases and injuries (e.g., osteoarthritis, anterior cruciate ligament tear, meniscal tear, etc.) should be considered. Finally, longitudinal studies on injured subjects will allow determination and validation of specifics acoustic emission features (e.g., consistent angular location) that provide valuable joint health information during rehabilitation following an acute injury.

3.3 Supplemental Human Subject Studies

The work presented in the previous section of this chapter was the product of the initial phase of a larger human subject study and was primarily used to validate preliminary sensing techniques (e.g., we decided to exclude data from the piezoelectric films in processing

schemes given its poor SNR). Ultimately, we collected data from 49 healthy subjects (50 total were recorded though one was excluded due to hardware failure) and nine subjects with recent knee injuries at the acute stage and following rehabilitation using the protocol presented in Section 3.2.1.4. This section describes some of the results derived from this dataset: (1) expansion of the significant acoustic event analysis to the entire subject population, (2) discrimination of healthy and injured knees, and (3) comparison of injured knees pre- and post-rehabilitation. The first analysis is described in Section 3.3.1, while the final two are briefly summarized in Section 3.3.2.

Note that electrical bioimpedance (EBI) was also collected as part of the data collection for this study; however, the results are not presented in this dissertation. To summarize, the absolute difference in resistance (R) and reactance (X) from the left to the right knee was able to distinguish injured and healthy knees ($p < 0.05$); the absolute difference in R decreased significantly ($p < 0.05$) in injured subjects following rehabilitation [36]. This result validated using EBI—as measured using benchtop equipment—for wearable monitoring of knee joint health and, in part, provided the basis for the work described in Chapter 4.

3.3.1 Joint Acoustics Analysis for a Collegiate Athlete Population

3.3.1.1 Subject Demographics

The results in this section are derived from the entire healthy subject dataset consisting of 49 subjects (15 females) who participate in four collegiate sports: American football and basketball for the male subjects and volleyball and basketball for females. The demographic information for these subjects is summarized in Table 3.1.

3.3.1.2 Analyses for Surveying Collegiate Athletes' Knees

Two analyses were performed. The first was an expansion upon the major acoustic event analysis results (i.e., click analysis from Section 3.2.2.2). The methods described in Section 3.2.1.5 were used to find all the clicks for a given cycle for a phase of exercise. Rather than

Table 3.1: Demographic Data for Healthy Collegiate Athletes

Sex	Sport	Number of Subjects	Age (years)†	Height (cm)†	Weight (kg)†	Percent Body Fat[a] (%)†	Dominant Leg, Right
Female	Volleyball	7 (46.7%)‡	20.3 ± 0.8	70.9 ± 2.5	168.3 ± 19.0	25.2 ± 3.2	7 (46.7%)‡
	Basketball	8 (53.3%)‡	19.8 ± 1.3	71.0 ± 4.3	183.3 ± 32.1	23.3 ± 4.7	8 (53.3%)‡
	Total	15 (30.6%)§	20.0 ± 1.1	70.9 ± 3.4	175.8 ± 26.5	24.2 ± 4.0	15 (30.6%)§
Male	Football[b]	28 (82.4%)‡	19.6 ± 1.1	72.8 ± 2.8	218.0 ± 36.2	13.5 ± 5.3	25 (73.5%)‡
	Basketball	6 (17.6%)‡	20.2 ± 0.8	78.7 ± 2.9	224.2 ± 22.0	12.3 ± 2.3	5 (14.7%)‡
	Total	34 (69.4%)§	19.7 ± 1.1	73.8 ± 3.6	219.1 ± 34.0	13.2 ± 4.9	30 (61.2%)§
All	*Total*	49	19.8 ± 1.1	72.9 ± 3.8	206.5 ± 37.4	16.4 ± 6.8	45 (91.8%)§

† Indicates ($\mu \pm \sigma$).
‡ Indicates (% of total number of subjects for the given sex).
§ Indicates (% of total number of subjects).
[a] Seven-site skinfold measurement.
[b] American football.

finding the most significant click from the three loudest clicks per cycle, the ten loudest per cycle were used. We increased the number of loudest clicks used from each cycle from three to ten to expand the search space with the intent to find the "best" most consistent click (i.e., low variance for location cycle-to-cycle) and reduce the influence of errant loud clicks not necessarily attributed to joint sounds. In total, eight click locations were found for each subject, resulting in 392 total locations for 49 subjects (15 females), as each leg (right or left), microphone location (lateral or medial), and phase of exercise (extension or flexion) were considered independently. Two histograms were generated, one for flexion and one for extension, from these click locations, and probability density functions (PDFs) were fit using a kernel distribution. The histograms and PDFs were compared with results presented by Whittingslow *et al.* [77]. The study investigated acoustic emissions from cadaver knees measured using high-bandwidth accelerometer-based contact microphones with the goal of understanding underlying physiological influences on the emitted sounds. Specifically, we compare our results with the root mean square (RMS) power measured during unloaded flexion / extension.

Second, all the identified clicks for each electret acoustic signal was used to calculate the *b*-value. The *b*-value summarizes the magnitude distribution of amplitudes of acoustic

events. This metric has successfully tracked improvements in joint health status for injured knees (sampled from this dataset) following rehabilitation with the acute phase exhibiting higher acoustic emission amplitudes [78], and a similar trend was observed in cadaver studies that compared baseline measurements with recordings following an induced meniscus tear [77]. In total, 196 *b*-values were calculated from the dataset where each *b*-value represents is extracted from an audio signal consisting of five flexion / extension cycles for a given subject, leg (self-reported dominant or non-dominant), and microphone location (lateral or medial). Note that the *b*-value calculation, though using the same mathematical formulas presented in [78], leveraged the pre-processing and click identification methods presented in this dissertation, and as such, the absolute values may be different compared to those reported in that in [78].

To assess whether *b*-value differed by either sex or leg dominance, a linear mixed effects model was used with sex (male or female) and leg dominance (dominant or non-dominant) treated as fixed effects, subject as a random effect, and microphone location as a covariate. Multiple permutations of the random error structure were tested, with the addition of microphone location or leg dominance not offering any improvement in model fit as determined by Akaike information criterion (AIC) and direct model comparisons from the analysis of variance (ANOVA) function within R (r-project.org [79]). The model was checked for fit using residual and Q-Q plots, which did not reveal any systemic errors or biases within the fitted values. When significant main effects were returned, *a priori* planned comparisons were completed (1) between sexes at each level of leg dominance and (2) leg dominance at each level of sex using pairwise post-hoc comparisons from the emmeans package in R (cran.r-project.org/web/packages/emmeans [80]). The *a priori* alpha level was set at $<$ 0.05. These comparisons were repeated for a subset of the data, specifically examining men and women basketball players (N = 15, 8 females) to complete a direct sport-matched comparison. Moreover, because the female athlete subject population consisted solely of jumping-based sports (volleyball and basketball) while the male athlete subject popula-

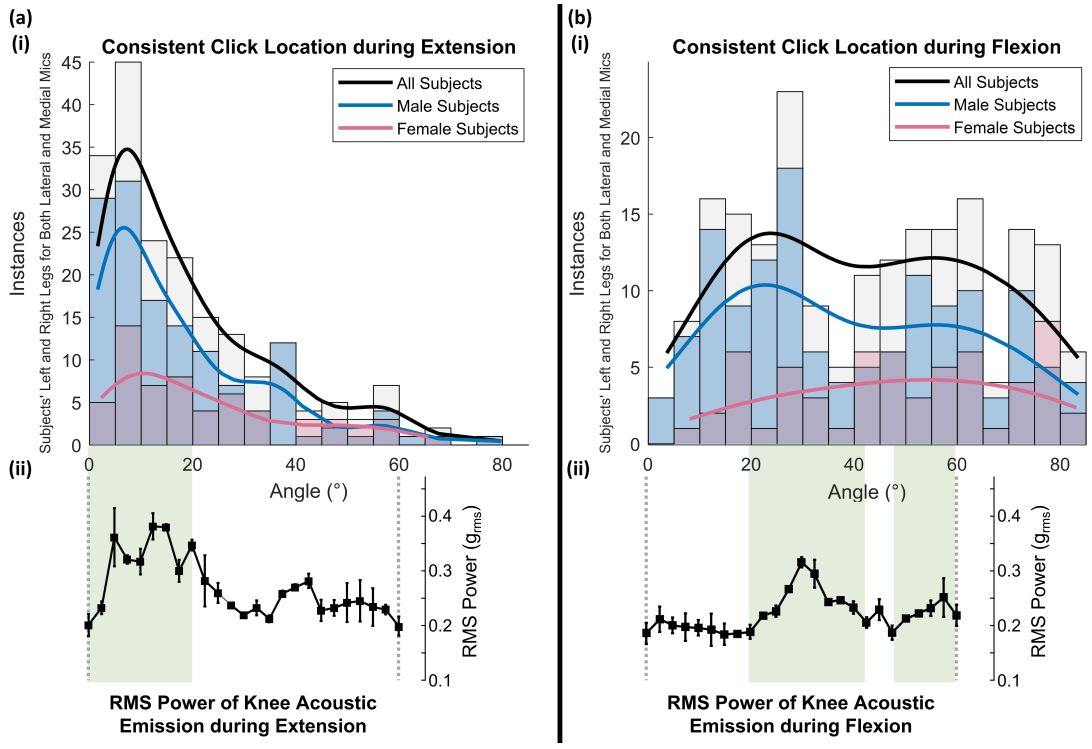

Figure 3.7: Consistent click location for healthy collegiate athletes (N = 49, 15 females). Histograms of the locations of the most consistent click are shown in (i) of (a-b). There are 196 location instances plotted for each histogram; one point represents the most consistent click location for a given subject, leg (left or right), and microphone location (lateral or medial) across five cycles. Histograms for the all subjects (gray) as well as histograms for the subsets of male and female subjects (blue and pink, respectively) are presented. The probability density function fit using a kernel distribution are superimposed on the histograms as solid lines. The histograms for the healthy subject data (measured with electret microphones) are compared against the root mean square (RMS) power of joint acoustics of cadaver knees as measured by contact microphones (ii of a-b), which are redrawn from [56] with a conversion to flexion angle. Though not a direct comparison since the sensing modality (air-based electret vs. contact-based accelerometer) and data (most consistent occurring loud click location vs. RMS power) are different, similarities are observed when comparing the healthy and cadaver knees. For extension (a), clicks and high RMS power most frequently occur when the leg is nearly fully extended, while for flexion (b), a bimodal trend is observed.

tion included a prevalence of football players (N = 28 football vs. N = 6 basketball), this comparison aimed to eliminate the influence of sport-related differences.

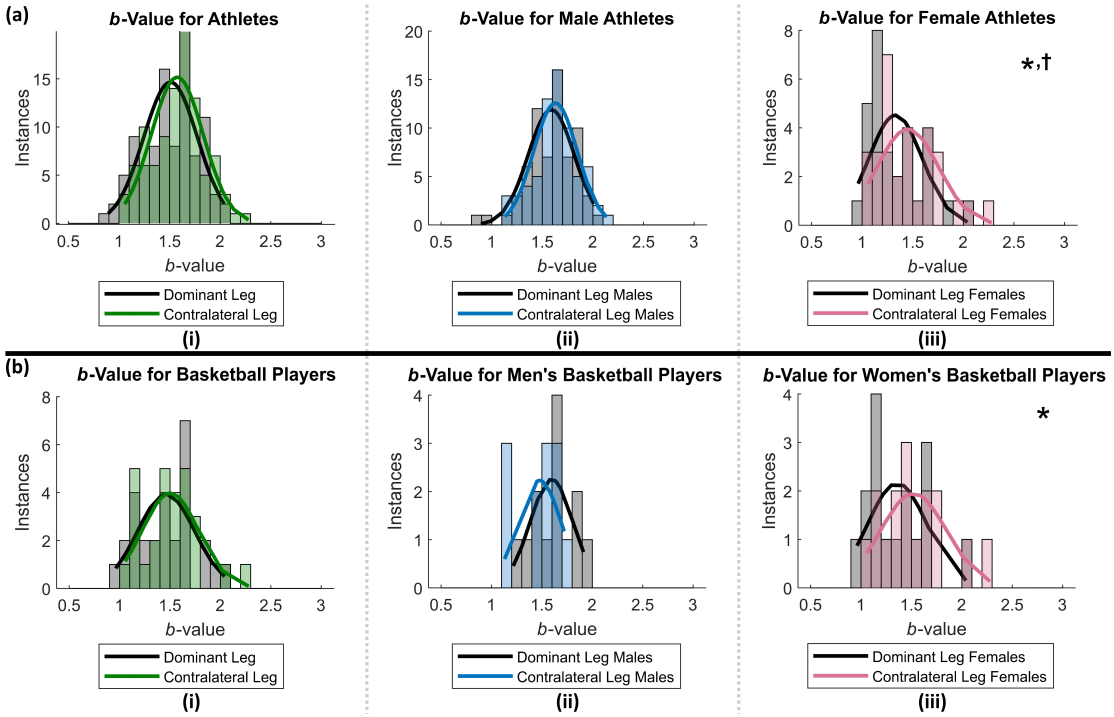

Figure 3.8: *b*-value for healthy collegiate athletes (N = 49, 15 females) calculated from five cycles of flexion / extension. Each instance plotted within a histogram represents the *b*-value for a given subject, leg (left or right), and microphone location (lateral or medial) as measured by electret microphones. The probability density function fit using a normal distribution are superimposed on the histograms as solid lines. The histograms compare the difference in *b*-value between the subjects' self-reported dominant and non-dominant (contralateral) leg for (a) all subjects and (b) for basketball players (N = 14, 8 females), specifically. For (a-b), histograms are provided for (i) all, (ii) male, and (iii) female subjects. A significant difference (*p $<$ 0.01) was observed between the females' dominant and non-dominant leg for both the total female athlete population (a-iii) and just those who played basketball (b-iii). Further, a significant difference (†p $<$ 0.0001) was observed between all male (a-ii) and female (a-iii) athletes' dominant legs but was not significant (p = 0.08) when comparing men (b-ii) and women (b-iii) basketball players' dominant legs. This implementation of the *b*-value, initially used in seismology, provides a single number to describe the amplitude distribution of the identified clicks within the signal with a lower *b*-value indicative of a larger spread of amplitude magnitudes (i.e., ratio of lower to higher amplitude clicks).

3.3.1.3 Results

The click locations for extension and flexion phases of exercises exhibited clear trends as shown in Figure 3.7(a) and (b), respectively. For extension, the most consistently-occurring major acoustic event is located towards full extension, and this matches the cadaver data,

which showed louder sounds for these joint angles ($\sim$10° – 20°). For flexion, the results are not as clear; the histogram for the click data showed a bimodal pattern with peaks at approximate flexion angles of 25° and 55°, while the cadaver data contained peaks in RMS power at $\sim$30° and $\sim$60°. Moreover, the click data exhibits less defined peaks compared to the cadaver result.

For *b*-value (Figure 3.8(a)), the main effects of sex (collapsed across leg dominance, p = 0.09) and leg dominance (collapsed across sex, p = 0.74) were not significant. However, the sex by leg dominance interaction was significant (p = 0.01). Pairwise comparisons revealed that dominant leg *b*-values were significantly lower ($p < 0.0001$) in females (1.14 ± 0.23) compared to males (1.44 ± 0.31), while non-dominant leg *b*-values were not different (male = 1.43 ± 0.25, female = 1.31 ± 0.37, p = 0.10). Furthermore, females had a lower *b*-value for the dominant compared to non-dominant leg (by 0.17 ± 0.35, p = 0.007), but men did not (-0.014 ± 0.24, p = 0.75).

Similarly, for the basketball player *b*-value analysis (Figure 3.8(b)), the main effects of sex (collapsed across leg dominance, p = 0.20) and leg dominance (collapsed across sex, p = 0.48) were not significant, though the sex by leg dominance interaction was significant (p = 0.02). Pairwise comparisons of *b*-values between men (1.34 ± 0.19) and women (1.15 ± 0.24) basketball players' dominant legs did not show a significant difference (p = 0.08), and the non-dominant leg *b*-values were not significant (men = 1.26 ± 0.22, women = 1.39 ± 0.37, p = 0.23) as well. Moreover, women's basketball players exhibited smaller *b*-values for the dominant leg compared to non-dominant leg (by 0.25 ± 0.40, p = 0.01), while men's basketball players were not significantly different (0.07 ± 0.16, p = 0.50).

3.3.1.4 Discussion

We found that consistent-click locations for collegiate athletes occur in probabilistic locations with these major acoustic events occurring towards the end of the exercise for extension or roughly at the first or second third of the flexion phase. The extension phase re-

sult strongly matched the results from a cadaver-based study [77], which attributed louder sounds during this period to compression of the menisci. This comparison is significant in that (1) these sounds can be captured using both air- and contact-based sensing modalities and (2) highly-controlled laboratory experiments which specified the speed of the exercise and limited interface noise by suturing the sensors to the skin matched recordings for which speed was not strictly controlled nor the sensor placement optimized for reducing interface noise (e.g., use of tape vs. medical-grade glue to adhere the sensors to the skin). While the flexion phase results did not show as strong a comparison with the cadaver data, importantly, the two results did not contradict one another.

Additionally, we observed differences in b-value between men and women healthy collegiate athletes. Most interesting, the b-value for the dominant leg in females was lower than the non-dominant leg as well as the dominant leg in males, and the dominant vs. non-dominant leg comparison in females result held true for women basketball players. The results of Jeong *et al.* and Whittingslow *et al.* suggest that a lower b-value is indicative of a more "unhealthy" knee (i.e., trending towards a more injured state) when comparing within-subject, within-knee measurements for, perhaps importantly, exclusively (or nearly so) male knees [77, 78]. However, it is unclear from these studies if a one-time, singular b-value measurement is sufficient to determine joint health—or injury risk—on its own. At this time, we speculate the lower dominant leg b-value exhibited in females—specifically those participating in sports involving repetitive jumping—may be, in part, attributed to a larger maximum knee valgus angle during drop vertical jump (DVJ) tasks in females' dominant knee, which was observed in high school basketball [81, 82] and soccer players [82]. Similarly, dominant knees exhibited greater valgus moments during cutting tasks [83]. However, one study has suggested that female collegiate vs. recreational athletes may show opposite side-to-side asymmetric knee kinematic trends though these results may be confounded by other factors, such as age, body mass index, sport, etc. [84]. Notably, models of valgus misalignments show increases in joint contact forces and overall larger and

more sustained forces during walking and stair climbing [85], and this larger valgus angle / loading has been associated with increased anterior cruciate ligament (ACL) strain (*in vitro*) [86] and patellofemoral pain as studied in female subjects [87] as well as a potential predictive measure for ACL injury [88]. Though *b*-value has not yet been explicitly studied during joint loading, other features of knee joint sounds—namely increased RMS power and heterogeneity—have been shown to change with increased loading [48, 89]. While we surmise that valgus angle and loading may contribute to the lower *b*-value females' dominant leg, other factors, such as those associated with the increased risk of ACL tears in females, may contribute to this difference, including neuromuscular deficits [90], namely "ligament dominance," "quadriceps dominance," "leg dominance," and "core dominance," hormone levels [91], anatomical differences (e.g., Q angle, femoral notch widths, etc.) [69, 92], and biomechanical variations [69].

Importantly, the *b*-value metric is just one feature of joint sounds, and as such, future analyses and studies should examine if other features of joint acoustics are similarly impacted by sex and / or leg dominance. Calculation of a joint health score, especially for decision-making criteria (e.g., return-to-play), should consider any impact of sex or leg dominance, and perhaps this joint health score could be used as a metric for determining the likelihood of injury susceptibility. Lastly, future studies should be adequately powered for sex differences, as results for males and females may not be generalizable when examining the magnitudes of singular value metrics of joint health (e.g., not within-subject or longitudinal comparisons).

3.3.2 Discriminating Healthy and Injured Subjects and Tracking Rehabilitation

This work [93] was largely completed by Dr. Sinan Hersek of the Inan Research Laboratory and is included—in brief—here, as it presents the results from the full study described in this chapter. This work and analysis developed a quantitative metric—graph community factor (GCF) score—for knee joint health derived from acoustical emissions, which not

only separates healthy and injured knees but also tracks improvements in knee health status following a successful rehabilitation protocol.

3.3.2.1 Subject Demographics

Results presented here were derived before the full healthy subject dataset was collected. Specifically, this dataset comprised of 33 healthy subjects (vs. 49 total) and nine injured subjects. These nine injured subjects had an acute, unilateral knee injury, and one measurement was taken from all nine subjects within seven days of the injury. The injuries included torn anterior cruciate ligament (six subjects), torn lateral meniscus (one subject), and sprained medial collateral ligament (two subjects). Seven of these subjects required corrective surgery, and thus a second measurement was taken four to six months following this surgery at which point the subjects could resume functional activities.

Subject demographics and physical characteristics are presented in Table 3.2. Subjects were similar in age, height, and weight between injured (N = 9) and non-injured groups (N = 33). A lower extremity functional scale questionnaire validated and utilized in clinical decision making (Binkley, *et al.* [94]) was completed at each laboratory visit. This self-reported score has a maximum value of 80 when no symptom limitations in daily function or activity are reported in the lower extremity. The questionnaire is made up of 20 questions related to the level of difficulty the subject has in performing various daily and sports activities (standing, sitting, running, squatting etc.). As expected, a significantly worse lower extremity functional score was reported by the injured subjects compared to the healthy subjects ($p < 0.01$ using a two-sample Kolmogorov-Smirnov test).

3.3.2.2 Graph Community Factor Calculation

An unsupervised graph mining algorithm was employed to visualize the heterogeneity of the high-dimensional acoustical emission data and then derive a quantitative metric capturing this heterogeneity—the GCF. Briefly, this method (1) extracts time and frequency

Table 3.2: Demographic Data for Study Participants (for Graph Community Factor Results)[a]

	Healthy	Injured
Number of Subjects	33	9
Number of Females (% of group)	7 (21%)	1 (11%)
Number of Males (% of group)	26 (79%)	8 (89%)
Age ($\mu \pm \sigma$, in years)	19.8 ± 0.9	20.8 ± 1.6
Height ($\mu \pm \sigma$, in cm)	184.0 ± 8.0	186.1 ± 7.9
Weight ($\mu \pm \sigma$, in kg)	94.6 ± 18.0	106.6 ± 22.3
Lower Extremity Functional Score	78.8 ± 2.5	$36.3 \pm 10.5^{*}$

* Indicates statistically significant difference ($p < 0.01$).
[a] Reproduced from [93].

domain features from multiple time windows of the recordings from both knees' audio signals, (2) constructs k-Nearest Neighbor graphs based on these features, and (3) calculates the GCF from these graphs. A detailed description of the GCF calculation is provided in [93]; however, a summary of the method is provided here.

First, the joint sound data is pre-processed, filtering the data to remove interface noise (bandwidth of 1 kHz to 15 kHz) and normalizing the signal to have zero mean and unity variance to account for distances between the microphone and skin. A total of 64 time and frequency domain features are extracted from sliding windows (50% overlap) of 200 ms (for a list of specific features, refer to [93]). Feature matrices from a single subject include data from the left and right knees from five flexion / extension cycles. This feature matrix is then used to create a kNN graph, which leverages weights assigned to each graph edge using dice similarity to incorporate the properties of each point's neighborhood rather than relying on Euclidean distance alone in attributing points to particular clusters or communities [95]. After the weighted graph is constructed, the potential communities within the graph are detected. The Infomap community detection algorithm (readily available online [96]) is used for this purpose [97]. This algorithm considers the amount of time spent in different portions of the graph, by a random walking process, to reveal different communities within the graph [97, 98]. Once the communities are detected, the GCF is calculated as the number of communities discovered.

It is expected that the data from both knees of a healthy subject would be more homogenously distributed within the features space than the data from a subject with a unilateral knee injury. However, modeling the distribution of the data matrix using models such as Gaussian or student's t-distribution [99] requires strong assumptions to be made about the shape of the data in the high-dimensional space (e.g., ellipsoid, convex). Furthermore, such models need parameters to be estimated about the underlying distribution of the data, which is difficult in high dimensions due to the curse of dimensionality [100, 101] (in high dimensional space where all data points appear to be sparse, it becomes increasingly difficult to understand the properties of the data). Kernel-density estimation-based clustering techniques suffer from the same problem due to the existence of parameters to be estimated, such as kernel bandwidth.

Rather than modeling the distribution of the data in the high-dimensional feature space, a kNN graph is used, which has been used in previous studies to model and cluster high dimensional data in bioinformatics [102, 103]. Here, the heterogeneity of the data distribution is quantified using the number of communities within the graph, which is expected to be higher for data that is more heterogeneously distributed.

Communities are detected within the data graph instead of finding clusters within the data using regular clustering algorithms such as k-means, Gaussian mixture models, or spectral clustering, as such algorithms take the number of clusters to be found as an input. Additionally, using kernel density estimate based clustering algorithms [104] to estimate the number of clusters in the data is not a feasible solution. Such techniques are time consuming for high-dimensional data, and the curse of dimensionality makes it difficult to robustly detect dense areas within the data distribution.

3.3.2.3 Graph Community Factor Results for Injury Classification

Figure 3.9(a, i-iii) provides visualized data (knee graphs) constructed for a representative healthy (Figure 3.9(a-i)) and a representative injured subject (Figure 3.8(a-ii), measured

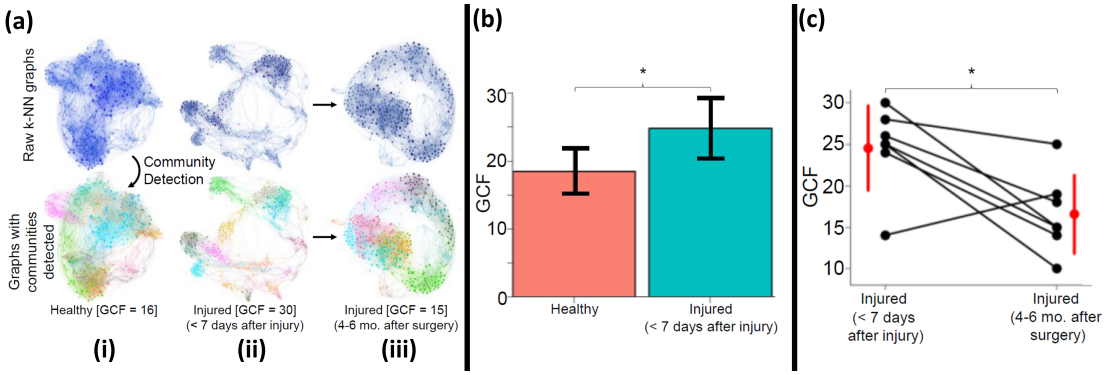

Figure 3.9: Healthy vs. injured knees and rehabilitation results. (a) The relationship between graph heterogeneity (quantified using the graph community factor, GCF) and acute unilateral knee injury. (a-i) The graph constructed using features extracted from the audio signals acquired from both knees of a healthy subject (top). The Infomap community detection algorithm discovered 16 communities (GCF = 16) in the graph, all shown in distinct colors on the graph in the bottom. (a-ii) The graph constructed using the data acquired from a subject with an acute unilateral knee injury, where 30 communities are detected. The heterogeneity of the features for the injured subject is visually and quantitatively greater than for the healthy subject. (a-iii) The graph constructed using the data acquired from an injured subject after corrective surgery, where the number of communities detected has decreased to 15, and the heterogeneity has decreased visually. (b) The GCF calculated for healthy subjects (N = 33, shown in pink) and subjects with an acute unilateral knee injury within seven days of the injury (N = 9, shown in cyan). The bars represent the mean of the GCF within the population and the error bars represent one standard deviation. The asterisk (*) represents a statistically significant difference (p = 0.01), where the p-value is calculated using a two sample Kolmogorov-Smirnov test. (c) The GCF metric for seven subjects with unilateral knee injury immediately after injury (within seven days) and 4 – 6 months after corrective surgery. The black data points connected with lines represent each subject's data. The red data points and error bars represent the mean and one standard deviation of the GCF for all the seven subjects, before and after surgery. The asterisk (*) represents statistical significance (p = 0.01) based on a two-sample Kolmogorov-Smirnov test. Adapted from [93].

within seven days of the injury; Figure 3.9(a-iii), measured again six months following reconstructive surgery for the same subject), respectively. As described in the previous section, each node in the graph represents the high dimensional vector of time and frequency domain features extracted from one windowed segment of the acoustical emission waveform. The different communities detected within these graphs are shown in different colors at the bottom. The number of communities detected within the healthy subject's data graph (Figure 3.9(a-i)) was 16 (GCF = 16); for the injured subject's graph (Figure

3.9(a-ii)), constructed from the recording taken within seven days of the injury, the GCF was 30. In addition, the GCF metric decreased to 15 for the same injured subject after corrective surgery and six months of recovery (Figure 3.8(a-iii)). The graph on the upper and lower left (healthy subject, Figure 3.9(a-i)) shows a set of densely clustered, homogeneous nodes, with many of the nodes falling close to one another in the high dimensional space. The graph on the upper and lower middle (Figure 3.9(a-ii), injured subject within seven days of the injury), on the other hand, shows a more heterogeneous set of nodes, geometrically spread out in space rather than clustering together densely. Finally, the graph on the upper and lower right (Figure 3.9(a-iii), injured subject six months after surgery and recovery) demonstrates that the same subject's nodes become much more homogeneous following recovery, resembling closely those observed in the healthy subject's graph.

Figure 3.9(b) compares the GCF metric of nine subjects with acute, unilateral knee injuries to that of 33 healthy subjects. While the GCF is derived from each subject's data independently, the metric can be compared among subjects in an absolute manner, with a lower GCF indicating more homogeneous acoustical emission signatures and a higher GCF more heterogeneous emissions. In the bar-plots shown in Figure 3.9(b), the height of the bar represents the mean value of the GCF metric within the population (injured or healthy) while the error bars represent one standard deviation. The GCF metric was higher for subjects with an acute, unilateral knee injury than the healthy subjects, and the difference between the groups was statistically significant ($p = 0.01$). A two-sample Kolmogorov-Smirnov test was performed to evaluate the statistical significance.

Figure 3.9(c) presents the individual change in the GCF metric during injury recovery for seven subjects with unilateral knee injuries that were treated with corrective surgery. This figure depicts that the GCF metric decreased for six out of seven of these injured subjects. In the exceptional case, the GCF metric showed an ascending pattern. The subject with the ascending pattern had a very low GCF value for the first recording, which is likely attributed to a noisy measurement. The overall results for all subjects were found

to be significantly lower following surgery and recovery using a two-sample Kolmogorov-Smirnov test (p = 0.01).

3.3.2.4 Conclusions using the Graph Community Factor

The changes in GCF were consistent with improved knee health from the athletic trainer's subjective evaluation as well as the improvement in the lower extremity functional scores. The lower extremity functional score for the injured subjects increased significantly ($p < 0.01$) from 36.1 ± 12.1 in the first measurement (within seven days of the injury) to 63.7 ± 11.0 in the second measurement (four to six months after surgery). Note that the functional score is derived from subject responses to survey questions regarding their ability to perform activities and, accordingly, is qualitative and can be subjective. The GCF metric provided by the joint sound recordings can augment this functional score and medical professional's evaluation by providing quantitative and objective data regarding joint health status. Moreover, if such data is obtained longitudinally throughout the rehabilitation, therapies can be titrated based on the changing joint health status of the patient. This paper shows the initial efficacy and potential of joint sounds, and associated GCF, as a metric of joint health; further studies with larger sample studies can allow for comparisons between GCF and functional scores, as well as investigate the possible combination of both for a more holistic assessment of joint health.

Knee joint acoustical emissions are complex signals produced by the underlying structures of the knee joint [26]. As the knee is flexed / extended, the femur and tibia move and the cartilage surfaces of these structures glide over each other as well as the patella. This gliding produces vibrations that contribute to knee joint acoustical emissions [19]. Furthermore, these motions cause changes of pressure in the synovial fluid within the joint and create vibrations in the surrounding muscles, which also contribute to the acoustical emissions [105]. Therefore, these acoustical emissions are generated by multiple complex processes within the knee joint and contain information about the underlying structures that

generate them. In this work, we study the acoustical emissions generated by both knees by creating a kNN graph using these signals and conclude that the generated graph has more heterogeneity (defined as a higher GCF) for injured subjects. One of the reasons for the increased GCF in injured subjects is greater differences between the acoustic emissions produced by the knees (injured versus healthy), possibly due to the changes in the structure of the injured knee. Other possible reasons of increased GCF in injured subjects are more variability within the acoustical emissions produced by either one of the knees due to less structural stability in the joint during particular movements.

3.4 Conclusion and Future Work

In this chapter, we examined miniature microphones for wearable joint health monitoring. We considered electret, MEMS, and piezoelectric film microphones. Sensing joint sounds via an air-based modality showed similar signatures as the contact-based microphone with high-amplitude, short-duration, and broad bandwidth instances sensed by both types of microphones. We demonstrated these clicks can be robustly measured and appear at similar flexion angles for repeated exercises. Further analyses examined joint sound characteristics in healthy subjects with preliminary findings showing differences between males and females and as well as differences between legs for females. Most importantly, the joint acoustic emissions sensed by the electret microphones were able to discriminate between healthy and injured knees and track improvements in knee health following rehabilitation. From this specific set of sensors, we recommend the air-based microphones, as the SNIR for the piezoelectric film was low; packaging techniques for film-based sensors must be carefully considered to minimize noise. Alternatively, other contact microphones, such as high-bandwidth accelerometers, may be used. For all microphones, future work will investigate techniques for integrating these microphones within a wearable brace, ensuring satisfactory signal acquisition while minimizing noise, guaranteeing sensor-to-skin interfaces or distances for contact- and air-based microphones, respectively.

3.5 Acknowledgements

We extend our thanks to P. Wolkoff (Georgia Tech Athletic Training) for insightful discussions and support during human subject testing.

CHAPTER 4
A WEARABLE, MULTIMODAL SENSING SYSTEM TO MONITOR KNEE JOINT HEALTH

4.1 Introduction

Ultimately, joint acoustics, edema, and kinematics aim to capture some underlying physiological state or anatomical change within the joint itself. While these measures have shown promise for assessing the health of the knee, nearly all the work using these sensors has been conducted in-lab / in-clinic using benchtop data acquisition units, which are not conducive for realistic implementation of such systems. An embedded systems-based approach presents an attractive next step, as embedded systems can be used for rapid prototyping and deployment in early phases of research due to their availability, low cost, and extended battery life. With respect to IMUs and EBI systems for wearable applications, embedded-based approaches have been achieved [106–110], likely made readily feasible by operating at conveniently low sampling rates ($\leq$ 2 kHz). However, acquiring joint sounds, which have been captured in even the ultrasonic bandwidth [21] and may use multiple microphones arrayed around the knee [48, 111], pose greater sampling loads for embedded systems. Further, given the still-exploratory nature of joint health research, joint sounds cannot yet be compressed (e.g., to minimize data storage or transmission requirements) using lossy methods without compromising the potential feature space, though recent work by Athavale *et al.* suggests an encoding scheme of these signals is possible [112], and compression ratios of lossless methods need to be balanced with energy consumption, memory accesses, and overall hardware constraints, such as the available RAM [113]. For biomedical research, there has been minimal work that acquires audio in wearable-type settings; studies have often relied on the use of commercially available audio recorders or smart

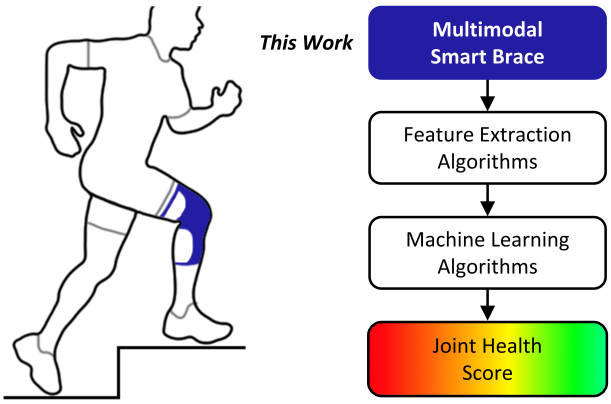

Figure 4.1: Overview of the wearable, multimodal sensor brace for knee joint health assessment. Using this smart brace, sensor data can be extracted and used to provide physiologically significant information such as swelling, activity level, and joint angle. Ultimately, machine learning algorithms can be employed to provide a joint health score for use in various applications, including during rehabilitation after an acute injury and management of joint diseases, such as arthritis.

phones [29, 114], which cannot be readily integrated into a custom system, particularly one designed to be wearable. Conversely, custom embedded systems have been deployed in other fields, such as environmental monitoring and underwater acoustics, though these systems have leveraged larger batteries, higher power consumption, and greater footprint overall [30, 31, 115, 116] and / or are commonly limited to single-channel audio [117, 118]. As such, new techniques for recording data from multiple high- and low- bandwidth sensors must be explored to achieve wearable technologies. Further, user-centric mechanical design must be considered for incorporating sensors and systems to encourage subject compliance, and other "smart" features may improve the user experience.

4.2 A Wearable Multimodal Smart Brace

4.2.1 Introduction

In this work, we present a multimodal "smart" knee brace for joint health assessment, capturing joint sounds, EBI, inertial measures, and skin temperature. This is the first-ever wearable system, to the best of our knowledge, that combines monitoring of both knee

physiology (i.e., swelling and kinematics) and structure (i.e., acoustics). In contrast to our group's prior work [18, 111], which involved benchtop hardware tethered to a laptop for data collection, this section presents the hardware and firmware implementation of two fully-embedded sub-systems and validation of their function. Importantly, we consider the robust sampling and saving of data, ensuring that no data packets are dropped. These embedded hardware systems were packaged in a flexible, 3D-printed "brace," providing an initial mechanical prototype for a wearable system. Lastly, we present proof-of-concept recordings of joint health data from a healthy subject, demonstrating the feasibility of the brace to be used for in-clinic or at-home studies. Ultimately, we envision the use of this smart brace to measure joint health data, which can then be processed with feature extraction and machine learning algorithms to provide a comprehensive and quantitative joint health score, equipping clinicians and patients with actionable data that may be used during rehabilitation following an acute injury or when titrating medication for disease management (Figure 4.1).

4.2.2 Embedded System Design

The system is comprised of two subsystems, currently located on two separate printed circuit boards (PCBs). The first system's purpose is to sample high-throughput audio data triggered by a switch, while the second system continuously samples lower-rate data from multiple sensors, specifically EBI, inertial, and temperature data. In this paper, these two boards are referred to as the audio and main board, respectively. A summary of the system and sensors is provided in Figure 4.2.

This two-microcontroller design was used to ensure that packets are not dropped. Given the high data rate required by the microphones, a dedicated microcontroller is required to obtain data from an analog-to-digital converter (ADC) and write it to a microSD card as quickly as possible. Even with this sole purpose, the microcontroller fails to strictly meet SD card timing specifications, which is described in Section 4.2.2.1.3. Adding additional

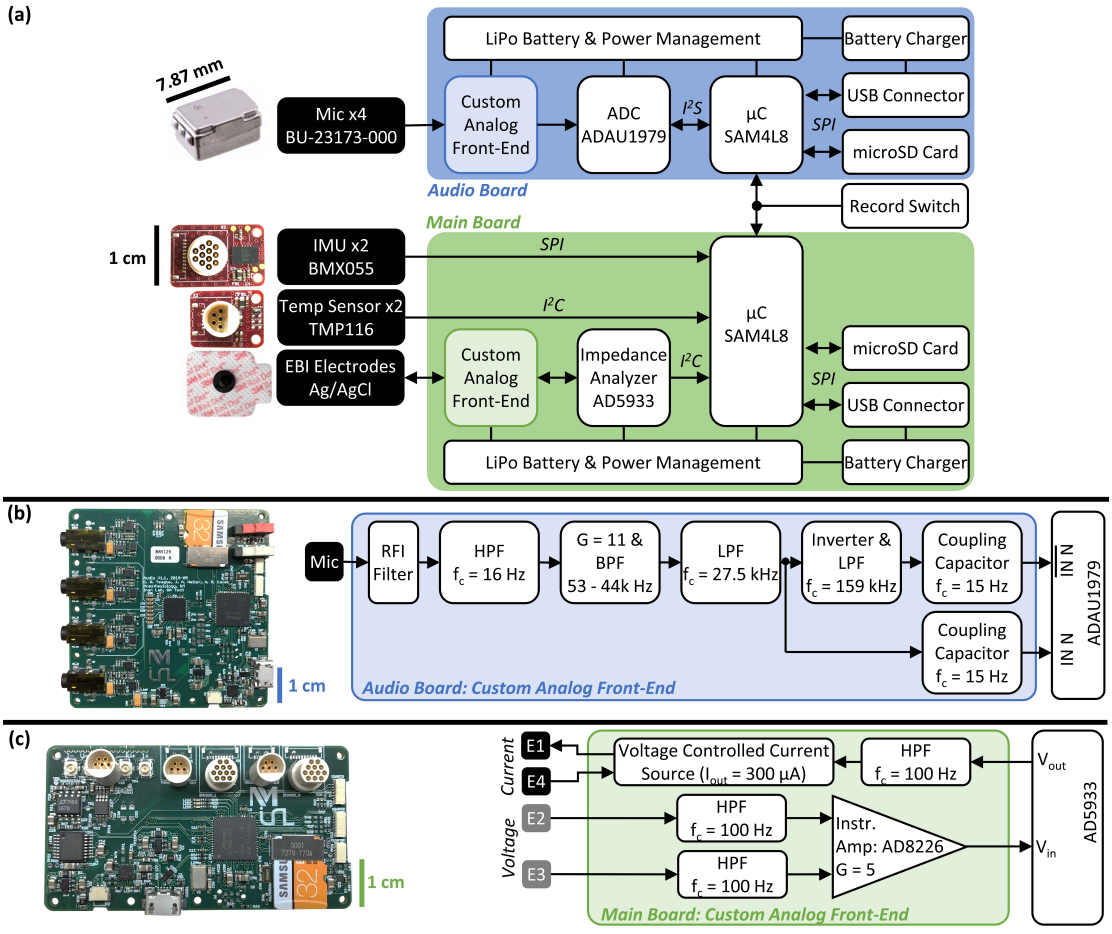

Figure 4.2: Smart brace system and block diagram. (a) Overall system block diagram, which consists of two circuit boards synchronized via an interrupt pin controlled by a slide switch, "Record Switch." The main board consists of a microcontroller (μC), which continuously samples data from (1) two inertial measurement units with three-axis accelerometer and gyroscope data, (2) two temperature sensors, and (3) electrical bioimpedance sensing hardware connected to the body via four Ag/AgCl gel electrodes. The sampled data are saved onto a microSD card. These data can later be read by a computer via USB, interfaced by an on-board microUSB connector. The audio board consists of a custom analog front-end, which applies gain and filters to four contact microphones. These four microphones are sampled by an ADC that transfers data to the microcontroller to save onto a microSD card. Both circuits have their own batteries, battery chargers, and power management systems to provide digital and analog power to different components. (b) Photo of the audio printed circuit board and block diagram of the custom analog front-end for conditioning the microphone signals. (c) Photo of the main circuit board and block diagram (reproduced from [119]) of the electrical bioimpedance circuit.

clock cycles to sample other sensors would further exacerbate this issue. Consequently, another microcontroller needed to sample from all other sensors. These subsystems were placed on separate boards so that the main board can be independently used for EBI measurement.

Importantly, these two boards are synchronized to provide important contextual information for joint sounds. For example, for joint sounds, IMUs provide joint angle, speed of the exercise, and exercise type, while for EBI, IMUs determine the orientation of the limb and can be used to gate processing of data compromised by motion artifacts. Similarly, the temperature sensors provide skin temperature, which can be used for interpreting changes in signals (e.g., edema) that are a result of environmental changes and are not due to underlying physiological changes. Accordingly, the system is aware of the context surrounding the physiological and structural health measurements, which should improve the robustness and relevance of the data obtained for assessing knee health.

Both boards use a SAM4L8 (Microchip Technology Inc., Chandler, AZ) microcontroller. It was selected for its low power modes, extensive digital communication modules, and inclusion of floating-point arithmetic, which future designs could leverage for on-board processing. Furthermore, the SAM4L is a 32-bit microcontroller, which is an important feature for efficiently reading audio data and minimizing counter roll-over of the 32.768 kHz crystal, which was clocked down to 4096 Hz. When it is used to record sample times, absolute timing of samples can be synchronized between the boards simply with an interrupt pin because overflow occurs at a time (12 days) that exceeds the battery life.

The embedded design was completed with J. Alex Heller of the Etemadi Research Group out of Northwestern University.

4.2.2.1 Audio Printed Circuit Board Design

A photo and block diagram of the audio PCB are shown in Figure 4.2(a) and (b). This system consists of four contact microphones, a custom analog front-end, a four-channel

analog-to-digital converter (ADC), a microcontroller (MCU), and a microSD card.

4.2.2.1.1 Microphones and Analog Front-End

The system permits four microphone channels. We selected miniature contact microphones (BU-23173-000, Knowles Electronics LLC., USA) for their low noise, small size, and wide bandwidth. Moreover, our previous work has shown their efficacy for evaluation of mechanical stress on the knee [48]. A contact microphone is essentially a wide bandwidth accelerometer that detects the vibrations of the skin in response to underlying acoustic emissions from the joint.

Each single-ended microphone signal was passed through a custom analog front-end (AFE). A block diagram of the AFE is shown in Figure 4.2(b). Following a radio frequency interference filter and a passive high pass filter (f_c = 16 Hz), the signal was amplified (gain of 11) and filtered (53 Hz – 44 kHz) using an audio operational amplifier (op-amp) (LTC6240, Analog Devices, Inc., Norwood, MA), which was selected for its high gain bandwidth product and low noise. Given the prevalence of the use of 100 Hz as a sample rate for IMU-based knee joint kinematics in the literature, a high-pass filter cutoff of 53 Hz (i.e., 50 Hz) was selected to reduce motion artifacts from saturating the amplifier. The signal was then low-pass filtered at 27.6 kHz via a second-order Sallen-Key to reduce aliasing during sampling. Though higher-order filters are generally preferred to provide sharp roll-off to prevent aliasing, the design leveraged the sigma-delta architecture of the ADC; sigma-delta ADCs oversample the inputs at a much higher rate than the sampling frequency, increasing the Nyquist frequency and allowing for a more gradual roll-off analog filters. Limiting the anti-aliasing filter to one op-amp and four passive components helped minimize power consumption and PCB footprint. The next stage consisted of an inverter—with low pass filtering (f_c = 159 kHz)—to create a differential signal. For this stage, highly matched passive components were employed to minimize error between the inverting and non-inverting inputs. Operating in differential mode allowed for a higher

effective number of bits given these components do not add more noise than bits gained, and this was experimentally verified. Finally, the differential signals were AC coupled; this capacitor combined with a resistor internal to the ADC to form a final high pass filter (f_c = 15 Hz). The AFE regulator's shutdown pin allowed this circuitry to be dynamically turned on and off by the MCU.

4.2.2.1.2 Analog-to-Digital Converter

The differential signals were sampled by a standalone ADC. We selected the ADAU1979 (Analog Devices, Norwood, MA) for its for its high bit depth (16 or 24 bits), low noise (-95 dB total harmonic distortion), and four-channel, simultaneous-sampling capability. Our prior studies were completed using 16-bit data acquisition systems—with both higher possible input voltage ranges and single-ended configurations—and demonstrated differences between different populations of subjects (healthy vs. injured) as well as different mechanical loading conditions within a given subject [48, 93], suggesting the 16-bit configuration should suffice for extracting physiologically relevant features using this new hardware.

The SAM4L8 only has one inter-IC sound (I^2S) channel and operates using a standard two-channel, stereo mode (i.e., a left and right channel on a single data bus). I^2S consists of three communication lines: (1) SDATA, which gives the serial sound data; (2) BCLK, which provides timing for each individual bit of SDATA; and (3) LRCLK, which specifies the left or right channel of SDATA. This conflicts with the default configuration of the ADC, which splits the four audio channels onto two different data busses when using I^2S. To transfer all four channels on one data bus, the time-division multiplexing (TDM) communication protocol—with respect to the ADC—must be used. TDM is an extended I^2S protocol allowing for multiple channels (slots) to be fit within one left / right channel, allowing for all four signals to be transmitted over a single SDATA bus. We use TDM4 to fit two signals within one channel. Using the 16-bit ADC data width, two signals may fit within one 32-bit LRCLK window. Accordingly, the MCU is programmed to expect 32-bit

LRCLK channels, and the ADC fills each left / right channel with two slots of 16-bit data. Post-processing later splits the data into distinct microphone signals.

Facilitating 24-bit ADC data resolution is more involved because, though 24-bit modes are available on both chips, clock division constraints on the MCU prevent their direct use for this application. Accordingly, a 32-bit SDATA width—the MCU's maximum received data width—is required, fitting the 24-bit data with extra, unused bits. Using this maximum width, the MCU-driven LRCLK provides two 32-bit I^2S / TDM slots, which will not fit all four channels. To permit two additional channels, we stretch the LRCLK by feeding this signal back into the MCU, divide the frequency in half, and feed it out to the ADC. This stretches each LRCLK to 64 bits, meaning the ADC now has enough room in each LRCLK channel to fit two 32-bit TDM slots. With this, the ADC now sees a sample frequency at half the desired rate (since LRCLK is directly the sample frequency), so this is mitigated by increasing the initial output sample rate from the MCU by a factor of two. We also configure BCLK to follow the same in-out-in path (without division) such that BCLK experiences the same path-induced phase delay as LRCLK, allowing for aligned data lines and thus correct bit placement. Of note, the data received is shifted by one bit, but since it is shifted in correct direction and given the extra space in the register with respect to the data width (i.e., 32-bit register vs. 24-bit data), the correct ADC data is resolved in post-processing.

For this work, we employ the 16-bit configuration to allow for four channels of audio. However, future work may utilize the 24-bit mode using fewer microphones to minimize the data-writing constraints to the microSD card.

4.2.2.1.3 Saving Data to a microSD Card

For saving the audio data stream, we employ the MCU's direct memory access (DMA). The DMA allows the I^2S module to directly save data to memory without processing intervention. The data are saved using a circular buffer with the DMA working with one half of

the buffer at a time. We leverage the MCU's reload buffer feature (i.e., a pointer to the next location to write data when the buffer is full), which helps prevent dropping packets since the DMA always has an address at which to write data. Once half a buffer is full, the MCU records the time as read from a 32.768 kHz crystal (clocked at 4096 Hz). It then saves the data to the microSD card. We write 22 016 bytes (43 512-byte sectors) every 58.7 ms. The SD card specification indicates a maximum write time of 250 ms [120]. However, because the data throughput is so high and RAM limited, we do not meet this constraint. Because we record the time when a buffer is full, we can determine in post-processing if samples are dropped due to slow SD card writes or quality of the card.

A simple file system was implemented on the microSD card with FAT16 compatibility [121]. Each file is defined by its starting address on the microSD card and its length (i.e., an offset from this starting address). Each half buffer—a multiple of 512-byte blocks for write-efficiency—is written as raw binary data to the SD card to be interpreted by the PC.

4.2.2.2 Main Board Printed Circuit Board Design

A photo and block diagram of the main PCB is shown in Figure 4.2(a) and (c). This system continuously samples from the EBI system, IMUs, and temperature sensors.

4.2.2.2.1 Main Board Sensors

The BMX055 (Bosch Sensortec GmbH, Kusterdingen, Germany) is a three-axis accelerometer, gyroscope, and magnetometer. Though the magnetometer is not used in this work, future iterations of the system may choose to sample from this sensor to provide complete orientation estimates [43]. This sensor was chosen for its low-noise sensors and digital output interface, SPI. Though the current consumption is higher than other IMUs currently available, we selected it for this first iteration as an initial proof-of-concept.

To measure temperature, we selected the TMP116 (Texas Instruments Inc., Dallas, TX) for its high bit-depth and accuracy, on-board averaging, low current consumption, digital

output (I^2C), and ability to trigger multi-sensor synchronized readings.

The EBI system is based off our group's previous work [119]. For this work, we use the AFE and calibration scheme developed by Mabrouk *et al.* on this new board [119]; note that the firmware—particularly how EBI is sampled with respect to other sensors as well as the audio board—is specific to this work. Briefly, the EBI system consists of an impedance analyzer integrated circuit (IC) (AD5933, Analog Devices, Inc., Norwood, MA) connected to a custom AFE to interface the body. Typically, the AD5933 provides an excitation voltage and receives a current measurement as part of a two-electrode configuration. However, the two-electrode configuration includes the electrode-skin impedance as part of the measurement, lowering the dynamic range, accuracy, and resolution. Moreover, this configuration does not strictly limit current as required by safety specifications (IEC 60601-1-11) [122].

To mitigate these issues, a four-electrode configuration was used. The outer electrodes (E1 and E4 in Figure 2(c)) source current through the tissue, while a high impedance instrumentation amplifier (IA) (AD8226, Analog Devices, Inc., Norwood, MA) connected by the inner electrodes (E2 and E3) measures the voltage, thus neglecting the skin-electrode impedance. The injected current is sourced via a voltage-controlled current source, delivering 280 μA_{rms} (0A DC) to the body, complying with safety requirements. A block diagram of the AFE is provided in Figure 2(c). EBI measurements are performed in sweeps consisting of 256 equidistant-frequencies at 371 Hz ranging from 5 kHz – 99.605 kHz. For each frequency, a 16-bit real and imaginary impedance component is recorded.

4.2.2.2.2 Sampling Scheme for the Main Board

Data from the sensors are continuously sampled. The sampling scheme for this system is similar to that described in [121]; lower-power sensors—when new samples are ready—drive wake-up periods for the MCU, consuming less power since the MCU (1) is only active when sampling or saving data and (2) does not waste unnecessary cycles polling sensors to determine if data are ready. As such, the MCU is in a low-power mode for most

of the time and only wakes up to an active state when it receives a data-ready interrupt.

4.2.2.3 Computer Data Extraction Software and Time Syncing

Data saved on the microSD cards must be extracted at some point for analysis. A custom program was developed in C# for transferring data from the microSD card to the computer directly, alleviating the need for a user or study coordinator to interact with the microSD cards or hardware directly. When the PCBs are connected to the computer via a microUSB cable, the device is recognized by the computer as a USB device. Opening the custom program lists connected devices and their respective files, cataloging each file size and creation date / time. A single mouse click automatically downloads all the files from the device, saving them to a folder on the computer. Lastly, the program transfers date / time information to the device. This time synchronization allows for precise timekeeping, simplifies synchronization of multiple devices, and permits timestamp-based file naming according to when a recording was started.

The computer application was developed by Florencia Garcia-Vicente and J. Alex Heller of the Etemadi Research Group out of Northwestern University.

4.2.3 An Initial Brace Proof-of-Concept

4.2.3.1 Brace Design

To demonstrate the system's translation towards a feasible wearable device, the embedded system was integrated into a wearable "brace" as shown in Figure 4.3. The brace is comprised of three major components: the circuit box and two sensor housings located proximal and distal to the patella. This work was completed with Brandi N. Nevius of the Inan Research Laboratory.

The circuit box, 3D-printed using a polylactic acid (PLA) material, contains the main and audio PCBs, two batteries (LP-523334 3.7 V 500 mAh with PCM, Shenzhen PKCELL Battery Co., Ltd, Guangdong Sheng, China), and switches for initiating and stop-

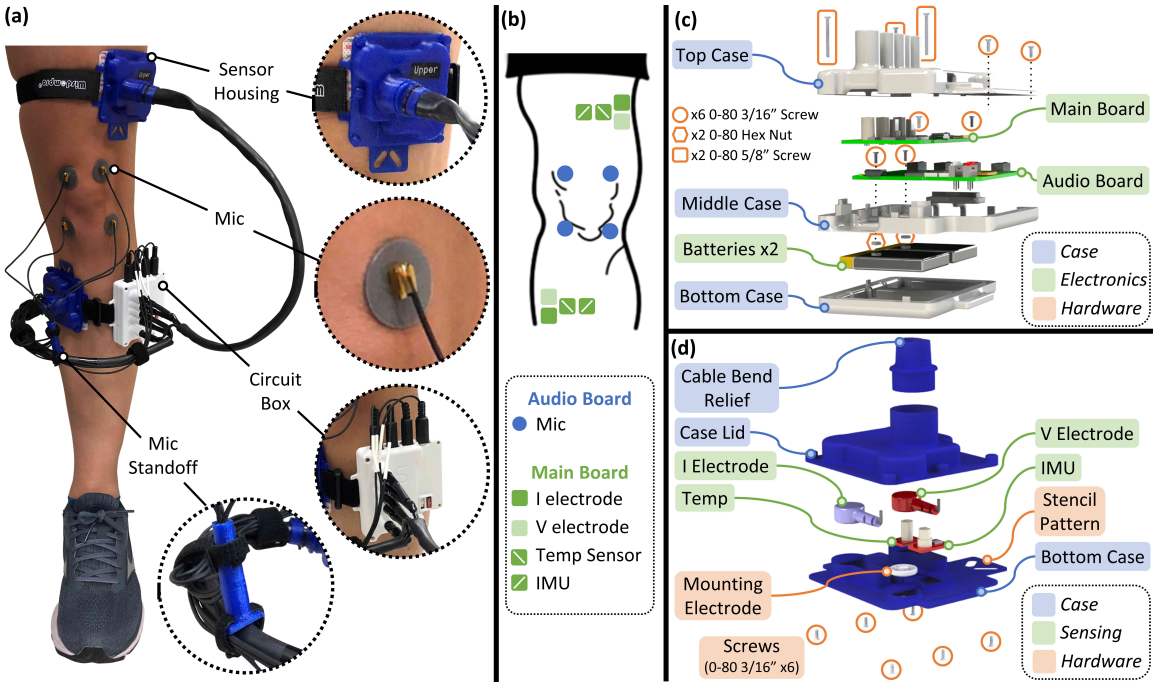

Figure 4.3: Initial brace prototype. (a) The brace worn on a subject's left knee. There are three major system components: the circuit box and two sensor housing units. The sensor housings and circuit boxes are attached to the leg via Velcro straps, and the sensor housings are further adhered using two electrical bioimpedance (EBI) electrodes and a third, non-electrically connected electrode. Lastly, microphones are mounted both proximal and distal to the patella using double-sided tape stickers. A "microphone (mic) standoff" is used to route the microphone cables away from the leg to prevent noise caused by inadvertent pulling and / or tapping of the cables on the skin. (b) Approximate locations of the various sensors (for a left knee) as sampled by each board. (c) An exploded view of the assembled circuit box, which houses both PCBs and batteries. (d) An exploded view of one of the sensor housings, which contains two EBI electrodes (one for current (I) and one for voltage (V)), an electrode used for mounting (not electrically connected), an inertial measurement unit (IMU), and a temperature sensor.

ping recordings. The circuit box itself is 7.5 $\times$ 7.7 $\times$ 3.9 cm. An exploded view of the circuit box assembly is shown in Figure 4.3(c).

The sensor housings (Figure 4.3(d)) serve as enclosures for the IMU and temperature sensors and include two electrode snaps for the EBI measurement (I and V electrodes) along with one additional snap that provides mounting support and is not electrically connected. The sensor housings are 3D-printed using a thermoplastic polyurethane material (NinjaFlex, NinjaTek, Manheim, PA). Its flexible nature serves multiple purposes; it allows

the brace to easily conform to different leg shapes and sizes and to provide some mechanical compliance as the subject moves. For reference, all blue components shown in Figure 4.3 are printed using this material. The electrode snaps are exposed on the subject-facing side to accommodate standard gel electrodes. Moreover, a slot in this inner surface exposes the temperature sensor, allowing for skin temperature measurements. The temperature sensor PCBs are coated with an aerosolized rubber (Plasti Dip, Plasti Dip International, Blaine, Minnesota) to protect the subject's skin from directly interfacing active and exposed circuit components while also providing the board protection from moisture, such as a subject's sweat.

The sensors and electrodes are connected to the circuit box via custom cables. Each cable—one to the IMU, temperature sensor, and both electrodes—are bundled into one larger cable assembly using silicone heat shrink. This method consolidates the four cables into one assembly while maintaining flexibility and permits sanitation.

4.2.3.2 Affixing the Brace

An important aspect of deploying a brace, particularly for at-home studies where ease-of-use for the subject is paramount, is consistent placement of sensing elements to (1) ensure the sensors acquire the desired data at specified anatomical locations and (2) facilitate valid longitudinal data comparisons. These considerations are essential for both joint sounds and EBI measurements; for joint acoustics, the positioning of the microphones with respect to the joint may influence the type of sounds measured, while EBI electrode spacing must be maintained to capture the same segment of the limb and thus the same gross tissue volume.

To enable correct and consistent placement of the brace on any given subject, a "stencil" approach was developed as illustrated in Figure 4.4. The stencil is a flexible, 3D-printed piece that provides areas to mark (with a marker) the subject's skin with the appropriate mounting locations. The stencil is configured with a curvature that fits against the distal or proximal edge of the patella, serving as an anatomical site for consistent sensor placement.

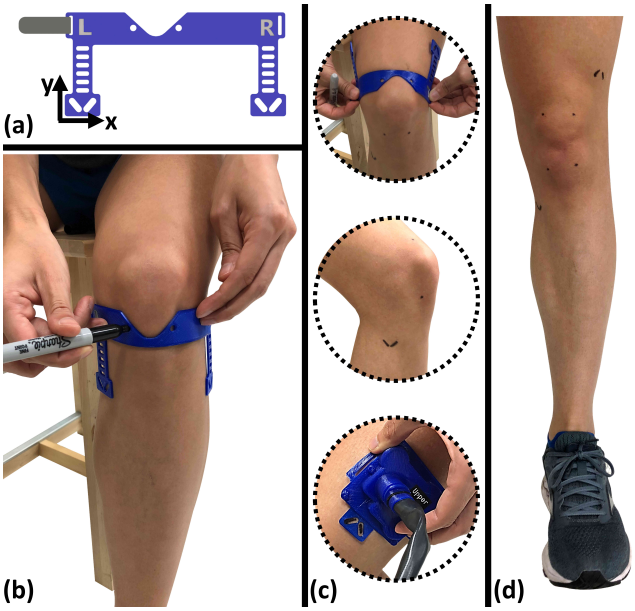

Figure 4.4: The stencil mechanism for mounting the microphones and sensor housings. (a) A rendering of the stencil shape. The curvature is used to fit the proximal or distal edge of the patella, providing a consistent anatomical reference. The round holes are used for marking the microphone locations, while the angled slots are used for locating the position of the thigh strap. By angling the slots, both x- and y- orientation constraints are achieved. (b) Aligning the stencil to the distal edge of the patella. In this position, the distal microphone locations are marked (as shown) as well as the pattern for mounting the distal sensor housing. (c) Positioning the stencil proximally for the thigh markings (top), example of the stencil markings as shown from the medial side (middle), and aligning the proximal sensor housing with the angled-slot stencil marking (bottom). (d) The final stencil markings for the microphones and sensor housings.

Notably, multiple sized stencils—or even stencils with varying patella curvature—are required to accommodate subjects of different height and weight. The stencil contains slanted slots (angled at 45°) at a fixed distance from the patella for positioning the sensor housings. The sensor housings contain these same slots such that the housing can be aligned (Figure 4.4(c)) and subsequently affixed to the skin, leveraging the EBI and mounting electrodes for adhesion and is further assisted by a Velcro strap. The angled nature of the slots constrains the placement of the sensor housing with respect to the sagittal and coronal planes, which are denoted as the x- and y- orientations in Figure 4.4(a). Additionally, round holes in the stencil note microphone locations at the lateral and medial sides of the patella and quadriceps tendons when the stencil is positioned distally or proximally, respectively, and

the microphones are then attached to the skin using double-sided adhesive pads (Lavalier Adhesive Stickies, Rycote, Rycote Microphone Windshields Ltd, Gloucestershire, United Kingdom).

However, correct placement of the microphones is not the only consideration; given they interface the audio board via long, free-hanging cables, the microphones can be susceptible to noise. These cables may introduce noise into the joint sound measurement by hitting other cables, tapping on the skin, and / or pulling on the microphone during articulation. To help prevent such instances, a "microphone standoff" (Figure 4.3(a)) is used to route the cables away from the leg, provide sufficient slack throughout the entire range of motion, and consolidate the cables such that they do not touch parts of the brace and / or other cables. In this way, the mic standoff emulates in-lab setups where cable management can be highly controlled.

4.2.3.3 Proof-of-Concept Recordings on Human Subjects

Institutional Review Board (IRB) approval was obtained from Northwestern University, the Georgia Institute of Technology, and the Navy's Human Research Protection Office (HRPO) to evaluate the device on human subjects. As a proof of concept, we measured signals from a single healthy subject (male, age: 33 years, height: 198 cm, weight: 79 kg) performing protocols established in previous studies [18]; specifically, for the joint sound measurement, the subject completed 10 cycles of unloaded, seated flexion / extension exercises, while the EBI measurement was conducted with the subject in a relaxed, seated position with his legs fully extended and supported (Figure 4.6(b) inset) for 10 sweeps. Given that prior work has already considered the use of these signals as quantitative physiological markers of joint health across multiple populations [18], and as the focus of this work is to outline the hardware for sampling across multiple sensors in a wearable form factor, we chose to present the results from a single, representative subject as a means to benchmark the feasibility of collecting robust data in a typical use case.

Table 4.1: Audio Board System Specifications

Parameter	Value
Power Consumption – Data Collection[a, b]	∼45.9 mA
Power Consumption – Sleep	∼330 µA
Sample Rate	46.875 kHz
Size	5.5 cm × 5.5 cm
Battery Life (using 500 mAh battery)[b]	$>$ 7 h
Frequency Response[c]	62.17 Hz – 22.84 kHz
Gain	20.75 dB
Data Storage Capacity	Card dependent

[a] Recorded with floating inputs.
[b] Dependent on SD card, number of recordings, and microphone inputs.
[c] Measured response.

For the purpose of this paper, processing was limited to enabling visualization of the signals of interest. Joint sounds from the four microphones were bandpass filtered (1 kHz – 10 kHz) and plotted against joint flexion angle, which was computed according to the algorithm presented by McGrath *et al.* [45]. The raw EBI data was converted to actual impedance values according to the calibration scheme by Mabrouk *et al.* [119]. Ensemble averaging—or sample-by-sample averaging across multiple datasets—was applied across the sweeps to provide a mean impedance sweep curve.

4.2.4 Design and Proof-of-Concept Results and Discussion

4.2.4.1 System Characterization

Tables 4.1 and 4.2 provide a summary of the audio and main board technical specifications, respectively. Note the current consumptions reported were measured using an Agilent Digital Multimeter (34410A, Keysight Technologies, Santa Rosa, CA) in series with each board's battery and streamed to a computer (via an Agilent 82357B USB/GPIB Interface High-Speed USB 2.0 cable, Keysight Technologies, Santa Rosa, CA).

For the audio board, a minimum 7-hour battery life is achieved with a 500 mAh battery. When waiting to record, the analog circuitry and ADC are powered down, while the MCU

Table 4.2: Main Board System Specifications

Parameter	Value
Power Consumption – Average[a, b]	$\sim$14.3 mA
Battery Life (using 500 mAh battery)[a, b]	$>$ 33 h
Size	3.5 cm $\times$ 6.5 cm
Electrical Bioimpedance	
Sample Rate	1 sweep/46.17 s (21.7 mHz)
Frequency Range	5 kHz – 99.605 kHz
Frequency Resolution	371 Hz
Dynamic Range[c]	200 Ω
I_{body}[c]	280 μA_{rms}
Resolution[c]	0.2 Ω
Mean Error in R[c]	0.4 Ω
Mean Error in X[c]	0.54 Ω
Accelerometer (3-axis)	
Bandwidth[d]	125 Hz, 62.5 Hz
Noise Density[d]	150 $\mu g/\sqrt{Hz}$
Sample Rate[d, e]	250 Hz [255.8 Hz], 100 Hz [107.5 Hz]
Gyroscope (3-axis)	
Bandwidth	32 Hz
Noise	0.1°/s (rms, BW=47 Hz, @0.014°/s/$\sqrt{Hz}$)
Sample Rate[d]	100 Hz [100 Hz]
Temperature Sensor	
Averaging	8 samples
Bandwidth	7.8125°($\pm$1 LSB)
Bandwidth	1 Hz [0.996 Hz]
Data Storage Capacity	Card dependent

[a] Dependent on impedance load.
[b] Dependent on SD card.
[c] Reproduced from [119].
[d] Two values because one sensor is oversampled.
[e] Programmed frequency [measured frequency].

is in a low-power mode, averaging a $\sim$330 µA wait current. When recording, the average current (with floating inputs) is $\sim$45.9 mA with average peak currents when writing to the microSD card at $\sim$70 mA. Lastly, the measured frequency response through the ADC is 62.17 Hz –22.84 kHz with a low-pass roll-off of approximately –1117 dB/decade, demonstrating the ADC's sharp filter, as the roll-off of just the analog is only -47 dB/decade.

The main board has a minimum 33-hour battery life using a 500 mAh battery, though

this is dependent on the impedance load. The average current consumption is $\sim$14 mA, which is largely dominated by the gyroscopes' continuous current draw of 10 mA. Additionally, the largest current surges occur when turning on / off the EBI analog, reaching nearly 67 mA. During an EBI sweep lasting 2.68 s, the average current is $\sim$34.7 mA.

The data outputs from the sensors were tested and validated using benchtop equipment to verify that the system yielded accurate measurements. For the audio board, the AFE was characterized using a signal analyzer (SR785, Dynamic Signal Analyzer, Stanford Research Systems, Sunnyvale, CA) and oscilloscope (DSOX3024A Oscilloscope, Keysight Technologies, Santa Rosa, CA). Additionally, the AFE and ADC outputs were compared to known input signals of various amplitudes, wave topologies, and frequencies. The EBI system architecture was extensively characterized in [33], and we validated that the data outputs from the brace matched the expected resistance and reactance values for known loads at every excitation frequency. For the IMUs, we validated the sensor outputs by comparing the acceleration and gyroscope values of the brace sensors when affixed to Xsens IMU units (MTW-38A70G20, Xsens, Enschede, The Netherlands). Lastly, we verified the temperature sensors' readings using a resistance temperature detector (RTD) (HH126, Omega Engineering, Stamford, CT).

4.2.4.2 Drop Sample Analysis

For the audio board, the drop sample analysis recording concluded once the battery died at nine hours. Since the audio board does not capture a timestamp for each individual audio sample but instead timestamps a group of audio samples, this analysis actually examines if a block of data, consisting of 2752 samples of 16-bit data from four channels, is dropped. Theoretically, given the size of the buffer and the sample rate, a data packet contains 58.7 ms of audio data. For the entire recording, the time between successive data blocks was calculated. The observed time differences between blocks were either 58.6 ms or 58.8 ms. This 0.2-ms artifact is a result of the timer resolution, which is 0.2 ms. In short, for the

nine-hour recording, no data blocks were dropped. Refer to Figure 4.5(a) for a histogram of this result.

Unlike the audio board, data acquired with the main board were analyzed on a sample-by-sample basis, as a timestamp for each sample was captured. The recording analyzed was 35 hours long. Sampling for this board is driven by the data-ready interrupt of one the accelerometers, ACC0, which is programmed at 250 Hz. Samples for ACC0 clustered around an average sample period of approximately 3.91 ms, or 16 timer ticks. While there was a distribution of observed sample rates, they were within ± 2 tick values around the 16-timer tick value, which is likely an artifact of the timer resolution and accelerometer internal timer accuracy. The other accelerometer (ACC1) and the gyroscopes (GYR0 and GYR1) are programmed to sample at 100 Hz. The sensors showed no dropped samples with average measured sample periods of 9.3, 10, and 10 ms for ACC1, GYR0, and GYR1, respectively. Similarly, the temperature sensors exhibited no dropped samples with an average period of 1.004 s, while the impedance sweeps were measured approximately every 46.17 s. Like the audio board, this board experienced no dropped samples. Refer to Figure 4.5(b-d) for a histogram of this result.

Though we observed no dropped samples, in the instance that samples are dropped, timestamps of the data will allow for researchers to detect the length (time) of the missed data and determine the appropriate response. Depending on how many samples are dropped, data can be reconstructed (e.g., a few dropped accelerometer samples may be interpolated) or removed entirely from analysis (e.g., prolonged periods of missing data).

4.2.4.3 Proof-of-Concept Recording Results

The signals from the proof-of-concept recordings are plotted in Figure 4.6. For the joint sound measurement (Figure 4.6(a)), joint sounds and IMU data were recorded from the audio and main boards, respectively. Given these boards are time-synchronized, joint sounds can be directly correlated with joint angle, as processed from the IMU data. Importantly,

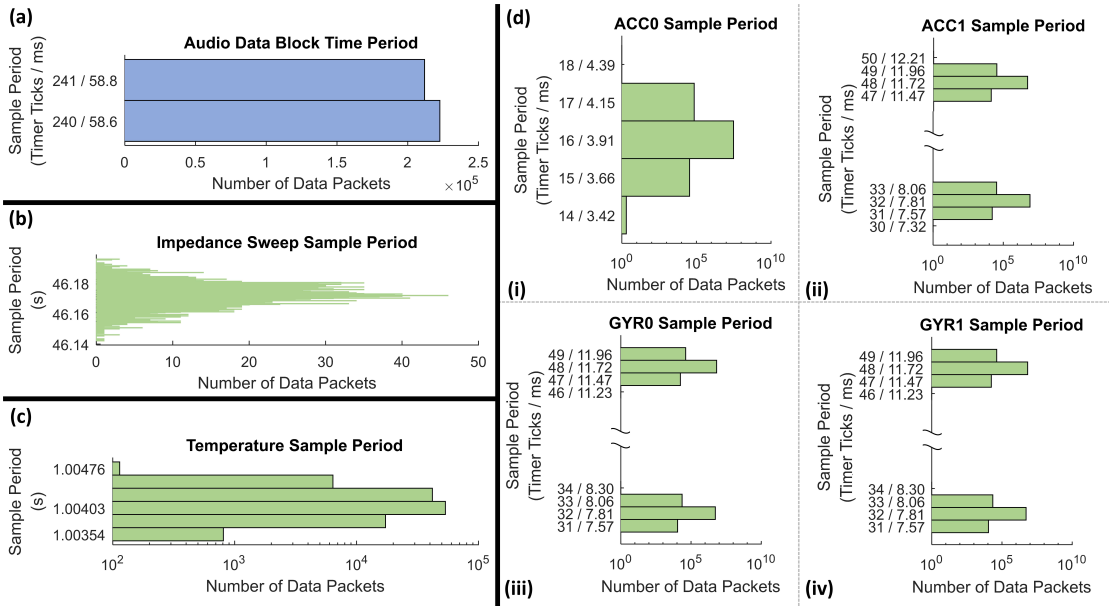

Figure 4.5: Histograms of received data samples or blocks used to show that no samples or data blocks are dropped for all sensors. Each bin width for all histograms is one timer tick wide. (a) Histogram of the audio data blocks received for a 9-hour recording. Data blocks contains 58.7 ms of four channels of 16-bit audio. The timer resolution means causes the timing differences between subsequent received blocks fall between 58.6 and 58.8 ms. (b) Histogram of first frequency sample or the impedance sweep for the 35-hour recording. The average sample period is 46.17 s. (c) Histogram of the instantaneous sample periods—with an average of 1.004 s—for the temperature sensors. (d) Histograms of the instantaneous samples periods for the (i-ii) accelerometers (ACC0/1) and (iii-iv) gyroscopes (GYR0/1), with average sample periods of 3.91, 9.3, 10, and 10 ms, respectively. The timer tick values are provided to show the variability is, in part, a result of the timer resolution.

as shown in Figure 4.6(a), significant acoustic emissions occur at similar joint angles for repeated exercises, which is consistent with our previous work that demonstrated—using benchtop equipment and electret microphones—that "clicks" (i.e., high-amplitude, short-duration, broad bandwidth signatures) occur at consistent joint angles for flexion / extension movements [111].

EBI measurements for 10 sweeps and the ensemble average of the sweeps are plotted in Figure 4.6(b). Of note, individual sweeps are within 1 Ω of the ensemble average, showing repeatability for the static measurement. Further, the curve is consistent with the Fricke-Morse bioimpedance model, which represents tissue segments as a resistor in parallel with a series network of a resistor and capacitor, representing extra- and intra-cellular regions of

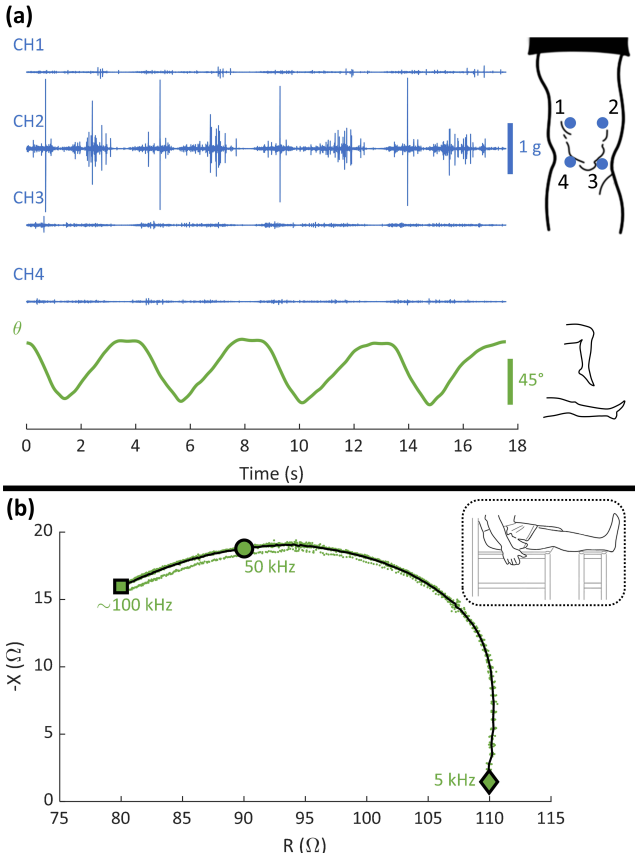

Figure 4.6: Proof-of-concept recordings from a single subject. (a) Joint sounds (blue) recorded for four flexion / extension exercises using four microphones from the positions indicated. The flexion angle (green) is also provided. Importantly, significant acoustic emissions occur at similar joint angles for repeated exercises. (b) Electrical bioimpedance (EBI) sweep from 5 – 96.605 kHz plotted for 10 impedance sweeps (green) and are within 1 Ω of the overall ensemble average across the sweeps (black). Specific frequencies are marked for reference. The measurement was recorded with the subject positioned as shown in the inset. During this measurement, which was conducted in a climate-controlled room, the average skin temperature recorded was 30.4°C.

tissue, respectively.

4.2.5 Limitations

4.2.5.1 Main Board Battery Life

The battery life of main board system can be improved. Currently, it is limited by the average current draw of the IMUs used in this design, specifically the gyroscope of the unit, which draws nearly 5 mA continuously (10 mA for the two used in this system) because

this sensor cannot be put to sleep at the 100 Hz sample rate given its long wakeup time. This IMU was selected to allow for future iterations to readily integrate a magnetometer if necessary. If deemed unnecessary, power consumption may be lowered by exchanging this part for low-power, standalone accelerometers and gyroscopes or a combined package. If a magnetometer is required, a newer version of this part, which was recently released at the time of writing this paper, is available and draws less current, though other IMUs may be selected. Moreover, other power-saving techniques may be employed, such as intelligent, activity-based gating of sensor sampling, capturing only the relevant sensors' data and / or at their minimal sample rate.

4.2.5.2 Adhesive-Based Brace

The brace presented in this work leverages the use of adhesives: the microphones pads and EBI gel electrodes. These adhesives are not conducive for long-term wear, so dry alternatives should be considered for a deployable system. With respect to the contact microphones, such methods must achieve consistent and firm coupling with the skin to capture the joint acoustic signals, and these methods must not add significant noise to the signal during articulation of the knee. Moreover, the brace design itself must not degrade the signal quality with noise sourced from rubbing, brace slippage, or ill-fitting designs. For the electrodes, various metals (preferably those that do not corrode), conductive textiles, and other materials may be evaluated with a particular focus on accuracy, signal-to-noise ratio, and power requirements given the increase in the electrode-to-skin interface impedance [37]. Similar to the microphones, coupling mechanisms to ensure skin contact must be considered. Sanitation and other medical-grade factors when selecting such materials may present additional design constraints.

4.2.5.3 Prototype, Proof-of-Concept Form Factor

The design in this work primarily serves as a proof-of-concept for untethered measurements of joint health, though in its current form, it may be used for in-lab / in-clinic experiments. For example, this brace may immediately replace DAQ-based equipment currently used, especially for clinic-based studies where space is often extremely limited. However, future designs must be optimized for at-home and long-term use. Importantly, efforts to improve upon the form factor—perhaps by adapting the current design to emulate or even retrofit a more traditional brace—could increase user compliance and acceptance of the device [123]. Further, retrofitting a hinged brace, for example, may allow for improved cable management and overall streamlining of the system (i.e., more closely fitted to the body), which would improve comfort and conformity between device and user. Additionally, weatherproofing should be considered to protect the system; for example, utilization of waterproof connectors and other packaging solutions would help prevent rain, sweat, debris, etc., from damaging the electronics.

4.2.6 Summary of Wearable Hardware Design and Future Directions

This section describes the design and validation of a smart, multimodal knee brace for joint health assessment. Custom electronics, firmware, and packaging were developed to provide a comprehensive sensor suite—encompassing joint acoustical emissions, EBI, inertial, and skin temperature data. These data are robustly sampled and saved to on-board storage without dropping packets. Tools, including the implementation of a host computer program and a stencil mechanism for determining sensor placement, were developed and implemented to allow users to interact with the device with minimal training while still achieving high-quality recordings. A 3D-printed brace served to easily place the sensors on the body and house all the electronics. Though this work was developed with the joint health application in mind, other areas may utilize a similar architecture to achieve wearable sensing, in particular with high-rate sensors.

4.3 An Automated Wake-Up System to Trigger Measurements of Joint Sounds and Electrical Bioimpedance

This section describes the first step towards a practical wearable brace that is capable of real-time diagnostics. Ideally, the wearable brace would continuously monitor all modalities of joint health. However, power consumption, storage constraints, and data bandwidth for offline processing preclude continuous sampling of data. Currently, we have switches on the brace for the user to initiate recordings. However, we propose a wake-up system for automatically detecting joint sound exercises of interest (i.e., flexion / extension and sit-to-stand) and correct posture for repeatable EBI recordings without user intervention.

Our early work used on-board, real-time activity recognition of flexion / extension and sit-to-stand exercises on a field-programmable gate array (FPGA)-based processor to gate the recording of joint sounds, achieving a power savings of 12%, but a power consumption of 2.9 W during idle periods still precluded continuous monitoring of joint sounds [124]. This high current consumption is largely the result of using a power-hungry processor (2.6 W typical idle power, myRIO National Instruments, Austin, TX). However, the scheme would likely remain unable to achieve the desired power savings even with implementations on a low-power processor, as the system continuously samples accelerometer data, performs filtering, standard deviation calculations, and threshold comparisons to generate wake-up signals. Moreover, this method did not consider EBI, and our EBI-specific work only implemented post-processing position identification algorithms for segmenting valid periods for EBI analysis [36]. Both the real-time and post-processing approaches used two accelerometers located on the thigh and shank portions of the leg to characterize movement about and orientation of the knee joint.

Accelerometers remain a popular choice for sourcing wake-up circuits. As noted in [125], much work has been dedicated toward optimization of accelerometers. Current commercially-available accelerometers have improved power consumption characteristics

(e.g., 0.68 μW at super-low output data rates for the IIS2DLPC from STMicroelectronics, Geneva, Switzerland). Notably, a recently (2017) fabricated accelerometer and corresponding wake-up system (tuned for a target frequency) consumes 5.4 nW as part of a research effort [126]. One challenge with using accelerometer outputs is efficiently discriminating specific leg movements for joint sound measurements from other motions encountered during everyday activity. Alternatively, encoders and potentiometers have been a practical choice for direct instrumentation of joint-based device (e.g., a string-based potentiometer as part of a flexible knee brace as shown in [127]); however, both would likely require processor involvement for analyzing joint angle. Moreover, these sensors do not provide orientation information about the leg.

We propose a simple method for detecting relevant activities and / or body positions—for recording joint sound or EBI measurements, respectively—via a hinged knee brace instrumented with contact-based switches and using step and orientation data provided from an accelerometer for improved real-time classification. With this approach, continuous monitoring of joint health may be achieved, especially for at-home use cases, without the need for cumbersome user-involvement to "turn-on" the system for measurements.

4.3.1 Wake-Up System Design

The wake-up system (WUS) is comprised of a sensorized hinge on a knee brace, a microcontroller (MCU), and an inertial measurement units (IMU). The WUS architecture, which is summarized in Figure 4.7, operates on a simple scheme; a low-power MCU in a sleep state will wake-up from an event—driven by equally low-power switches and accompanying circuits—and confirm the occurrence of an activity by leveraging additional information from the IMU. If an activity of interest is recognized, the system will trigger a more "power-hungry" system to record joint health data. Two types of activities are classified by the WUS: (1) exercises performed for recording of joint sounds, specifically flexion / extension and sit-to-stand movements, and (2) appropriate posture for consistent

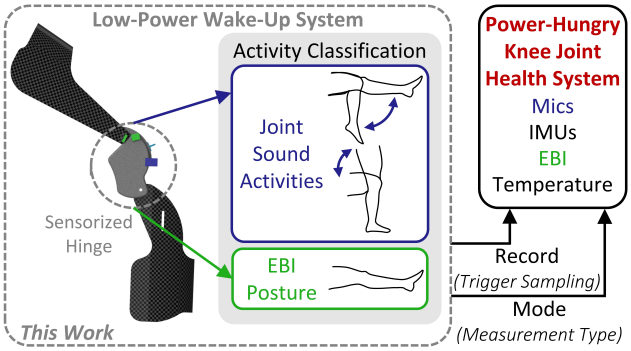

Figure 4.7: A low-power system, leveraging a sensorized hinged knee brace, for automatically detecting instances of joint sound activities—flexion / extension and sit-to-stand—as well as posture for electrical bioimpedance (EBI) measurement. This low-power system is intended to trigger a joint health system measuring data from microphones, inertial measurement units (IMUs), EBI, and skin temperature sensors.

acquisition and analysis of EBI. The system not only sends the start and stop sequence for a recording (*RECORD* signal) but also the type of recording (*MODE* signal) such that only the relevant sensors are sampled for a joint sound or EBI measurement, economizing battery life.

4.3.1.1 Switch Mechanism and Interrupt Generation

The recognition of both activities starts via a similar mechanism; custom-made contact switches retrofitted to the brace's hinge generate interrupt signals to the MCU (Figure 4.8). These switches were affixed to a commercially-available hinged knee brace (Flex, Össur hf., Reykjavík, Iceland) intended for various ligament instabilities (Figure 4.8). Both switches consisted of two components, one mounted on the stationary part of the hinge and one on the moving portion. Note that this brace utilizes a three-linkage mechanism, with the middle link encased in "stationary" plastic enclosure with respect to the outer, rotating linkages. The switches were printed using a polylactic acid (PLA) or thermoplastic polyurethane (NinjaFlex, NinjaTek, Manheim, PA) materials for the rigid and flexible components, respectively. Copper shims (0.254 mm thick) were epoxied to each printed piece to provide the contacts for the switch.

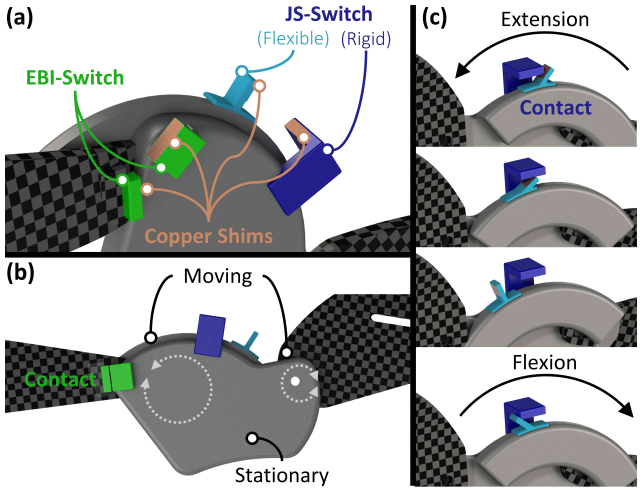

Figure 4.8: The sensorized hinge. (a) Lateral view of the two switches on the hinge. The joint sounds switch (JS-switch) is comprised of a stationary, rigid piece mounted on the stationary arm of the joint, while a flexible piece affixed a moving arm can bend to travel beneath the rigid piece. The electrical bioimpedance switch (EBI-switch) consists of two rigid pieces. Copper shims epoxied to the pieces provide the mechanism for making electrical contact. (b) Lateral view of the hinge with the brace fully extended. In this position, the two EBI-switch components make continuous contact. Also noted are the rotation arms of the three-linkage hinge joint. (c) Progression of the JS-switch (as viewed from the inside of hinge) as the leg extends and then flexes. This switch only makes momentary contact when extending the leg from large flexion angles; it does not make contact during flexion.

The first switch (joint-sounds switch [JS-switch]) is positioned to make momentary contact at approximately 72° flexion angle (i.e., where 0° represents full extension), which falls within the range of motion for flexion / extension and sit-to-stand motions but generally excludes walking tasks, as the average maximal flexion angle during the gait cycle is 60° [128]. Note that while stair-walking does typically achieve this higher flexion angle, it may be beneficial in future work to capture joint sounds during such high knee power exercises as the sounds may contain information regarding vertical loading forces on the joint [48]. This interrupt signal is normally driven high using a weak pull-up resistor, and extension of the brace from acute angles grounds the line, creating a falling edge—filtered using switch-debounce circuitry—for the MCU to detect. This switch uses both the rigid and flexible materials. The rigid piece is mounted at the fixed 72° angle, and the flexible component bends to travel beneath it. This is to ensure contact is only made during

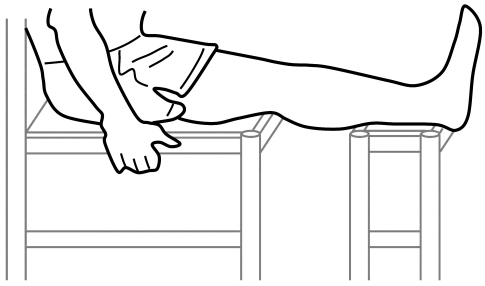

Figure 4.9: Correct posture for electrical bioimpedance (EBI) measurements at this time. The leg is fully-extended and supported.

one phase of motion, constraining the conditions under which an interrupt may be generated. Note the mounting angle of the switch can be adjusted to modify the sensitivity of the wake-up interrupt signal, possibly to account for acute stages of rehabilitation where range-of-motion is limited, for example.

The second switch (EBI-switch) closes when the leg is at its maximal extension angle, which is a key attribute of our preferred EBI posture: the subject seated with the leg is fully-extended and supported, providing an easily-achieved, repeatable position that is less susceptible to minimal motion artifacts (Figure 4.9). Given EBI measurements in our previous work called for a minimum recording time of 60-seconds [36], the supporting circuit for this switch utilized charging time constants of a resistor-capacitor circuit to ensure the extended position was held for a sufficient amount of time before generating an interrupt. During charging, the capacitor is simultaneously discharged at a slower rate, providing a means for the circuit to reset for repeated measures. While this could also be accomplished by shorting the capacitor through the MCU when needed, we decided on the external resistor to minimize MCU intervention and accommodate the case where some charge is stored but does not reach a voltage level high enough to trigger an interrupt; this is one of the simplest methods for guaranteeing the extended position is maintained.

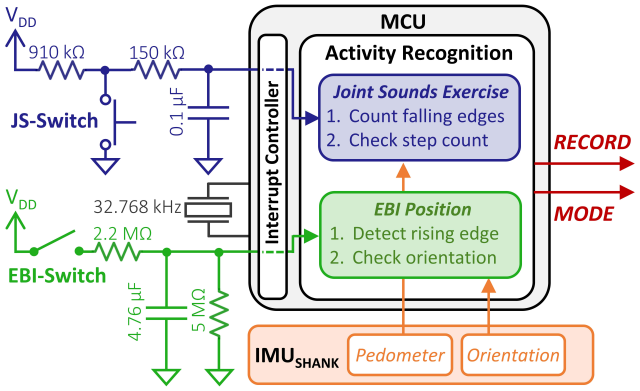

Figure 4.10: Wake-up system overview. Interrupt signals generated from joint-sounds and electrical bioimpedance switches (JS-Switch and EBI-Switch, respectively) on the knee brace hinge joint wake up the microcontroller (MCU). The Activity Reignition algorithm uses the interrupts, timing considerations, and pedometer and orientation information from an inertial measurement unit (IMU) to classify activities and sends signals to the main system to start (*RECORD*) a specific type of recording (*MODE*).

4.3.1.2 Microcontroller-Based Classification

The MCU (PIC18F46K40, Microchip, Chandler, AZ) remains in a low-power state until an interrupt from either the JS- or EBI-switches is triggered. This MCU was selected for its low power consumption during sleep mode even when clocking from an external crystal oscillator. As noted previously, the MCU leverages information, specifically step counts (pedometer) and orientation, polled from an IMU (LSM6DSL, STMicroelectronics, Geneva, Switzerland) to provide additional context from the interrupts. The IMU is mounted to the distal segment of the brace on the frontal pane such that its axes align with the brace edges and faces, and thus the leg, with respect to the global (gravitational) frame.

If a JS-switch fires, the MCU wakes and initializes the IMU and its pedometer function. Additionally, the MCU starts a timer clocked from an external 32.768 kHz crystal oscillator and begins searching for two more instances of this switch signal to occur within eight seconds, effectively detecting if four cycles of an exercise have been completed. Once completed, the MCU polls the IMU, checking to see if steps were detected. If so, the MCU is put into a sleep state, as our current systems only require joint sounds recorded during the described activities. However, if no steps are recognized, the MCU initiates a joint sound

recording, sending *RECORD* and *MODE* signals. We determined that the pedometer was most reliable after a few seconds had elapsed, and thus in addition to the minimum number of cycles needed to trigger a recording, a minimum amount of time is required to accurately register valid steps and make decisions for recording. While the pedometer function may be unnecessary for level-terrain walking since the JS-switch should not go low, stair-walking presents an activity where flexion angles are more extreme and would activate the JS-switch interrupt. The recording is stopped six seconds after receiving the last interrupt from the JS-switch. While this scheme requires four cycles of the exercise to be completed to start a recording, these initial unrecorded cycles serve as a preconditioning period for the joint itself [77].

An EBI-switch is supplied to the MCU after a minimum charge time of $\sim$20 seconds. Upon receiving the interrupt and waking from a deep sleep state, the MCU powers and initializes the IMU and polls it to determine if the orientation of the IMU, and thus shank, is perpendicular to the gravitational field. If this condition is met, the leg is assumed to be in the EBI posture, as a fully-extended leg (EBI-switch interrupt) with the shank in the desired orientation is in all likelihood the EBI position. The recording is stopped when a falling edge is detected on the interrupt line or an interrupt on the JS-switch is recognized.

4.3.1.3 System Characterization

The current consumption of the WUS system was measured at 1 kHz using an Agilent Digital Multimeter (34410A, Keysight Technologies, Santa Rosa, CA) in series with its battery (LP-523334 3.7 V 500 mAh with PCM, Shenzhen PKCELL Battery Co., Ltd, Guangdong Sheng, China).

4.3.1.4 Human Subject Pilot Study

All studies obtained approval from the Institutional Review Board (IRB) at the Georgia Institute of Technology and written informed consent was obtained from all participants.

The device was worn by four healthy subjects (one female, age: 24 – 32 years, height: 165 – 180 cm, weight 56 – 90 kg) while they performed various different movement and posture tasks: (1) standing, (2) sitting with both feet on the ground, (3) sitting with legs crossed at the thigh, (4) sitting with legs fully extended and supported, (5) walking, (6) stair walking during ascent and decent, (7) seated flexion / extension, and (8) sit-to-stand. Of note, these exercises encompassed all the activities tested in our previous work for classification of optimal EBI position [36]. Each activity lasted a minimum of 30 s (90 s for Task 4) or 10 cycles for cyclic tasks (Tasks 7-8) and was repeated twice. Further, the order of the activities for each subject was randomized to help eliminate the influence of prior system states. Lastly, a researcher observed the WUS LEDs to determine if the task was correctly or incorrectly identified.

4.3.2 Results and Discussion

4.3.2.1 System Characterization Results

The WUS current consumption waveform for joint sound exercises and EBI posture recognition are plotted in Figure 4.11(a) and (b), respectively. The MCU remains in a low-power state when sleeping and not handling interrupts at $\sim$300 nA. When woken up, the MCU consumes approximately 230 µA. Most of the power draw is attributed to the IMU functions, even though the IMU only uses the accelerometer. During the pedometer initialization, the current draw reaches a peak current consumption of $\sim$3.1 mA.

4.3.2.2 Human Subject Study

The confusion matrix produced from four subjects' worth of data is shown in Figure 4.12. The system performed well with only a few misclassifications. However, given the conditions of the current and prior states, these misclassifications were generally expected based on the MCU's state machine. The one false classification of flexion / extension occurred because the subject failed to fully flex his knee beyond the JS-switch angle of 72°. In this

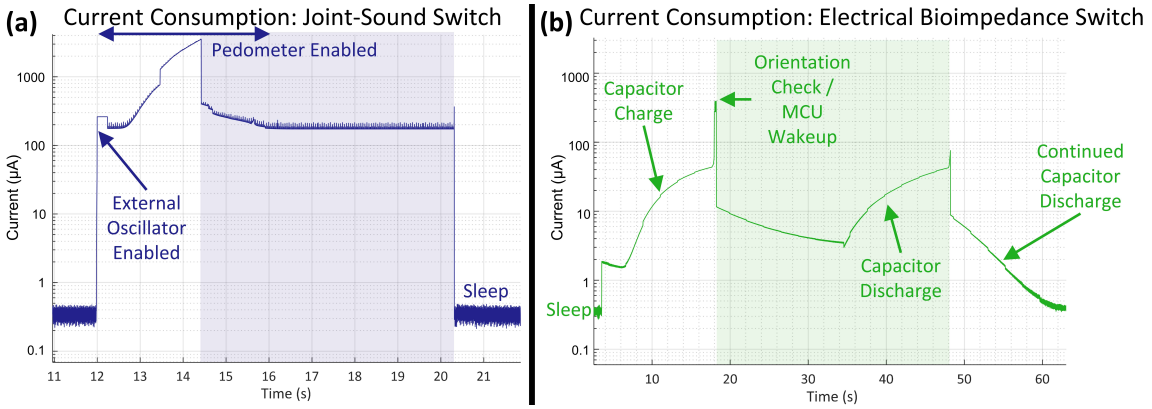

Figure 4.11: Wake-up system (WUS) current consumption. (a) Current consumption for detecting joint sound recordings via the joint-sound switch (JS-Switch). The microcontroller (MCU) starts in a sleep state at ∼300 nA. When the knee flexes beyond ∼72°, an interrupt is generated, waking-up the MCU (∼230 µA). The MCU initializes a 4-second timer clocked from an external real-time crystal oscillator. Additionally, the pedometer function of the pedometer is enabled, which is power-hungry at peak current draws of ∼3.1 mA. The pedometer remains enabled for four seconds before disabling, allowing for the pedometer to accurately register steps, which is polled by the MCU. If no steps are detected and a minimum of four extension cycles have been completed, a recording will be started (blue shaded area). A recording lasts for six seconds after receiving the last JS-Switch interrupt. At this time, the MCU goes back to sleep. (b) Current consumption for detecting electrical bioimpedance (EBI) posture via interrupts from the EBI-Switch. The MCU starts in the sleep state. The leg is held in the fully-extended position, closing the EBI-Switch and charging the capacitor. Once the capacitor is sufficiently charged, the MCU wakes via an interrupt, enables the IMU, and quickly polls the IMU for its orientation before disabling. If the orientation is correct, an EBI recording is started (green shaded area). When the leg flexes, opening the EBI-Switch, the capacitor discharges, and the MCU wakes when it recognizes a low signal. The MCU stops the recording and goes to sleep, and the capacitor continues to discharge.

case, the system did successfully classify that the subject did not complete a *correct* flexion / extension exercise, as this healthy subject was capable of full range-of-motion (ROM). Nevertheless, this demonstrates that the system may need to be tuned to individuals depending on their current ROM, which is significantly limited during early stages of rehabilitation following an acute injury and subsequent surgery. Given the simple mechanical design, this would be easily achievable. An additional incorrect classification of electrical bioimpedance (EBI) occurred when the subject completed 30 seconds of standing before moving to the EBI position, thus failing to provide a valid rising edge once moving into

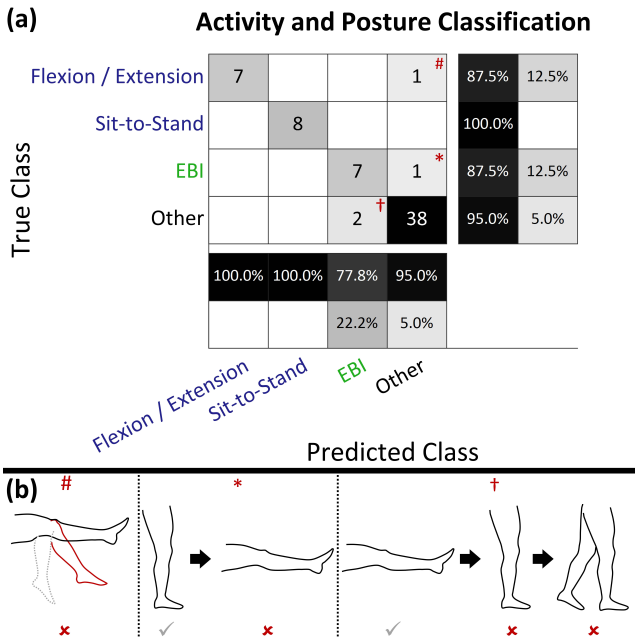

Figure 4.12: Confusion matrix for activity classification for four subjects performing a variety of randomly ordered tasks. The True Class represents the activity performed by the subjects, while the Predicted Class provides the wake-up systems' output: recognition of a joint sounds activity (i.e., flexion / extension or sit-to-stand), a valid electrical bioimpedance posture, or other activity during which no recording should be initiated. The misclassifications are marked in (a) and illustrated further in (b).

position. Lastly, the two activities immediately following an instance of EBI for one subject—standing still and walking—were incorrectly identified as EBI and, in fact, a continuous measurement from the correctly identified EBI position because the EBI-capacitor did not discharge enough to generate a falling edge to stop the EBI recording. This primarily occurred since this subject kept his legs straight when moving from the EBI position to the standing (vs. bending the legs to a standard seated position before standing, which would have immediately ended the EBI measurement). We anticipate that these failed scenarios would be infrequent; moreover, even with a few "false negatives" where the occurrence of a motion / position of interest is missed by the system, most of the occurrences can still be detected, and the overall burden for the subject would still be alleviated as compared to the use of a on-off switch and / or requirement for more frequent charging of the battery.

4.3.3 Limitations and Potential Improvements

The current consumption for the WUS is not necessarily optimized. Though techniques for reducing current consumption may be considered, it is important to balance system complexity with the overall power savings in the context of the integrated application (e.g., determining if saving a few microamps extends battery life significantly and / or is perceivable to the user). The pedometer used for rejecting step-based activities draws the most current in the WUS by an order of magnitude. Replacing the pedometer with an ultra-low power accelerometer configured in a motion-triggered mode may provide an opportunity for greater power savings, though thresholding would need to be selected to discriminate step-based from joint sound activities. However, future implementations may exclude the pedometer altogether if the wearable brace should additionally capture stair-walking. As mentioned above, stair-walking may prove to be an interesting task with respect to joint sounds, as it may provide an alternative to or expand upon repeated sit-to-stand, or squatting, motions given the increased loading forces on the joint.

Similarly, for EBI detection, a future optimization may consider using an ultra-low power accelerometer(s) (e.g., ADXL362, Analog Devices, Inc., Norwood, MA) for detecting prolonged periods of inactivity to generate an interrupt to the MCU, which may then check for correct orientation. Typical use-case studies would help identify which approach would result in better power savings; while the accelerometer approach may draw less current than the EBI-switch to detect the fully-extended position, it may wake the MCU more frequently, diminishing the initial power savings. Moreover, this mechanism may offer an opportunity to appropriately handle edge cases, namely the case when moving from a prolonged standing to the correct measurement position, for correct classification of EBI, as it may provide more frequent, and perhaps more deterministic, MCU intervention for position checking.

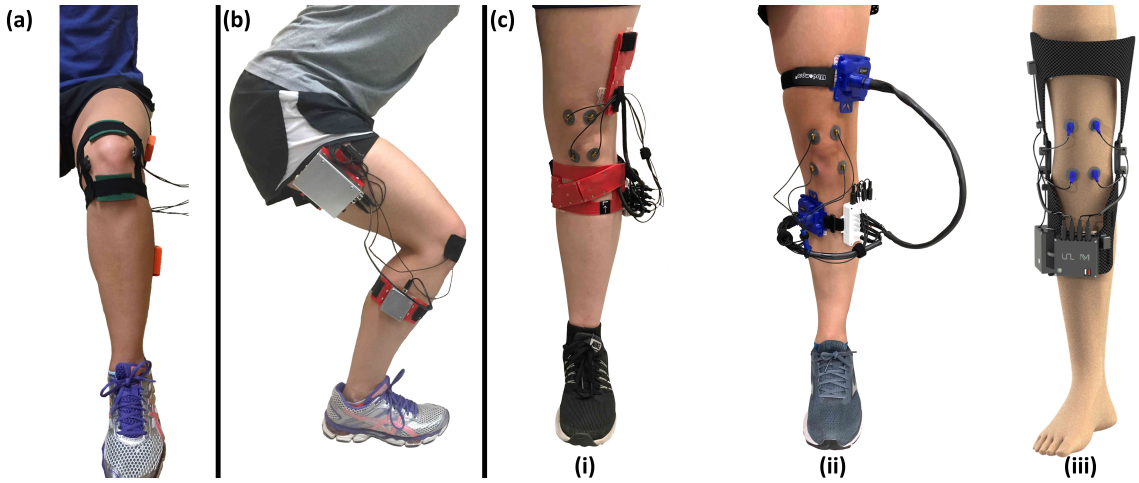

Figure 4.13: Evolution of the hardware presented in this thesis work. (a) Initial tethered system, collecting acoustics and inertial measurement data using benchtop equipment as described in Chapter 3. (b) Initial attempt at wearable acoustics (not described in this thesis explicitly but detailed in [70]). (c) Optimization of wearable system described in Chapter 4. An initial design (i) was fabricated and ultimately finalized as (ii) for initial proof-of-concept studies. The rendering depicted (iii) shows future plans for the wearable system that retrofits a commercially-available hinged brace.

4.3.4 Summary of the Wake-Up System Design

In this section, we demonstrated a real-time, wake-up circuit for detecting instances of exercises and correct posture for joint sounds and EBI data acquisition, respectively. In the immediate future, this real-time classification system may facilitate simpler user interactions with the device and promote user wear compliance. Looking towards long-term applications, as joint sounds become more understood from a signals and data standpoint, perhaps more complex exercises may be used for analyses for outputting a "joint health score." By capturing complex, every-day activities, such as walking or stair climbing (with modification of the WUS to trigger on these tasks), in an unobtrusive manner, a more realistic snapshot of the joint may be captured, as the user is not necessarily acutely aware of their movements. Thus, a joint score derived from more representative day-to-day activities may be explored.

4.4 Conclusion and Future Work

This chapter presents methods for acquiring measures of joint health in a wearable form factor. We implemented a two-microcontroller system with one microcontroller sampling high-bandwidth, multi-channel microphone data, while the second samples EBI, IMU, and temperature data. The data are saved on microSD cards, and a custom one-click program transfers this data from the device to a computer via a USB cable. We retrofitted the embedded system into a custom 3D-printed brace and provided users—patients, study coordinators, or researchers—with a simple, "stencil" mechanism for properly adhering the brace to the knee in a repeatable fashion. We characterized the system and validated that robust sensing and sampling was achieved. Figure 4.13 shows the optimization of the hardware described in this chapter. Lastly, we presented an initial real-time wake-up architecture on a commercially-available hinged brace for automatically detecting times to measure joint sounds or EBI, which we believe will help ease user interaction with the device. Future work will combine the embedded and wake-up systems on a hinged brace, as a traditional brace will present a more user-friendly look and ease putting on the device, which may help with users comply with wearing the device. Future brace optimizations will consider elimination of adhesives, including the gel electrodes and double-sided tape used for EBI and microphone measurements, respectively. Note, any future mechanical optimizations must consider noise characteristics of the brace.

CHAPTER 5
CONCLUSION AND FUTURE WORK

5.1 Conclusion

Orthopedics—in particular joint health assessment—is an area where wearable devices may provide clinicians and patients with more readily available quantitative data. Recently, wearable sensing modalities for the knee joint have been explored to assess joint health. Such sensing modalities include the measurement of joint acoustics, edema, and activity via microphones, electrical bioimpedance (EBI) circuitry, and inertial measurement units (IMUs), respectively. For example, studies pre-dating this thesis have used joint acoustical emissions ("joint sounds") to discriminate healthy subjects and those with osteoarthritis [21, 129] and classify varying conditions of the patellofemoral joint [22], while recent studies—leveraging the initial findings (Section 3.2) of the thesis—have monitored improvements in kids with juvenile idiopathic arthritis after receiving effective medication [130] and tracked changes in loading stresses on the joint [48]. Similarly, EBI has been used to detect swelling (edema) of the joint [34], and studies have demonstrated its efficacy for detecting changes in edema during injury recovery [36]. Lastly, researchers have leveraged IMUs to provide information about knee valgus / joint stability [131], range of motion [42, 132], and joint kinematics [133] on their own, while also providing contextual information when combined with other sensing modalities, such as noting the angular location at which joint sounds occur [111]. Ultimately, joint acoustics, edema, and kinematics aim to capture some underlying physiological state or anatomical change within the joint itself.

However, prior to this dissertation, the "wearable" aspects of such approaches were limited to in-lab / in-clinic environments and often relied on benchtop equipment and data acquisition units. Moreover, the integration of the sensors into a "smart brace" was first

conceived as part of this dissertation, and was enabled by the investigation of miniature acoustic and vibration sensors for joint sound measurements, as well as the development of high fidelity electronics for their recording in a brace. Importantly, this work translated such sensors into a fully untethered smart brace for the first time, to the best of our knowledge. Specifically, as a first step, we investigated miniature microphones suitable for wearable applications, examining aspects such as signal-to-noise-and-interference ratio and frequency response for sensing joint sounds for microphones with power consumption compatible with battery-powered devices and appropriate sizes for incorporation within a brace. We validated the sensing capabilities of these sensors and, importantly, performed an initial human subject study to demonstrate robust and repeatable sensing of acoustic events for sets of cyclic exercises. A subsequent larger human subject study was conducted, and initial trends for healthy subjects were characterized. Importantly, we successfully tracked rehabilitation improvements in athletes following an acute injury.

Equipped with suitable microphones, we tackled the engineering task of sampling four of these high-bandwidth sensors—as well as acquisition of other sensing modalities of joint health (EBI, IMUs, and temperature sensors)—on a battery-powered, completely untethered embedded platform, and the resulting system was integrated into a 3D-printed wearable "brace." In addition to ensuring the sensor suite robustly sampled and saved data, we implemented methods to simplify device usage including one-click USB transfer of data to the computer and a "stencil"-based approach to aid proper mounting of the device, especially for inexperienced users. Other wearable considerations included a wake-up system to automatically trigger measurements of joint sounds and EBI, which may be used to limit required user-interaction with hardware while also providing a means to potentially measure data during every-day—and perhaps during "unconscious," proprioception-rooted activities.

5.2 Future Directions

5.2.1 Hardware Directions

While this work serves as an initial scheme for foreseeable brace implementations, there are many opportunities for improvements in hardware design. Future iterations will likely leverage traditional knee brace form factors, either retrofitting or emulating current hinged designs to aid user adoption and wear compliance. Such hinge-based designs allow for flexibility in hardware design given the large surface area and, perhaps most importantly, direct access to the joint that theoretically allows for the most amount of energy harvesting on the body [134]. Hinged-based designs have been used in the literature to harvest energy using a variety of techniques, but most focused on generation of power from knee motion [135–138]. Other techniques involve exploiting strain and thermal energy in the form of muscle forces and body heat, respectively, providing other opportunities and mechanisms to harness energy [139]. Wearables in the literature have demonstrated to achieve power on the order of micro- to miliwatts [139].

Such energy harvesting techniques would benefit greatly from electronics with reduced power consumption. While this work used commercially-available integrated circuits (ICs), implementation of application-specific integrated circuits (ASICs) and system on chips (SoCs) would improve power requirements. For example, research towards electroencephalogram (EEG) and electrocorticography (ECoG) have worked towards low-power, multi-channel acquistion at appreciable bit-depths and sample rates as well as on-chip classification of signals for closed-loop seizure detection and control [140, 141]. Moreover, on-board processing and / or compression of raw joint acoustic signals may facilitate energy-efficient, wireless transmission of data from the brace [112, 142].

Lastly, modification and expansion of the sensing modalities may provide a richer dataset for joint health assessment. For example, in this work, we only examine EBI as a method to detect joint swelling. Research has shown that circumferential EBI arrays can

be used for high resolution tomography [143,144], and integration of EBI tomography may be able to detect localized areas of edema in a future brace. Moreover, we currently only employ passive acoustic sensing; however, active sensing may be able to provide information about muscle-tendon loading [145].

5.2.2 Clinical Directions

In the immediate future, we anticipate the wearable system being used in-clinic given its accessible form (vs. setting up cabled data acquisition units within an often-small examination room). The easy-to-use system can be readily deployed by physicians and / or study coordinators with access to large clinical populations and their associated medical records. Such studies may enable greater understanding of joint sound signals, as knowledge of these signals and their properties is still in its infancy, largely due to a lack of cross-sectional databases and research exploring the origin and propagation of the signals.

Moreover, the joint sound data that has been collected has been limited to measurements recorded during simple motions, namely seated flexion / extension, sit-to-stand (or squatting / leg-press) maneuvers, and, less frequently, treadmill walking. These exercises have been leveraged due to their simplicity, which, from a research perspective, aids the validity of controlled, repeated-measures experiments and also mitigates certain limitations imposed by cables, such as noise produced by cable motion and constraints on the distance a subject may travel from a wired data acquisition unit (DAQ). An untethered system can accommodate more complex motions and everyday activities, possibly enriching datasets for understanding physiological responses to different biomechanical conditions.

Likewise, the scope of these studies can be expanded beyond the clinic with a wearable system. At-home studies may be of interest for long-term monitoring of medication efficacy or rehabilitation progress, and telemedicine (or mHealth) is directly relevant to current needs in the joint health space. For example, pediatric rheumatology may benefit greatly from telemedicine; given a low supply of specialists, families are often required to travel far

distances, incurring significant financial and time costs, especially when factoring the need for multiple visits [146]. A system which could readily classify a successful medication regimen, for example, may be particularly useful and potentially save patients an unnecessary trip to the clinic. Further, at-home studies may examine changes in joint health status throughout the course of a day. For example, patients with osteoarthritis report stiffness of the joint in the morning or after long periods of inactivity [147]. The brace may be used to record data immediately after a patient wakes in such cases or may even be used to explore whether the joint follows some circadian pattern like those followed by other physiological signals such as blood pressure [148]. These throughout-the-day measurements cannot be readily obtained with current clinical tools, and thus our design presents an opportunity to measure unique, rich, quantitative data. Ultimately, we envision this work will serve as the fundamental electronic design for future braces, thus deepening our understanding of sensorized joint health monitoring and broadening its applications.

REFERENCES

[1] P. D. Austermuehle, "Common knee injuries in primary care," *Nurse Pract.*, vol. 26, no. 10, pp. 26, 32–38, 41–45, Oct. 2001.

[2] B. E. Gage *et al.*, "Epidemiology of 6.6 million knee injuries presenting to United States emergency departments from 1999 through 2008," *Acad. Emerg. Med.*, vol. 19, no. 4, pp. 378–85, Apr. 2012.

[3] P. J. McMahon and H. B. Skinner, "Sports medicine," in *Current Diagnosis & Treatment in Orthopedics*, 3rd ed., H. B. Skinner, Ed. New York, NY USA: Lange Medical Books, 2003, pp. 155–173.

[4] W. C. Whiting and R. F. Zernicke, Eds., *Biomechanics of Musculoskeletal Injury*. Champaign, IL, USA: Human Kinetics, 2008.

[5] W. R. Smith *et al.*, "Musculoskeletal trauma surgery," in *Current Diagnosis & Treatment in Orthopedics*, 3rd ed., H. B. Skinner, Ed. New York, NY, USA: Lange Medical Books, 2003, pp. 134–142.

[6] M. Majewski *et al.*, "Epidemiology of athletic knee injuries: A 10-year study," *The Knee*, vol. 13, no. 3, pp. 184–8, June 2006.

[7] J. M. Hootman *et al.*, "Epidemiology of collegiate injuries for 15 sports: Summary and recommendations for injury prevention initiatives," *J. Athl. Train.*, vol. 42, no. 2, pp. 311–9, Apr.–June 2007.

[8] J. G. Ingram *et al.*, "Epidemiology of knee injuries among boys and girls in US high school athletics," *Am. J. Sports Med.*, vol. 36, no. 6, pp. 1116–22, June 2008.

[9] G. S. Smith *et al.*, "Hospitalization due to injuries in the military: Evaluation of current data and recommendations on their use for injury prevention," *Am. J. Prev. Med.*, vol. 18, no. 3, Suppl. 1, pp. 41–53, Apr. 2000.

[10] J. M. Hootman *et al.*, "Epidemiology of musculoskeletal injuries among sedentary and physically active adults," *Med. Sci. Sports Exerc.*, vol. 34, no. 5, pp. 838–44, May 2002.

[11] "Common knee injuries," http://orthoinfo.aaos.org/topic.cfm?topic=a00325, (accessed: Aug. 10, 2015).

[12] "Arthritis in america," https://www.cdc.gov/vitalsigns/arthritis/index.html, (accessed: March 15, 2019).

[13] Y.-L. Zheng *et al.*, "Unobtrusive sensing and wearable devices for health informatics," *IEEE Trans. Biomed. Eng.*, vol. 61, no. 5, pp. 1538–1554, May 2014.

[14] A. Rampp *et al.*, "Inertial sensor-based stride parameter calculation from gait sequences in geriatric patients," *IEEE Trans. Biomed. Eng.*, vol. 62, no. 4, pp. 1089–1097, Apr. 2015.

[15] L. Atallah *et al.*, "Observing recovery from knee-replacement surgery by using wearable sensors," in *Proc. Int. Conf. Body Sensor Netw.*, Dallas, TX, USA, 2011, pp. 29–34.

[16] L. D. Toffola *et al.*, "A wearable system for long-term monitoring of knee kinematics," in *Proc. IEEE-EMBS Int. Conf. Biomed. Health Informat.*, Hong Kong, China, 2012, pp. 188–191.

[17] S. C. Abbott and M. D. Cole, "Vibration arthrometry: A critical review," *Crit. Rev. Biomed. Eng.*, vol. 41, no. 3, pp. 223–42, 2013.

[18] O. T. Inan *et al.*, "Wearable knee health system employing novel physiological biomarkers," *J. Appl. Physiol.*, vol. 124, no. 3, pp. 537–547, March 2018.

[19] Y. Wu *et al.*, "Computer-aided diagnosis of knee-joint disorders via vibroarthrographic signal analysis: a review," *Crit. Rev. Biomed. Eng.*, vol. 38, no. 2, pp. 201–24, 2010.

[20] R. A. Mollan *et al.*, "A critical appraisal of auscultation of human joints," *Clin. Orthop. Relat. Res.*, no. 170, pp. 231–7, Oct. 1982.

[21] L. K. Shark *et al.*, "Discovering differences in acoustic emission between healthy and osteoarthritic knees using a four-phase model of sit-stand-sit movements," *Open Med. Inform. J.*, vol. 4, pp. 116–25, 2010.

[22] J. H. Lee *et al.*, "Vibration arthrometry in patients with knee joint disorders," *IEEE Trans. Biomed. Eng.*, vol. 47, no. 8, pp. 1131–3, Aug. 2000.

[23] S. Tavathia *et al.*, "Analysis of knee vibration signals using linear prediction," *IEEE Trans. Biomed. Eng.*, vol. 39, no. 9, pp. 959–970, Sept. 1992.

[24] R. M. Rangayyan and Y. F. Wu, "Screening of knee-joint vibroarthrographic signals using statistical parameters and radial basis functions," *Med. Biol. Eng. Comput.*, vol. 46, no. 3, pp. 223–32, Mar. 2008.

[25] T.-F. Lee *et al.*, "Analysis of vibroarthrographic signals for knee osteoarthritis diagnosis," in *Proc. 6th Int. Conf. Genetic Evol. Comput.*, Kitakyushu, Japan, 2012, pp. 223–228.

[26] S. Krishnan *et al.*, "Adaptive time-frequency analysis of knee joint vibroarthrographic signals for noninvasive screening of articular cartilage pathology," *IEEE Trans. Biomed. Eng.*, vol. 47, no. 6, pp. 773–783, 2000.

[27] K. Umapathy and S. Krishnan, "Modified local discriminant bases algorithm and its application in analysis of human knee joint vibration signals," *IEEE Trans. Biomed. Eng.*, vol. 53, no. 3, pp. 517–523, March 2006.

[28] S. Cai *et al.*, "Knee joint vibration signal analysis with matching pursuit decomposition and dynamic weighted classifier fusion," *Comput. Math Methods Med.*, vol. 2013, March 2013, Art. no. 904267.

[29] A. Martin and J. Voix, "In-ear audio wearable: Measurement of heart and breathing rates for health and safety monitoring," *IEEE Trans. Biomed. Eng.*, vol. 65, no. 6, pp. 1256–1263, June 2018.

[30] B. Travaglione, "Using a single-board microcontroller and ADC to perform real-time sonar signal processing," in *Proc. of Acoustics: The Second Australian Acoustical Societies Conf.*, Brisbane, Australia, 2016.

[31] C.-C. Wang *et al.*, "Development of MSP430-based ultra-low power expandable underwater acoustic recorder," *Ocean Engineering*, vol. 36, no. 6, pp. 446–455, May 2009.

[32] E. Stranden, "A comparison between surface measurements and water displacement volumetry for the quantification of leg edema," *J. Oslo. City Hosp.*, no. 31, pp. 153–155, 1981.

[33] R. B. Frobell *et al.*, "The acutely ACL injured knee assessed by MRI: changes in joint fluid, bone marrow lesions, and cartilage during the first year," *Osteoarthr. Cartil.*, vol. 17, no. 2, pp. 161–167, Feb. 2009.

[34] U. G. Kyle *et al.*, "Bioelectrical impedance analysis—part I: review of principles and methods," *Clin. Nutr.*, vol. 23, no. 5, pp. 1226–1243, Oct. 2004.

[35] S. Grimmes and O. Martinsen, *Bioimpedance and Bioelectricity Basics*, 2nd ed. Elsevier Ltd., 2008.

[36] S. Hersek *et al.*, "Wearable vector electrical bioimpedance system to assess knee joint health," *IEEE Trans. Biomed. Eng.*, vol. 64, no. 10, pp. 2353–2360, Oct. 2017.

[37] Y. M. Chi *et al.*, "Dry-contact and noncontact biopotential electrodes: Methodological review," *IEEE Rev. Biomed. Eng.*, vol. 3, pp. 106–119, 2010.

[38] G. Medrano *et al.*, "Skin electrode impedance of textile electrodes for bioimpedance spectroscopy," in *13th Int. Conf. Elect. Bioimpedance and 8th Conf. Elect. Impedance Tomography*, H. Scharfetter and R. Merwa, Eds., Graz, Austria, Aug. 2007, pp. 260–263.

[39] P. Rai *et al.*, "Smart healthcare textile sensor system for unhindered-pervasive health monitoring," in *Proc. SPIE*, vol. 8344, San Diego, CA, USA, March 2012, Art. no. 83440E.

[40] M. N. Sawka, "Body fluid responses and hypohydration during exercise-heat stress," in *Human performance physiology and environmental medicine at terrestrial extremes*, K. B. Pandolf *et al.*, Eds. Indianapolis, IN, USA: Brown & Benchmark Press, 1988, pp. 236–240.

[41] N. Ravi *et al.*, "Activity recognition from accelerometer data," in *Proc. 17th Conf. Innov. Appl. Artif. Intell.*, Pittsburgh, PA, USA, July 2005, pp. 1541–1546.

[42] T. Seel *et al.*, "IMU-based joint angle measurement for gait analysis," *Sensors*, vol. 14, no. 4, pp. 6891–6909, Apr. 2014.

[43] S. O. H. Madgwick *et al.*, "Estimation of IMU and MARG orientation using a gradient descent algorithm," in *IEEE Int. Conf. Rehab. Robot.*, Zürich, Switzerland, June 2011, pp. 1–7.

[44] P. Cheng and B. Oelmann, "Joint-angle measurement using accelerometers and gyroscopes—a survey," *IEEE Trans. Instrum. Meas.*, vol. 59, no. 2, pp. 404–414, Feb. 2010.

[45] T. McGrath *et al.*, "An auto-calibrating knee flexion-extension axis estimator using principal component analysis with inertial sensors," *Sensors*, vol. 18, no. 6, June 2018.

[46] K. D. Shelbourne and P. Nitz, "Accelerated rehabilitation after anterior cruciate ligament reconstruction," *Am. J. Sports Med.*, vol. 18, no. 3, pp. 292–299, May 1990.

[47] B. M. Cascio *et al.*, "Return to play after anterior cruciate ligament reconstruction," *Clin. Sports Med.*, vol. 23, no. 3, pp. 395–408, July 2004.

[48] H.-K. Jeong *et al.*, "Quantifying the effects of increasing mechanical stress on knee acoustical emissions using unsupervised graph mining," *IEEE Trans. Neural Syst. Rehabil. Eng.*, vol. 26, no. 3, pp. 594–601, March 2018.

[49] H. Töreyin *et al.*, "Quantifying the Consistency of Wearable Knee Acoustical Emission Measurements During Complex Motions," *IEEE Journal of Biomedical and Health Informatics*, vol. 20, no. 5, pp. 1265–1272, 2016.

[50] B. Mascaro *et al.*, "Exploratory study of a non-invasive method based on acoustic emission for assessing the dynamic integrity of knee joints," *Med. Eng. Phys.*, vol. 31, no. 8, pp. 1013–22, Oct. 2009.

[51] L.-K. Shark *et al.*, "Knee acoustic emission: A potential biomarker for quantitative assessment of joint ageing and degeneration," *Med. Eng. Phys.*, vol. 33, no. 5, pp. 534–545, June 2011.

[52] C. Teague *et al.*, "Novel approaches to measure acoustic emissions as biomarkers for joint health assessment," in *Proc. 12th Int. Conf. Body Sensor Netw.*, Cambridge, MA, USA, June 2015, pp. 1–6.

[53] D. Adams *et al.*, "Current concepts for anterior cruciate ligament reconstruction: A criterion-based rehabilitation progression," *J. Orthop. Sports Phys. Ther.*, vol. 42, no. 7, pp. 601–614, July 2012.

[54] P. de Mille and J. Osmak, "Performance: Bridging the gap after ACL surgery," *Curr. Rev. Musculoskelet. Med.*, vol. 10, no. 3, pp. 297–306, July 2017.

[55] J. Cavanaugh and M. Powers, "ACL rehabilitation progression: Where are we now?" *Curr. Rev. Musculoskelet. Med.*, vol. 10, no. 3, pp. 289–296, Aug. 2017.

[56] M. C. Raynor *et al.*, "Cryotherapy after ACL reconstruction–A meta-analysis," *J. Knee Surg.*, vol. 18, no. 2, pp. 123–129, Apr. 2005.

[57] K. D. Shelbourne and C. Klotz, "What I have learned about the ACL: Utilizing a progressive rehabilitation scheme to achieve total knee symmetry after anterior cruciate ligament reconstruction," *J. Orthop. Sci.*, vol. 11, no. 3, pp. 318–325, May 2006.

[58] D. Schröder and H. Pässler, "Combination of cold and compression after knee surgery," *Knee Surg. Sports Traumatol. Arthrosc.*, vol. 2, no. 3, pp. 158–165, Sept. 1994.

[59] K. Shelbourne and D. Patel, "Timing of surgery in anterior cruciate ligament-injured knees," *Knee Surg. Sports Traumatol. Arthrosc.*, vol. 3, no. 3, pp. 148–156, Sept. 1995.

[60] M. S. Decarlo *et al.*, "Traditional versus accelerated rehabilitation following ACL reconstruction: A one-year follow-up," *J. Orthop. Sports Phys. Ther.*, vol. 15, no. 6, p. 309, June 1992.

[61] K. Shelbourne and P. Nitz, "Accelerated rehabilitation after anterior cruciate ligament reconstruction," *J. Orthop. Sports Phys. Ther.*, vol. 15, no. 6, pp. 256–264, June 1992.

[62] T. Shaw, "Accelerated rehabilitation following anterior cruciate ligament reconstruction," *Phys. Ther. Sport*, vol. 3, no. 1, pp. 19–26, Feb. 2002.

[63] G. Bravo-Illanes *et al.*, "IMU sensor fusion algorithm for monitoring knee kinematics in ACL reconstructed patients," in *Proc. 41st Annu. Int. Conf. IEEE Eng. Med. Bio. Soc.*, Berlin, Germany, July 2019, pp. 5877–5881.

[64] M. A. Watkins *et al.*, "Reliability of goniometric measurements and visual estimates of knee range of motion obtained in a clinical setting," *Phys. Ther.*, vol. 71, no. 2, pp. 90–96, Feb. 1991.

[65] H. O. Mayr *et al.*, "Arthrofibrosis following ACL reconstruction–Reasons and outcome," *Arch. Orthop. Trauma Surg.*, vol. 124, no. 8, pp. 518–522, Aug. 2004.

[66] B. P. Boden *et al.*, "Etiology and prevention of noncontact ACL injury," *Physician Sportsmed.*, vol. 28, no. 4, pp. 53–60, June 2000.

[67] P. Sadoghi *et al.*, "Effectiveness of anterior cruciate ligament injury prevention training programs," *J. Bone Joint Surg.*, vol. 94, no. 9, pp. 769–776, May 2012.

[68] J. D. Harris *et al.*, "Return to sport after ACL reconstruction." *Orthopedics*, vol. 37, no. 2, pp. e103–e108, Feb. 2014.

[69] T. E. Hewett *et al.*, "Anterior cruciate ligament injuries in female athletes: Part 1, mechanisms and risk factors," *Am. J. Sports Med.*, vol. 34, no. 2, pp. 299–311, Feb. 2006.

[70] C. Teague, "A robust system for sensing acoustic emissions for wearable knee health assessment," Master's thesis, School Elect. Comput. Eng., Georgia Inst. of Tech., Atlanta, GA, USA, 2016.

[71] W. Martinez *et al.*, *Exploratory Data Analysis with MATLAB*, 2nd ed. Boca Raton, FL, USA: CRC Press, 2010.

[72] B. Rosner, *Fundamentals of Biostatistics*. Boston, MA, USA: Cengage Learning, 2010.

[73] K. Liu *et al.*, "Visual estimation of lower limb motion using physical and virtual sensors," in *Proc. IEEE Int. Conf. Inf. Autom.*, Harbin, China, June 2010, pp. 179–184.

[74] J. F. S. Lin and D. Kulić, "Human pose recovery using wireless inertial measurement units," *Physiol. Meas*, vol. 33, no. 12, pp. 2099–2115, Dec. 2012.

[75] K. A. Elsaid *et al.*, "Association of articular cartilage degradation and loss of boundary-lubricating ability of synovial fluid following injury and inflammatory arthritis," *Arthritis Rheum.*, vol. 52, no. 6, pp. 1746–1755, June 2005.

[76] S. L. Woo *et al.*, "Biomechanics of knee ligaments: Injury, healing, and repair," *J. Biomech.*, vol. 39, no. 1, pp. 1–20, Oct. 2006.

[77] D. C. Whittingslow *et al.*, "Acoustic emissions as a non-invasive biomarker of the structural health of the knee," *Ann. Biomed. Eng.*, vol. 48, no. 1, pp. 225–235, Jan. 2020.

[78] H.-K. Jeong *et al.*, "b-Value: A potential biomarker for assessing knee-joint health using acoustical emission sensing," *IEEE Sens. Lett.*, vol. 2, no. 4, pp. 1–4, Dec. 2018.

[79] R Core Team, *R: A Language and Environment for Statistical Computing*, Vienna, Austria, 2018.

[80] R. Lenth *et al.*, *Estimated Marginal Means, aka Least-Squares Means*, 2020.

[81] K. R. Ford *et al.*, "Valgus knee motion during landing in high school female and male basketball players," *Med. Sci. Sports Exerc.*, vol. 35, no. 10, pp. 1745–50, Oct. 2003.

[82] T. E. Hewett *et al.*, "Decrease in neuromuscular control about the knee with maturation in female athletes," *J. Bone Joint Surg.*, vol. 86, no. 8, pp. 1601–8, Aug. 2004.

[83] H. R. Cowley *et al.*, "Differences in neuromuscular strategies between landing and cutting tasks in female basketball and soccer athletes," *J. Athl. Train.*, vol. 41, no. 1, pp. 67–73, 2006.

[84] Y. Morishige *et al.*, "Difference in leg asymmetry between female collegiate athletes and recreational athletes during drop vertical jump," *J. Orthop. Surg. Res.*, vol. 14, Dec. 2019, Art. no. 424.

[85] M. O. Heller *et al.*, "The influence of alignment on the musculo-skeletal loading conditions at the knee," *Langenbeck's Arch. Surg.*, vol. 388, pp. 291–297, Sept. 2003.

[86] T. J. Withrow *et al.*, "The effect of an impulsive knee valgus moment on in vitro relative acl strain during a simulated jump landing," *Clin. Biomech.*, vol. 21, no. 9, pp. 977–983, Nov. 2006.

[87] L. Herrington, "Knee valgus angle during single leg squat and landing in patellofemoral pain patients and controls," *The Knee*, vol. 21, no. 2, pp. 514–517, March 2014.

[88] T. E. Hewett *et al.*, "Biomechanical measures of neuromuscular control and valgus loading of the knee predict anterior cruciate ligament injury risk in female athletes: A prospective study," *Am. J. Sports Med.*, vol. 33, no. 4, pp. 492–501, Apr. 2005.

[89] N. B. Bolus *et al.*, "A glove-based form factor for collecting joint acoustic emissions: Design and validation," *Sensors*, vol. 19, no. 12, June 2019, Art no. 2683.

[90] T. E. Hewett *et al.*, "Mechanisms, prediction, and prevention of ACL injuries: Cut risk with three sharpened and validated tools," *J. Orthop. Res.*, vol. 34, no. 11, pp. 1843–1855, Sept. 2016.

[91] E. M. Wojtys *et al.*, "Association between the menstrual cycle and anterior cruciate ligament injuries in female athletes," *Am. J. Sports Med.*, vol. 26, no. 5, pp. 614–9, Sept. 1998.

[92] N. Voskanian, "ACL injury prevention in female athletes: Review of the literature and practical considerations in implementing an ACL prevention program," *Curr. Rev. Musculoskelet. Med.*, vol. 6, no. 2, pp. 158–63, Feb. 2013.

[93] S. Hersek *et al.*, "Acoustical emission analysis by unsupervised graph mining: A novel biomarker of knee health status," *IEEE Trans. Biomed. Eng.*, vol. 65, no. 6, pp. 1291–1300, June 2018.

[94] J. M. Binkley *et al.*, "The lower extremity functional scale (LEFS): Scale development, measurement properties, and clinical application," *Phys. Ther.*, vol. 79, no. 4, pp. 371–383, Apr. 1999.

[95] L. A. Adamic and E. Adar, "Friends and neighbors on the web," *Soc. Networks*, vol. 25, no. 3, pp. 211–230, July 2003.

[96] D. Edler and M. Rosvall, "Source code for multilevel community detection with Infomap," March 2017. [Online]. Available: http://www.mapequation.org/code.html.

[97] M. Rosvall and C. T. Bergstrom, "Maps of random walks on complex networks reveal community structure," *Proc. Nat. Acad. Sci.*, vol. 105, no. 4, p. 1118–1123, Jan. 2008.

[98] M. B. Pouyan and M. Nourani, ""clustering single-cell expression data using random forest graph," *IEEE J. Biomed. Health Inf.*, vol. 21, no. 4, pp. 1172–1181, July 2017.

[99] C. M. Bishop, *Pattern Recognition and Machine Learning*. New York, NY, USA: Springer, 2006.

[100] M. Verleysen and D. François, "The curse of dimensionality in data mining and time series prediction," in *Proc. 8th Int. Conf. Artif. Neural Netw.: Comput. Intell. Bioinspired Syst.*, 2005, pp. 758–770.

[101] P. Indyk and R. Motwani, "Approximate nearest neighbors: Towards removing the curse of dimensionality," in *Proc. 30th Annu. ACM Symp. Theory Comput.*, Dallas, Texas, USA, May 1998, pp. 604–613.

[102] J. Levine *et al.*, "Data-driven phenotypic dissection of AML reveals progenitor-like cells that correlate with prognosis," *Cell*, vol. 162, no. 1, pp. 184–197, July 2015.

[103] C. Xu and Z. Su, "Identification of cell types from single-cell transcriptomes using a novel clustering method," *Bioinformatics*, vol. 31, no. 12, pp. 1974–1980, June 2015.

[104] C. Fraley and A. E. Raftery, ""model-based clustering, discriminant analysis, and density estimation," *J. Amer. Statist. Assoc.*, vol. 97, no. 458, pp. 611–631, June 2002.

[105] R. E. Andersen *et al.*, "A review of engineering aspects of vibroarthography of the knee joint," *Crit. Rev. Phys. Rehabil. Med.*, vol. 28, no. 1-2, pp. 13–32, 2016.

[106] Q. Liu *et al.*, "Gazelle: Energy-efficient wearable analysis for running," *IEEE Trans. Mobile Comput.*, vol. 16, no. 9, pp. 2531–2544, Sept. 2017.

[107] S. Hersek *et al.*, "A robust system for longitudinal knee joint edema and blood flow assessment based on vector bioimpedance measurements," *IEEE Trans. Biomed. Circuits Syst.*, vol. 10, no. 3, pp. 545–555, June 2016.

[108] A. Hafid *et al.*, "Full impedance cardiography measurement device using Raspberry PI3 and system-on-chip biomedical instrumentation solutions," *IEEE J. Biomed. Health Inform.*, vol. 22, no. 6, pp. 1883–1894, Nov. 2018.

[109] T. Vuorela *et al.*, "Design and implementation of a portable long-term physiological signal recorder," *IEEE Trans. Inf. Technol. Biomed.*, vol. 14, no. 3, pp. 718–725, May 2010.

[110] M. Rapin *et al.*, "Wearable sensors for frequency-multiplexed EIT and multilead ECG data acquisition," *IEEE Trans. Biomed. Eng.*, vol. 66, no. 3, pp. 810–820, March 2019.

[111] C. N. Teague *et al.*, "Novel methods for sensing acoustical emissions from the knee for wearable joint health assessment," *IEEE Trans. Biomed. Eng.*, vol. 63, no. 8, pp. 1581–1590, Aug. 2016.

[112] Y. Athavale and S. Krishnan, "A telehealth system framework for assessing knee-joint conditions using vibroarthrographic signals," *Biomed. Signal Process. Control*, vol. 55, Jan. 2020, Art. no. 101580.

[113] K. C. Barr and K. Asanovi, "Energy-aware lossless data compression," *ACM Trans. Comput. Syst.*, vol. 24, no. 3, pp. 250–291, Aug. 2006.

[114] D. D. Mehta *et al.*, "Mobile voice health monitoring using a wearable accelerometer sensor and a smartphone platform," *IEEE Trans. Biomed. Eng.*, vol. 59, no. 11, pp. 3090–3096, Nov. 2012.

[115] B. Travaglione *et al.*, "Using low cost single-board microcontrollers to record underwater acoustical data," in *Internoise Conf.*, Melbourne, Australia, Nov. 2014.

[116] M. Caldas-Morgan *et al.*, "An autonomous underwater recorder based on a single board computer," *PloS One*, vol. 10, no. 6, June 2015, Art. no. e0130297.

[117] B. Gao and W. L. Woo, "Wearable audio monitoring: Content-based processing methodology and implementation," *IEEE Trans. Human-Mach. Syst.*, vol. 44, no. 2, pp. 222–233, Apr. 2014.

[118] A. P. Hill *et al.*, "AudioMoth: Evaluation of a smart open acoustic device for monitoring biodiversity and the environment," *Methods Ecol. Evol.*, vol. 9, no. 5, pp. 1199–1211, May 2018.

[119] S. Mabrouk *et al.*, "Robust longitudinal ankle edema assessment using wearable bioimpedance spectroscopy," *IEEE Trans. Biomed. Eng.*, vol. 67, no. 4, pp. 1019–1029, Apr. 2020.

[120] SD Association, *SD Specifications: Part 1 Physical Layer Simplified Specification*, Std., 2016.

[121] M. Etemadi *et al.*, "A wearable patch to enable long-term monitoring of environmental, activity and hemodynamics variables," *IEEE Trans. Biomed. Circuits Syst.*, vol. 10, no. 2, pp. 280–288, April 2016.

[122] IEC 60601-1-11, *Medical electrical equipment–Part 1-11: General requirements for basic safety and essential performance–Collateral standard: Requirements for medical electrical equipment and medical electrical systems used in the home healthcare environment*, Std., 2015.

[123] J. R. Basford and S. J. Johnson, "Form may be as important as function in orthotic acceptance: A case report," *Arch. Phys. Med. Rehabil.*, vol. 83, no. 3, pp. 433–435, March 2002.

[124] H. Töreyin *et al.*, "Real-time activity classification in a wearable system prototype for knee health assessment via joint sounds," in *Proc. 38th Annu. Int. Conf. IEEE Eng. Med. Bio. Soc.*, Orlando, FL, USA, Aug. 2016, pp. 3113–3116.

[125] G. Cohn *et al.*, "An ultra-low-power human body motion sensor using static electric field sensing," in *Proc. ACM Conf. Ubiquitous Comput.*, Pittsburgh, PA, USA, Sept. 2012, pp. 99–102.

[126] R. W. Reger *et al.*, "Near-zero power accelerometer wakeup system," in *Proc. 2017 IEEE SENSORS*, Glasgow, Scotland, Oct. 2017, pp. 1–3.

[127] S. I. Lee *et al.*, "A novel flexible wearable sensor for estimating joint-angles," in *Proc. 13th Int. Conf. Body Sensor Netw.*, San Fransisco, CA, USA, June 2016, pp. 377–382.

[128] J. Perry, "Kinesiology of lower extremity bracing," *Clin. Orthop. Relat. Res.*, vol. 102, pp. 18–31, July–Aug. 1974.

[129] M. Sarillee *et al.*, "Assessment of knee joint abnormality using acoustic emission sensors," in *Proc. 4th IEEE Int. Conf. Control Syst., Comput. Eng.*, Batu Ferringhi, Malaysia, Nov. 2014, pp. 378–383.

[130] B. Semiz *et al.*, "Using knee acoustical emissions for sensing joint health in patients with juvenile idiopathic arthritis: A pilot study," *IEEE Sensors J.*, vol. 18, no. 22, pp. 9128–9136, Nov. 2018.

[131] R. Kianifar *et al.*, "Automated assessment of dynamic knee valgus and risk of knee injury during the single leg squat," *IEEE J. Transl. Eng. Health Med.*, vol. 5, Oct. 2017, Art. no. 2100213.

[132] R. A. Bloomfield *et al.*, "Proposal and validation of a knee measurement system for patients with osteoarthritis," *IEEE Trans. Biomed. Eng.*, vol. 66, no. 2, pp. 319–326, Feb. 2019.

[133] H. Dejnabadi *et al.*, "Estimation and visualization of sagittal kinematics of lower limbs orientation using body-fixed sensors," *IEEE Trans. Biomed. Eng.*, vol. 53, no. 7, pp. 1385–1393, July 2006.

[134] Y.-M. Choi *et al.*, "Wearable biomechanical energy harvesting technologies," *Energies*, vol. 10, Sept. 2017, Art. no. 1483.

[135] J. M. Donelan *et al.*, "Biomechanical energy harvesting: generating electricity during walking with minimal user effort," *Science*, vol. 319, no. 5864, pp. 807–810, Feb. 2008.

[136] Y. Kuang *et al.*, "Design and characterisation of a piezoelectric knee-joint energy harvester with frequency up-conversion through magnetic plucking," *Smart Mater. Struct.*, vol. 25, no. 8, Aug. 2016.

[137] C. Apgar *et al.*, "Biomechanical energy harvesting using a knee mounted generator," in *Pro. IEEE Syst. Inf. Eng. Des. Symp.*, Charlottesville, VA, USA, Apr. 2016, pp. 1–5.

[138] "Powerwalk®," https://www.bionic-power.com/, (accessed: March 15, 2020).

[139] M. Safaei *et al.*, "A review of energy harvesting using piezoelectric materials: State-of-the-art a decade later (2008-2018)," *Smart Mater. Struct.*, vol. 28, Nov. 2019, Art. no. 113001.

[140] M. A. Bin Altaf *et al.*, "A 16-channel patient-specific seizure onset and termination detection soc with impedance-adaptive transcranial electrical stimulator," *IEEE J. Solid-State Circuits*, vol. 50, no. 11, pp. 2728–2740, Nov. 2015.

[141] C. Wu *et al.*, "A 16-channel cmos chopper-stabilized analog front-end ecog acquisition circuit for a closed-loop epileptic seizure control system," *IEEE Trans. Biomed. Circuits Syst.*, vol. 12, no. 3, pp. 543–553, June 2018.

[142] S. Shah *et al.*, "A proof-of-concept classifier for acoustic signals from the knee joint on a FPAA," in *Proc. 2016 IEEE SENSORS*, Orlando, FL, USA, Oct. 2016, pp. 1–3.

[143] Y. Zhang *et al.*, "Advancing hand gesture recognition with high resolution electrical impedance tomography," in *Proc. 29th Annu. Symp. User Interface Softw. Tech.*, Tokyo, Japan, Oct. 2016, p. 843–850.

[144] Z. Xu *et al.*, "Development of a portable electrical impedance tomography system for biomedical applications," *IEEE Sensors J.*, vol. 18, no. 19, pp. 8117–8124, Oct. 2018.

[145] J. A. Martin *et al.*, "Gauging force by tapping tendons," *Nat. Commun.*, vol. 9, pp. 1592–1592, Apr. 2018, Art. no. 1592.

[146] E. A. Kessler *et al.*, "Decreasing patient cost and travel time through pediatric rheumatology telemedicine visits," *Pediatr. Rheumatol.*, vol. 14, Sept. 2016, Art. no. 54.

[147] R. D. Altman *et al.*, "Recommendations for the medical management of osteoarthritis of the hip and knee: 2000 update," *Arthritis Rheum.*, vol. 43, no. 9, pp. 1905–1915, Jan. 2000.

[148] M. W. Millar-Craig *et al.*, "Circadian variation of blood-pressure," *The Lancet*, vol. 311, no. 8068, pp. 795–797, Apr. 1978.